POLYPUBLIE
Polytechnique Montréal

POLYTECHNIQUE MONTRÉAL
UNIVERSITÉ D'INGÉNIERIE

Titre: Title:	The Mechanical Buckling Behaviour of Composite Sandwich Structure Made from Hybrid Glass/Carbon Face Sheets and Rigid Foam Core
Auteur: Author:	Muhammad Basha
Date:	2016
Type:	Mémoire ou thèse / Dissertation or Thesis
Référence: Citation:	Basha, M. (2016). The Mechanical Buckling Behaviour of Composite Sandwich Structure Made from Hybrid Glass/Carbon Face Sheets and Rigid Foam Core [Thèse de doctorat, École Polytechnique de Montréal]. PolyPublie. https://publications.polymtl.ca/2370/

Document en libre accès dans PolyPublie
Open Access document in PolyPublie

URL de PolyPublie: PolyPublie URL:	https://publications.polymtl.ca/2370/
Directeurs de recherche: Advisors:	Rachid Boukhili
Programme: Program:	Génie mécanique

Ce fichier a été téléchargé à partir de PolyPublie, le dépôt institutionnel de Polytechnique Montréal
This file has been downloaded from PolyPublie, the institutional repository of Polytechnique Montréal

https://publications.polymtl.ca

UNIVERSITÉ DE MONTRÉAL

THE MECHANICAL BUCKLING BEHAVIOUR OF COMPOSITE SANDWICH STRUCTURE MADE FROM HYBRID GLASS/CARBON FACE SHEETS AND RIGID FOAM CORE

MUHAMMAD BASHA

DÉPARTEMENT DE GÉNIE MÉCANIQUE

ÉCOLE POLYTECHNIQUE DE MONTRÉAL

THÈSE PRÉSENTÉE EN VUE DE L'OBTENTION

DU DIPLÔME DE PHILOSOPIAE DOCTOR

(GÉNIE MÉCANIQUE)

DÉCEMBRE 2016

© Muhammad Basha, 2016.

UNIVERSITÉ DE MONTRÉAL

ÉCOLE POLYTECHNIQUE DE MONTRÉAL

Cette thèse intitulée :

THE MECHANICAL BUCKLING BEHAVIOUR OF COMPOSITE SANDWICH STRUCTURE MADE FROM HYBRID GLASS/CARBON FACE SHEETS AND RIGID FOAM CORE

présentée par : BASHA Muhammad

en vue de l'obtention du diplôme de : Philosophiae Doctor

a été dûment acceptée par le jury d'examen constitué de :

M. BALAZINSKI Marek, Docteur ès sciences., président

M. BOUKHILI Rachid, Doctorat., membre et directeur de recherche

M. VADEAN Aurelian, Doctorat., membre

M. ATARSIA Abdelatif, Ph. D., member externe

DEDICATION

To my parents, wife and children

God Bless you all

ACKNOWLEDGEMENTS

I would like thank my academic advisor, Professor Rashid Boukhili, for his kind guidance throughout my PhD journey and for his support in providing the valuable resources to perform the experimental work included in this dissertation.

I want to express my gratitude to my follow PhD colleague for helping me during the PhD program especially with the experimental work and the French language.

I would also like to express my thanks for my sponsor King Abdul Aziz University in Saudi Arabia, Jeddah for their grant to pursue my PhD program in École Polytechnique de Montréal.

Finally very special thanks to my Father Dr. Adnan Basha, My Mother Nawal for their emotional support and prayers and my wife Reem for being very supportive and patient during the period of my study. I also appreciate her for being a great mother to our children Maya, Abdulmalik and Misk.

RÉSUMÉ

L'apparition d'un effet hybride en flambage pour des panneaux sandwichs fabriqués à partir des peaux composites hybrides interlaminaires et d'une âme en mousse rigide a fait l'objet de cette étude. Dans un premier temps, des essais expérimentaux ont été effectués et les résultats obtenus ont été validés à l'aide des prédictions analytiques et des simulations numériques. Deuxièmement, une comparaison exhaustive entre les résultats expérimentaux, analytiques et numériques a été effectuée pour confirmer l'apparition d'un effet hybride, qui était l'objectif principal de cette étude.

Sur le plan expérimental, des panneaux sandwich ont été fabriqués à l'aide du procédé de moulage par transfert de résine assisté sous vide (VARTM). À ce stade, l'infusion de la résine a été effectuée simultanément à travers les deux peaux du sandwich. Par ailleurs, une série des tests de compression a été effectuée pour optimiser les dimensions des échantillons de flambage. En outre, des essais de flexion 3 points ont été réalisés pour étudier d'une part l'existence d'un effet hybride dans les six échantillons hybrides fabriqués à partir de peaux composites en fibres hybrides 2:2 (verre:carbone) et d'autre part, leur capacité à retarder la déformation plastique et la rupture finale. Les résultats des échantillons hybrides ont été comparés à ceux de deux échantillons de référence réalisés à partir des panneaux sandwichs avec des peaux entièrement en fibre de verre ou de carbone. Il a été constaté lors des essais de flexion, que les probabilités de la rupture de la peau sont plus élevées lorsque les couches de fibres de carbone sont placées au niveau ou à proximité du côté extérieur de la peau. De plus, les meilleures performances en flexion sont obtenues par les échantillons avec des peaux équilibrées. Enfin, le comportement en flambage des six panneaux sandwichs différents a été étudié en comparaison avec deux panneaux sandwichs de référence. La déflexion hors plan de chaque échantillon a été mesurée par des capteurs laser à réflexion sans contact, placés de deux côtés de l'échantillon pour capturer les déflexions négatives et positives. Les résultats des essais de flambage ont révélés un effet hybride positif pour l'échantillon hybride avec un ordre alterné des couches de fibres de verre et de carbone en retardant la charge critique de flambage de 11,4% à 18,3%. Un examen microscopique a été effectué pour étudier les modes de rupture et leurs mécanismes pour les échantillons testés en flexion 3 point et aussi en flambage.

Sur le plan analytique, les théories de *Shear Deformation Plate* (SDPT) et *Allen Thick Face sheet* (ATFT) ont été utilisées pour prédire les charges critiques de flambage des panneaux sandwichs

étudiés. Les résultats obtenus par la théorie SDPT sont en désaccord avec ceux obtenus par la théorie (ATFT). La théorie (ATFT) concorde mieux avec les résultats expérimentaux et les prédictions numériques.

Sur le plan numérique, un modèle 2D multicouches a été construit à l'aide du logiciel d'éléments finis ANSYS V13.0 pour reproduire les expériences du test de flexion 3 points et pour valider les propriétés mécaniques utilisées pour les panneaux sandwichs hybrides. Les prédictions numériques du comportement élastique (la partie linéaire de la courbe contrainte-déformation) des panneaux sandwichs étudiés étaient en bon accord avec les résultats du test. Un deuxième modèle 2D a été ensuite construit pour simuler le comportement non-linéaire de flambage observé lors des essais expérimentaux. L'analyse non-linéaire a été d'abord effectuée à l'aide de la méthode de Newton-Raphson, puis en ajoutant l'option de stabilisation non-linéaire au logiciel d'éléments finis. Les résultats du modèle concordent avec les résultats expérimentaux avec une différence marginale allant de 2% à 11%.

ABSTRACT

The occurrence of a hybrid effect for sandwich panels made from inter-laminar hybrid composite face sheets and a rigid foam core with respect to buckling performance was the subject of investigation in this study. As a first step, this study performed experiments and validated the results using analytical predictions and numerical simulations. Second, a comprehensive comparison of the experimental, analytical and numerical results was used to confirm the occurrence of a hybrid effect, which was the study's major objective.

Experimentally, all the sandwich panels were fabricated using the Vacuum Assisted Resin Transfer Molding (VARTM) process by double infusing the resin through the sandwich panel face sheets simultaneously. A set of compressive tests were performed to optimize the dimensions of the buckling test specimens that delivered the most clear and recordable out-of-plane deflection using non-contact laser sensors. Additionally, flexural 3-point bending tests were performed to investigate the existence of a hybrid effect within the six hybrid specimens made from 2:2 hybrid (glass:carbon) fiber face sheets and to study their ability to delay the yield and ultimate loading points. The hybrid specimen results were compared to two baseline specimens made from sandwich panels with all-glass or all-carbon face sheets. The chances of face sheet failure were higher when the carbon fiber layers were placed at or near the outer side of the face sheet lamina during the bending tests. Moreover, the best flexural performance was delivered by the specimens with balanced face sheets. Finally, the buckling behavior of the six different sandwich panels were investigated compared to the two baseline sandwich panels. The out-of-plane deflection of each specimen was measured by back-to-back reflex non-contact laser sensors to capture the negative and positive deflections on both sides of the specimen. The experimental buckling results showed a positive hybrid effect in the hybrid specimen with an alternating order of glass and carbon lay-up in delaying the critical buckling load by 11.4% to 18.3%. A microscopic examination was performed to investigate the failure modes and their mechanisms caused by both the flexural 3-point bending tests and the buckling tests.

Analytically, the Shear Deformation Plate Theory (SDPT) and Allen Thick Face sheet Theory (ATFT) were used to predict the critical buckling loads for all the specimens. The SDPT output results disagreed with the results obtained from ATFT in terms of their values and their rate of

gradual increase. ATFT provided a good level of agreement with the experimental and numerical results.

Numerically, a multi-layered 2D model was constructed using a commercial finite element analysis (FEA) package (ANSYS V13.0) to simulate the flexural 3-point bending test experiment and to validate the calculated mechanical properties of the hybrid sandwich panels. As a result, the linear part of the experimental stress-deflection curves of all the sandwich panels were in good agreement with the numerical results. A second 2D model was constructed to simulate the non-linear buckling behavior demonstrated through the experimental procedure using the same FEA package. The model had two face sheets attached to a middle core and was designed to simulate the experimental boundary and loading conditions in addition to the out-of-plane deflection readings recorded by the non-contact laser sensors. Non-linear analysis was performed first using Newton-Raphson and then by adding the non-linear stabilization option to the software solver. The mode results agreed with the experimental results with a marginal difference ranging from 2% to 11%.

TABLE OF CONTENTS

DEDICATION III

ACKNOWLEDGEMENTS IV

RÉSUMÉ V

ABSTRACT VII

TABLE OF CONTENTS IX

LIST OF TABLES XIII

LIST OF FIGURES XIV

LIST OF SYMBOLS AND ABBREVIATIONS XIX

LIST OF APPENDICES XXII

CHAPTER 1 INTRODUCTION 1

1.1 Project Objective 11

Research Problem/Question 13

Thesis Structure 13

CHAPTER 2 LITERATURE REVIEW 15

2.1 Composite Materials 15

2.2 Composite Inter-Laminar Failure Modes 16

2.2.1 Mode 1: Fiber Tensile Fracture 16

2.2.2 Mode 2: Fibre Micro-Buckling "Kinking" 17

2.2.3 Mode 3: Fibre and Matrix Crushing 18

2.3 Composite Sandwich Structure 19

2.4 Sandwich Panel Flexural Rigidity 20

2.5 Composite Manufacturing 22

2.6 Sandwich Panel Manufacturing 23

2.7 Vacuum Assisted Resin Transfer Molding (VARTM) 25

2.8 Woven Fabrics 26

2.8.1 Woven Composite Fabric Mechanical Performance under Compression 28

2.9 Composite Sandwich Buckling 29

2.9.1 Sandwich Panels Buckling Failure Modes 29

2.9.2 Analytical Buckling Failure Prediction 31

2.9.3 Numerical Buckling Analysis 37

2.10 Hybrid Composites 38

2.10.1 Hybrid Composite Theory 40

2.10.2 Hybrid Effect 44

2.10.3 Bridging Effect 46

2.10.4 Experimental Hybrid Composites Mechanical Performance 47

CHAPTER 3 EXPERIMENTAL PROCEDURE 56

3.1 Manufacturing 56

3.1.1 Manufacturing Process 59

3.1.2 Face Sheet Fibre Volume Fraction V_f 61

3.2 Test Specimen Design and Face Sheets Arrangements 62

3.3 Experimental Critical Buckling Load (P_{cr}) 66

3.4 Buckling Test Specimens Dimensions 67

3.5 Flexural 3-Point Bending Test 72

3.5.1 3-Point Bending Test Set-up 73

3.5.2 Bending Test Results 74

3.6 Buckling Test Set-up 82

3.7 Experimental Test Results 84

3.7.1 The Extraction of P_{cr} from the Experimentally Recorded Data 84

3.7.2 Buckling Test 86

3.7.3 Load Vs. In-plane Displacement 91

3.7.4 Load Vs. Out-of-plane Deflection 94

CHAPTER 4 NUMERICAL MODELING 98

4.1 Flexural 3-Point Bending Model 99

4.1.1 Materials Properties 102

4.1.2 Flexural 3-Point Bending Model Results 105

4.2 Non-linear buckling model 112

4.3 Non-Linear Stabilization 116

4.3.1 Modified Model with Non-Linear Stabilization 116

4.4 Results and Discussion 117

CHAPTER 5 ANALYTICAL, EXPERIMENTAL AND NUMERICAL RESULTS 121

5.1 Flexural 3-Point Bending Results 121

5.2 ATFT and SDPT 123

5.3 The Analytical, Experimental and Numerical P_{cr}: A Comparison 124

CHAPTER 6 CONCLUSION AND CONTRIBUTION TO KNOWLEDGE 128

6.1 Contribution to the Knowledge 129

6.2 Recommendations and Future Work 131

BIBLIOGRAPHY 132

APPENDICES……... 142

LIST OF TABLES

Table 3-1: The materials used in manufacturing the sandwich panels 61

Table 3-2: Comparison of the instrumentations used in experimental tests 67

Table 3-3: 3-Point bending test results.....77

Table 3-4: Buckling test experimental results.....88

Table 4-1: Material properties of the sandwich model face sheets 105

Table 4-2: Experimental and numerical results of the flexural 3-point bending tests 107

Table 4-3: FE model materials properties 114

Table 4-4: Numerical and experimental P_{cr} results.....118

LIST OF FIGURES

Figure 1-1: Walt Disney World monorail 2

Figure 1-2: The Construction of the overwing fairing of the F-14 3

Figure 1-3: Okinawa All Hybrid Pedestrian Bridge.....5

Figure 1-4: (a) The Joffre bridge in Sherbrooke, QC. (b) Tylor bridge in headingly, MN.....5

Figure 1-5: Composite sandwich panel (wall) 6

Figure 1-6: Sandwich panels sections 7

Figure 1-7: Hollow sandwich panel with filling options.....7

Figure 1-8: (a) manufacturing sandwich panels. (b) Sandwich panels assembly 9

Figure 1-9: two and multi storey buidlings made from sandwich panels walls.....9

Figure 1-10: Wind rotor blade structure.....10

Figure 1-11: (a) Hybrid AFO (Composite, 2016), (b) Hybrid compact ballistic helmets used by the Canadian Forces. 11

Figure 2-1: Forces acting on a composite lamina 15

Figure 2-2: Fibre tensile fracture.....17

Figure 2-3: Fibre micro-buckling failure 18

Figure 2-4: Fibre and matrix lateral crushing failure 19

Figure 2-5: Fibre and matrix crushing failure at ± 54º.....19

Figure 2-6: Sandwich structure 20

Figure 2-7: Flexural rigidity, lamina vs. sandwich structure 21

Figure 2-8: Cross section of a sandwich structure 21

Figure 2-9: Steps of Manufacturing composites 23

Figure 2-10: VARTM manufacturing set-up 26

Figure 2-11: Wrap and fill directions in woven fabrics 27

Figure 2-12: Some fabric woven styles 28

Figure 2-13: Performance of UD woven carbon fibre under compressive load 29

Figure 2-14: Sandwich Panels Failure modes under uniaxial compression load (a) specimen under uniaxial compression, (b) Global buckling, (c) local buckling (face sheet delamination), (d) Local buckling (face sheet crushing), (e) shear crimping 30

Figure 2-15: Bucking and post buckling stability and neutral behaviour 31

Figure 2-16: Euler's critical buckling fixing conditions 32

Figure 2-17: Comparison between different analytical solutions to solutions for Pcr 33

Figure 2-18: Schematic of the additional displacment due to transverse shear and core shear strain 35

Figure 2-19: Allen thick sandwich 35

Figure 2-20: Uniaxial buckling load with n =1 and m=2 36

Figure 2-21: Newton-Raphson non-linear iterative method 143

Figure 2-22: Types of hybrid composites 40

Figure 2-23: Tensile strength variation model in interply hybrid laminates 41

Figure 2-24: Variations of the tensile strength and modulus of a carbon/glass composite 44

Figure 2-25: Hybrid effect as proposed by Hayashi 45

Figure 2-26: Pandya et al. hybrid effect of hybrid specimens under tensile and compressive loading 51

Figure 2-27: Zhang et al. (a) tensile stress-strain curve. (b) compressive stress-strain curve. (c) flexural stress-strain curve (d) experimental vs. analytical flexural results. (e) experimental vs. analytical tensile and compressive results 55

Figure 3-1: Grooved foam core patterns 56

Figure 3-2: Types of commercial foam cores 57

Figure 3-3: Dry spots and resin rich areas in the VARTM samples 58

Figure 3-4: VARTM mold 59

Figure 3-5: Sandwich panel before resin infusion 60

Figure 3-6: 7781 8H glass and 94101 plain 3k T-300 carbon Fibres fabrics and SAN core 61

Figure 3-7: ASTM D792-00 standard test methods for density and specific gravity (Relative Density) of plastics by displacement.....62

Figure 3-8: Sandwich panel configurations 65

Figure 3-9: Load vs. in-plane displacement for sandwich panels made from all-carbon and all-glass face sheets 68

Figure 3-10: Load vs. in-plane displacement for the samples with L/b = 4 and 3.....69

Figure 3-11: Load vs. out-of--plane deflection for the samples with L/b = 4 and 3.....69

Figure 3-12: Compressive load vs. in-plane displacement 71

Figure 3-13: Compressive load vs. out-of-plane deflection.....71

Figure 3-14: (a) diamond cutting table saw. (b) buckling test specimens.....72

Figure 3-15: 3-point bending test set-up 73

Figure 3-16: The extracted P_{yld} and P_{ult} from the load-deflection curve.....75

Figure 3-17: The experimental stress-deflection curves of the 3-point bending test.....75

Figure 3-18: Microscopic bending failure zones view.....79

Figure 3-19: (a) P_{yild} for all tested specimens. (b) w_{yild} for all tested specimens. (c) (a) w_{ult} for all tested specimens. (d) P_{ult} for all tested specimens 81

Figure 3-20: AMSLER 600-ton universal test machine.....82

Figure 3-21: Buckling test set-up. (a) specimen under pure compression loading. (b) specimen starting to deflect (global buckling failure). (c) shear crimping failure of specimen.....83

Figure 3-22: Methods of extracting P_{cr} from experimental data. (a) Southwell plot, (b) top-of-the-knee method, (c) Strain-reversal method and (d) average stress/unit-shortening method.....84

Figure 3-23: Experimental buckling curve divided into 4 zones 85

Figure 3-24: Specimens failure zones on the load vs out-of-plane deflection curve 87

Figure 3-25: Sandwich panel face sheet lay-up and different flexural rigidities of the face sheets during bending.....89

Figure 3-26: : Microscopic buckling failure zones: (a) shear crimping failure, (b) failure zone at 10x zoom, (c) failure zone at 150x zoom.....90

Figure 3-27: : Load vs. In-plane displacement performance 91

Figure 3-28: P_{ult} load for all tested specimens 93

Figure 3-29: d_{ult} load for all tested specimens.....94

Figure 3-30: Load vs. out-of-plane deflection 95

Figure 3-31: Pcr extracted from both $+w$ and $-w$.....97

Figure 3-32: w_{max} load for all tested specimens 97

Figure 4-1: (a) The arranged layers of the sandwich panel model. (b) the woven fabric equivalent ply thickness.....100

Figure 4-2: Shell 281 geometry.....101

Figure 4-3: (a) The 3-point bending models with the applied load and boundary conditions. (b) Von-mises stress distribution 101

Figure 4-4: Normal, bending and twisting loads applied on a lamina 102

Figure 4-5: The Von-mises stress vs. deflection of the numerical and experimental results of all the tested sandwich panels 108

Figure 4-6: Von-Mises stress distribution for each layer within the sandwich panel numerical model 109

Figure 4-7: Von-mises yield stress distribution across the model thickness.....110

Figure 4-8: Von-mises ultimate stress distribution across the model thickness 110

Figure 4-9: The FEA 2D buckling model 112

Figure 4-10: (a) The model after meshing and applying boundary conditions, (b) the models first buckling mode shape 113

Figure 4-11: Newton-Raphson non-linear curve results 115

Figure 4-12: Experimental and FEA load vs. out-of-plane deflection for S1 and S8 118

Figure 4-13: Experimental and FEA load vs. out-of-plane deflection for H1 and H6 119

Figure 4-14: Experimental, FEA and MFEA load vs. out-of-plane deflection for H2 and H5 119

Figure 4-15: Experimental, FEA and MFEA load vs. out-of-plane deflection for H3 and H4 120

Figure 5-1: ATFT analytical prediction compared to SDPT results 123

Figure 5-2: Comparison of the experimental, numerical and analytical P_{cr} results 1/2 125

Figure 5-3: Comparison of the experimental, numerical and analytical P_{cr} results 2/2 126

LIST OF SYMBOLS AND ABBREVIATIONS

A	Area of transverse shear
AFO	Ankle Foot Orthosis
ARALL	Aramid Reinforced Aluminum Laminate
ATFT	Allen Thick Face Sheet Theory
b	Sandwich width
β	Euler correction factor
c	Core thickness
C.V	Coefficient of Variance
DOF	Degree of Freedom
E_a	Modulus of fibre a
E_b	Modulus of fibre b
E_c	Modulus of core material
E_f	Modulus of fibres
E_m	Modulus of matrix
E_x	Longitudinal modulus of elasticity (x-axis)
E_y	Lateral modulus of elasticity (y-axis)
E_z	Out-of-plane modulus of elasticity (z-axis)
$(EI)_b$	Sandwich panel flexural rigidity
$(EI)_f$	Face sheets flexural rigidity
E_s	Modulus of face sheets
FE	Finite Element

FFW	Future Force Warrior
F_i	Numerical buckling initiation force
Gc	Core shear modulus
Gxy	Shear modulus (xy)
Gyz	Shear modulus (yz)
Gzx	Shear modulus (zx)
GLARE	Glass Fibre Reinforced Aluminum
HE	High Elongation
HYCOPROD	Hybrid Composites Products project
L	Sandwich panel length
LE	Low Elongation
m	Buckling mode along the sandwich panel length
n	Buckling mode along the sandwich panel width
OOA	Out of Autoclave
PASGT	Personnel Armor System for Ground Troops
P_C	Shear buckling load
P_{Cr}	Critical buckling load
P_E	Euler buckling load
P_{Ef}	Euler buckling load for face sheets
PVC	Polyvinyl Chloride
R_x	Rotation about the x-axis
R_x	Rotation about the y-axis
R_x	Rotation about the z-axis

ROM	Rule of Mixture
SAN	Styrene Acrylonitrile
SDPT	Shear Deformation Plate Theory
SCRIMP	Seemann Resin Infusion Molding Process
SHM	Structural Health Monitoring System
t	Face sheet thickness
TiGr	Titanium graphite laminates
U_x	longitudinal transition along the x-axis
U_y	Transverse transition along the y-axis
U_z	Out-of-plane transition along the z-axis
UD	Unidirectional
VARTM	Vacuum Assisted Resin Transfer Modling
w	Out-of-plane deflection

LIST OF APPENDICES

APPENDIX A – ANSYS ITERATIVE NEWTON-RAPHSON METHOD 142

APPENDIX B – MATERIALS PROPERTIES USED IN NUMERICAL ANALYSIS 144

APPENDIX C – STRESS DISTRIBUTION ACROSS NUMERICAL MODEL'S THICKNESS 151

CHAPTER 1 INTRODUCTION

Composite sandwich structures are gradually replacing the conventional structural materials used in building columns, offshore structures and both pedestrian and traffic bridges. This is made possible due to the tailored properties of composite sandwich structures that can bear and resist different types of loads combined with severe environmental conditions for several structural applications. New, simple and economical manufacturing techniques such as Out of Autoclave (OOA), Seemann Composites Resin Infusion Process (SCRIMP) and Vacuum Assisted Resin Transfer Molding (VARTM) have improved the manufacturing process of composite structures.

Buckling resistance in columns is an important structural property that encourages building or reinforcing columns with composite materials to enhance the columns' structural integrity and stability by adding the distinct advantages of composite sandwiches. Stability and even degraded continuous load resistance after the first buckling failure in sandwich structures is one of the greatest benefits to structural safety and durability.

Since the introduction of glass fibers in the 1950s, they have been increasingly replacing metals in main and secondary structures due to their low cost and high strength. On the other hand, the use of stronger, lighter and stiffer carbon fibers remains low because of their higher cost (Short & Summerscales, 1979). Therefore, incorporating carbon fibers with glass fibers in hybrid textile fabrics had helped the industry to create lighter, stronger and less corrosive structures without an excessive increase in production cost. Numerous studies regarding hybrid composite behavior and manufacturing have been published, especially in aerospace and automotive applications. Further investigations have been conducted by researchers to expand the use of hybrids to new and modern applications beyond the aerospace industry, such as the mechanical, chemical and civil engineering disciplines.

The automotive industry has used hybrid structures to reduce vehicle weights. Old reports showed an early interest in implementing composites and hybrid composites in land transportation industries (Shimamura & Ishine, 1976) (Thompson, 1978) (Margolis, 1986) (Kliger, 1978a, 1978b) (May & Tanner, 1979). Advanced Technology and Research used hybrids to build the Walt Disney World monorail (Figure 1-1). The monorail shells were made of 95% glass fibers and 5% carbon fibers (Greene, 1999b).

Figure 1-1: Walt Disney World monorail (Blog, 2010)

Between 2000 and 2004, the Advanced Railway Research Center (ARRC) in the UK and 18 partners from 11 countries established a hybrid composite production (HYCOPROD) project to study the implementation of large sandwich structure production by developing feasible and cost-effective manufacturing methods for mass production of large sandwich structures for the transportation industry; this industry requires high impact resistance and predictable failure structures for buses, trams, trains, trailers and containers. "*Therefore, seven demonstrator vehicles and components were designed and manufactured within HYCOPROD. These included a rail vehicle cab and carriage end, a refrigerated semi-trailer, a bus door and bonnet, a tram bumper, and a horse box. Overall, these demonstrators validated the anticipated benefits of composites in terms of light weight, parts reduction and improved crashworthiness. Furthermore, a majority of the demonstrators were estimated to be cheaper, or no more expensive, than conventional metallic solutions*" ("NewRail, The Center for Railway Research at Newcastle University").

Corrosive marine working environments motivated the marine industry to rapidly convert from using heavy, costly, labor intensive and high maintenance metallic structures to composites. Hybrid composites play a major rule in marine structures where impact resistance, high corrosive resistance, high strength and pre-failure prediction are critical for public and environmental safety. Racing powerboats, sailing boats, canoes, kayaks, jet skis, fishing boats, ferries and submarines are currently manufactured using mono fiber sandwich panels or hybrid sandwich panel structures.

The use of sandwich panel structures in marine applications goes back to the 1970s, when designers realized the advantages of using cross-linked PVC foam and end-grain balsa as core materials that exhibited better flexural performance thank thick laminates (Greene, 1999b).

The aerospace industry is known as the leading composite developer and user among other industries. Since 1903, when the Wright brothers developed the first fiber-wrapped wing airplane that was considered the first motor-powered flying object, these fibers were treated as a key material in aircraft structures. Over the past three decades, composites have rapidly replaced metals in building commercial airplanes.

Hybrid composites can be found in parts where the material's high modulus is less critical. Historically, hybrids have been in used in Grumman US Navy F14 overwing fairing (Figure 1-2) with graphite and woven glass/epoxy skins and molded boron epoxy caps over an aluminum honeycomb core. This led to a 25% reduction in weight and a 40% reduction in cost compared to the equivalent metal structure (Hadcock, 1974).

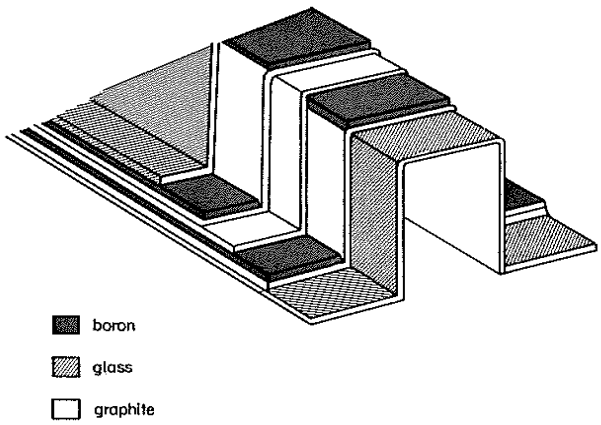

Figure 1-2: The Construction of the overwing fairing of the F-14
(Short & Summerscales, 1979)

(Hess, Huang, & Rubin, 1977) proposed the use of glass fiber strips as a crack arrestor in carbon aircraft structures to improve the aircraft crack propagation resistance without exceeding the design weight limit. This slightly increased the cost but considerably reduced the structural shear failure.

Some parts of fighter aircrafts were made using boron-graphite composite; through their Composite Flight Wing Program, McDonnell proposed a 50% reduced weight hybrid wing model that met improved performance requirements such as reduced drag, low radar observability and increased resistance to temperatures generated at high speeds (Greene, 1999b). Navy fighters F-18A graphite skins are separated from the aluminum framing with fiberglass layers to withstand the galvanic corrosion influenced by the salty, humid and sulfur-rich surrounding environment (Greene, 1999b). In modern commercial aircrafts, Aramid Reinforced Aluminum Laminate (ARALL), Glass Fiber Reinforced Aluminum (GLARE) and titanium graphite laminates (TiGr) are hybrids that are commonly used in building aircraft fuselages.

Recent studies in civil engineering have shown a great potential for using composite structures in this field. Restoring and repairing old, corroded and decayed columns is achieved using fiber wraps applied around the affected columns in several layers to extend the columns' operative life by protecting them from harsh environmental conditions (Greene, 1999a).

Hybrid civil structures are essentially made by combining conventional building materials such as wood, steel and concrete with fibers, especially in beams, pipes and columns, to improve the strength, fatigue life, weight reduction, corrosive resistance and vibration damping of the structures. The first and the only composite hybrid pedestrian bridge was built in Okinawa, Japan, in 2001 (Figure 1-3). Due to the corrosive environment influenced by the nearby ocean, a hybrid carbon/glass structure was chosen for the bridge's girders (Nunna et al., 2012). Other bridges that were partially made using composites and hybrid composites are found in Sherbrook, Quebec, and Headingly, Manitoba, as shown in Figure 1-4.

Further studies on composite structures in civil engineering fields have been investigated by several researchers. Bridge decks, walls, and roofs made from composite sandwich structures show promising potential for replacing conventional concrete structures (Keller, Rothe, Castro, & Osei-Antwi, 2014; Sharaf & Fam, 2012); (A. C. Manalo, Aravinthan, Karunasena, & Islam, 2010).

Figure 1-3: Okinawa All Hybrid Pedestrian Bridge (Nunna, Chandra, Shrivastava, & Jalan, 2012)

(a)

(b)

Figure 1-4: (a) The Joffre bridge in Sherbrooke, QC. (b) Tylor bridge in headingly, MN

As a modern building material, composite sandwich structures are currently used to build residential and commercial accommodations and are gradually replacing conventional concrete and wooden structures (see Figures 1-5 and 1-6). A standard or stiffened sandwich panel made from glass fiber reinforced gypsum (GFRG) or concrete (GRC) with filled or hollow cores are now used for their distinct advantages. The economical, cost-effective, environmentally friendly and easy-to-install sandwich panels are a good choice in countries where the conventional construction materials are expensive and their resources are less available. As shown in Figure 1-7, the ability to use different types of filling cores gives the sandwich panels the advantages of thermal and sound insulation and additional strength. Composite sandwich panel or wall manufacturers claim that their materials can save up 27% of the total construction cost due to the savings on steel, cement, water, bricks, timber and labor costs. This might also be true because the sandwich panel walls were designed to require less labor, less materials and less time. In addition, each wall was designed to bear the loads from additional construction above, such as in multistory buildings. The walls can withstand a major compression load that may otherwise lead to buckling failure. Similarly, the sandwich panels used as the floors for the first level and upper levels should resist the bending loads generated from the dead and live loads without any deflection beyond the tolerance limits. Thus, it is highly important to avoid any contractual failures, including buckling and deflection.

.

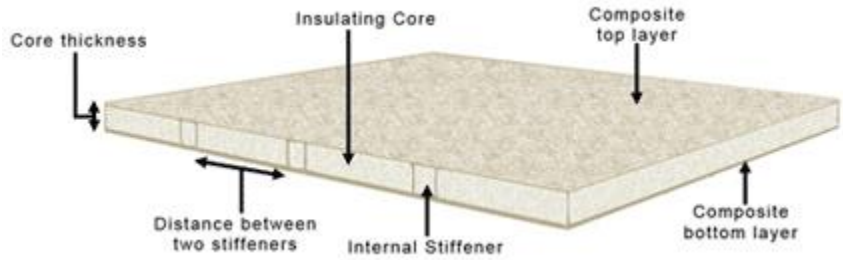

Figure 1-5: Composite sandwich panel (wall) (Inovatec Systems, 2016)

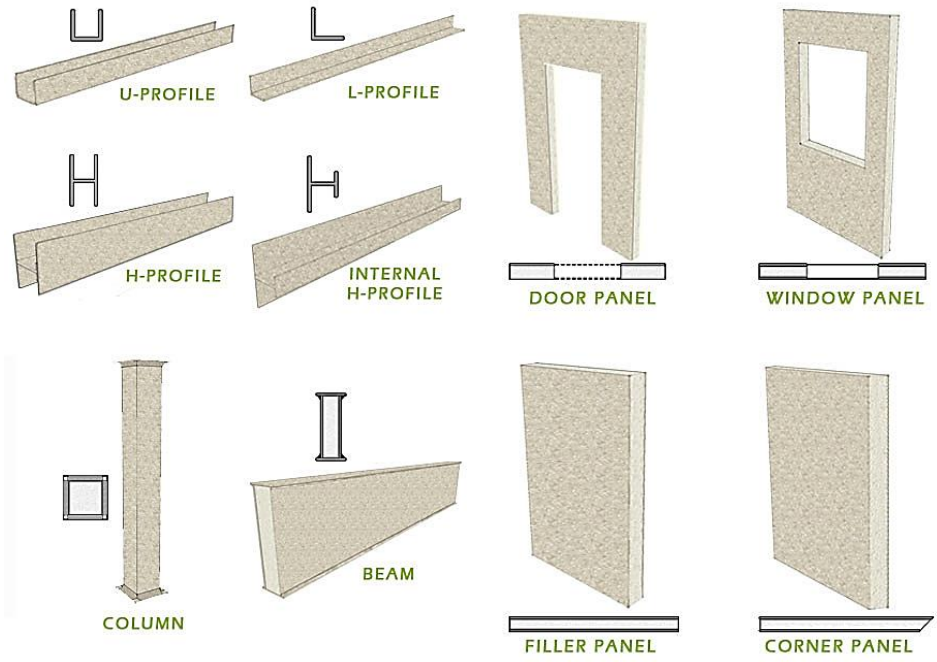

Figure 1-6: Sandwich panels sections (Inovatec Systems, 2016)

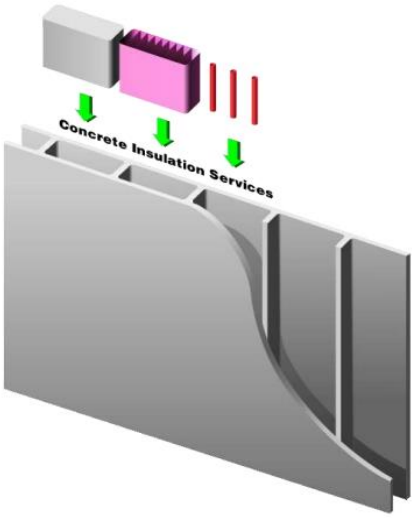

Figure 1-7: Hollow sandwich panel with filling options (Construction, 2016)

The GFRG and GRC sandwich panel face sheets are made from either chopped glass fibers or glass fiber plies imbedded with gypsum or concrete along with resin and special chemical additives. The face sheets are then molded in huge steel molds and left to cure. After curing, the sandwich panels are cut according to the design instructions and then transported to the job site for assembly (see Figure 1-8). Most of the completed projects are two- or three-story buildings. However, a nine-story building can be constructed by filling the core gaps with cement, as shown in Figure 1-9. (Mastali, Valente, Barros, & Gonçalves, 2015) tested hybrid sandwich panel slabs to be used in replacing damaged masonry slabs in old buildings. The slabs were made with Deflection Hardening Cement Composites (DHCC) as an upper face sheet, a GFRP lower face sheet, GRFP rib inserts between both face sheets and a foam core. Under flexural loading, the hybrid slabs performed better than conventional masonry slabs in terms of the loading capacity to dead weight ratio. (Wang, Liu, & Hui, 2014) manufactured and tested a full-scale column made from GRFP face sheets and Paulownia wood as the core using VARTM. The tested columns had two diameters (D =550 mm and D = 580 mm) and an equal height of 4 m. They noticed that the face sheet thickness had an effect on the column failure modes, which showed as an outer face sheet buckling failure in the less thick face sheets and compressive failure in the columns with thicker face sheets.

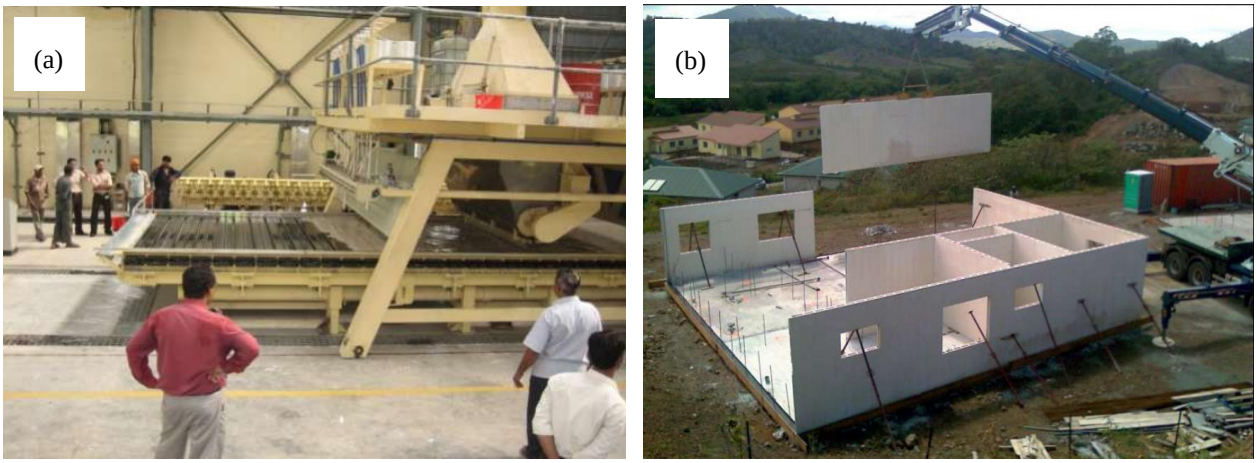

Figure 1-8: (a) manufacturing sandwich panels. (b) Sandwich panels assembly (Inovatec Systems, 2016)

Figure 1-9: two and multi storey buidlings made from sandwich panels walls (Construction, 2016)

In offshore hydrocarbon production, hybrid carbon/glass fibers submarine pipelines are used due to their weight, resistance to corrosion and mechanical performance. "*Circumferential carbon fibers provide resistance to external pressure, and longitudinal glass fibers provide lengthwise flexibility*" (Summerscales, 1987).

Wind turbine rotor blades are fabricated entirely from hybrid carbon/glass epoxy laminates or sandwiches, similar to helicopter rotor blades, to endure the flexural and torsional loading produced

by the rotary motion required to generate clean energy (Figure 1-10). The need for more cost savings in manufacturing rotor blades led to many studies investigating the possibility of substituting expensive carbon fibers with less expensive basalt fibers without affecting the blades' structural performance (Griffin, 2004).

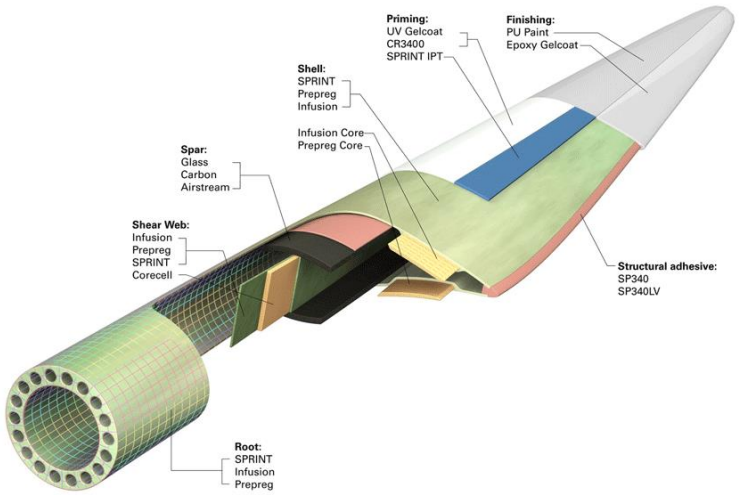

Figure 1-10: Wind rotor blade structure (Griffin, 2004)

Old reports studied the use of hybrids in medical prostheses. (Johnson, 1978) designed a prosthetic limb made of glass/carbon laminate coupled with steel hinges and brackets. The assembly method for the tap screw and epoxy resin adhesive joints was easy to prostheses users. Cuirasses, also known as portable iron lungs, have also benefited from the high impact resistance and energy absorbing property of composites compared to the ones made from carbon fibers alone (Phillips, 1976). Highly efficient, safe and light weight Ankle Foot Orthosis (AFO) are made from hybrids instead of the costly pure carbon fibers or pure glass fibers that failed in flexural fatigue (Figure 1-11(a)). The US Army is currently developing new, lighter helmets designed for the Future Force Warrior (FFW) made from high toughness and stiffness carbon/thermoplastic layers merged with aramid/thermoplastic layer to endure more ballistic and impact resistance and wear resistance;

these new helmets would replace the current PASGT helmets that are made of aramid thermosetting laminate (Thomas & Cramer, 2008; Walsh, Scott, & Spagnuolo, 2005). Hybrid compact ballistic helmets (Figure 1-11 (b)) supplied by Morgan Advanced Materials are used by the Canadian Forces for their light weight and high ballistic performance.

Figure 1-11: (a) Hybrid AFO (Composite, 2016), (b) Hybrid compact ballistic helmets used by the Canadian Forces (Materials, 2016).

Experimental research on hybrid composites performance showed an unexpected variation in the mechanical performance of hybrid laminates resulted from changing the glass and carbon plies positions within the laminates. This unexpected variation in performance was theoretically explained as “Hybrid Effect” and up to date many research including this project are trying to test the hybrid effect and its benefits to the mechanical performance of composite materials.

1.1 Project Objective

The objective of this project is to study the hybrid effect of using woven glass/carbon fibers face sheets bonded to a rigid foam core manufactured by VARTM on the mechanical buckling performance. This objective will be achieved as follows:

a) Manufacturing baseline reference sandwich panels with all-carbon face sheets as the upper limit and all-glass sandwich panels as the lower limit and comparing them to hybrid sandwich panels. The hybrid panel face sheets will have the same carbon-to-glass ply ratio of 2:2 but with different stacking sequences of carbon and glass plies. The ratio between the carbon and glass provides six possible arrangements of carbon and glass plies within the face sheets. All sandwich panels are manufactured by VARTM to produce high quality sandwich panels with a good fiber volume fraction V_f and less resin rich and dry areas.

b) Experimentally testing the manufactured specimens using a designed buckling test and recording the load along with both the in-plane displacement and the out-of-plane deflection to verify the existence of a hybrid effect explained in Section 2.10.2.

c) Developing a finite element model to predict the critical buckling load P_{cr} and comparing its outcomes to the results obtained from the experimental and analytical approaches. The finite element validation could be extended to study other sandwich panels with different materials.

d) Studying the hybrid effect of different stacking sequences of carbon and glass interplies on the buckling and the out-of-plane deflection resistance.

e) Studying the hybrid effect and its influence to the complex buckling failure mechanism and defining the hybrid effect in relation to the critical buckling load P_{cr}.

Notably, there is limited literature on the buckling, compressive and flexural behavior of hybrid sandwich panels with woven face sheets. Moreover, to the author's knowledge, there is no literature available on the buckling behavior of hybrid carbon/glass sandwich panels with rigid foam cores, which is the focus of this project.

Research Problem/Question

What is the influence or added advantage of using hybrid glass/carbon on the buckling and post-buckling performance of a composite sandwich panel with a rigid foam core? The compression and flexural behavior have negative and positive hybrid effects, respectively; what hybrid effect do the sandwiches exhibit during buckling?

Thesis Structure

This section guides the reader through the research structure, methodology and the research work used to answer the research question.

Chapter 2: Literature Review

This chapter reviews the existing research related to the topics and techniques covered in this thesis. This chapter starts by reviewing the definition of composite materials and how to obtain their mechanical properties as an orthotropic material and some of their failure modes. An overview of the definition of sandwich structures and their distinctive flexural rigidity characterization against bending is presented. Composite structure manufacturing techniques and Vacuum Assisted Resin Transfer Molding (VARTM) are reviewed. The composite woven fabrics and their mechanical behavior under compression are discussed in this chapter. Sandwich panel buckling performance, failure modes, analytical predictions and numerical analysis are reviewed. A comprehensive view of composite hybrid theory and the hybrid effect is followed by a broad investigation of the work by other researchers in the last sections of this chapter.

Chapter 3: Experimental Procedure

The experimental procedure started by manufacturing a set of sandwich panels using the VARTM technique by infusing both face sheets simultaneously to overcome the problems of dry spots or resin rich areas. Several buckling test trials were performed on specimens with different aspect ratios until finding clear and measurable experimental out-of-plane deflection readings recorded by the non-contact laser sensors. After setting the dimensions of the test specimens, the

arrangements of the hybrid carbon and glass fiber layers for the specimen face sheets were designated into six different hybrid face sheets with different stacking sequences of carbon and glass fiber layers with maintaining a 2:2 ratio of carbon to glass fibers. A standard flexural 3-point bending test was performed to investigate the effect of the six different hybrid sandwich panels on the specimens' flexural yield and ultimate performance. Moreover, the test was used to validate the analytically calculated mechanical properties of the hybrid face sheets by plugging them into a linear numerical model and plotting them together, as discussed in Chapter 4. The buckling test setup was designed to fix the specimens' short edges and to apply a controllable compressive in-plane displacement until failure. The gathered out-of-plane (deflection) data were recorded by the non-contact laser sensors, and the in-plane and out-of-plane results were plotted against the applied compressive load and analyzed.

Chapter 4: Numerical Modeling

Two different models were constructed: one to simulate the flexural 3-point bending test and the other to simulate the non-linear behavior of the test specimens' middle point deflection recorded by the non-contact laser sensor. The material properties were obtained for each hybrid face sheet by entering the different stacking sequences of carbon and glass layers into the FEA commercial package ANSYS APDL V 13.0. The first model was a combination of Equivalent Single Layer (ESL) and Discrete Layer (DL), and its results were compared to the experimental results from Chapter 3. The second model was constructed as a 2D section using the ESL method and Newton-Raphson non-linear equations to solve the model non-linearly. The numerical outputs were then analyzed and compared to the experimental results.

Chapter 5: Analytical, Experimental and Numerical Results

This chapter summarizes the key analytical, experimental and numerical results and how they could answer the research question. A comprehensive conclusion of the research results and their contribution to the industry are discussed. Additionally, further recommendations on supplementary research work are also provided.

CHAPTER 2 LITERATURE REVIEW

2.1 Composite Materials

The consolidation of fibers made from carbon, glass and synthetic polymer with a polymeric matrix creates polymeric reinforced composite structures. These composite structures are generated by stacking several fiber plies on top of each other to form a laminate, as shown in Figure 2.1. Depending on the angle θ between each ply's fiber orientation (local coordinate) and the laminate global coordinates, the Classical Laminate Plate Theory (CLPT) can be used to obtain the laminate global stiffness. Hence, for a specific laminate with a particular stacking sequence of fiber plies and ply thicknesses, the laminate's global stiffness can be determined by calculating the A, B and D matrices, as shown below.

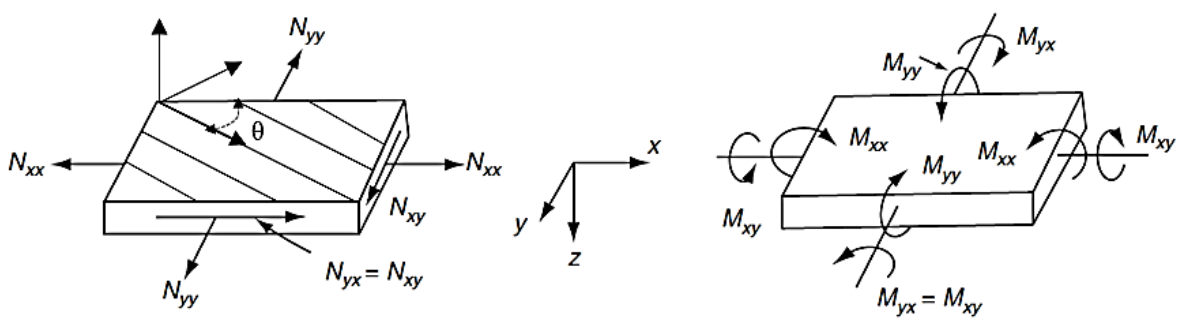

Figure 2-1: Forces acting on a composite lamina (Hyer, 1998)

$$\begin{Bmatrix} N_x \\ N_y \\ N_z \\ M_x \\ M_y \\ M_z \end{Bmatrix} = \begin{bmatrix} \begin{bmatrix} A_{11} & A_{12} & A_{13} \\ A_{21} & A_{22} & A_{23} \\ A_{31} & A_{32} & A_{33} \end{bmatrix} & \begin{bmatrix} B_{11} & B_{12} & B_{13} \\ B_{21} & B_{22} & B_{23} \\ B_{31} & B_{32} & B_{33} \end{bmatrix} \\ \begin{bmatrix} B_{11} & B_{12} & B_{13} \\ B_{21} & B_{22} & B_{23} \\ B_{31} & B_{32} & B_{33} \end{bmatrix} & \begin{bmatrix} D_{11} & D_{12} & D_{13} \\ D_{21} & D_{22} & D_{23} \\ D_{31} & D_{32} & D_{33} \end{bmatrix} \end{bmatrix} \begin{Bmatrix} \varepsilon_x \\ \varepsilon_y \\ \gamma_{xy} \\ k_x \\ k_y \\ k_{xy} \end{Bmatrix}$$

2.2 Composite Inter-Laminar Failure Modes

The manufacturing process of the composite structure starts by impregnating the fibers with a bonding matrix and letting them cure inside or outside the ovens. During the curing process, the matrix transforms from a liquid form to a polymerized solid form over time, giving the composite structure improved mechanical properties. As a result of the differences between the thermal expansion coefficients of the fibers and the matrix, fiber misalignment and the matrix shrinkage factor, residual stresses occur. This leads to initial microscopic cracks and local debonding zones inside the structure. These micro-cracks start to propagate in length and number and become visible after loading the structure for the first time. When the load increases, the cracks transform to a visible failure zone through the structure thickness and cause inter-laminar fractures (Knops, 2008).

To study the inter-laminar failure modes and the mechanisms of polymeric composites, we need to study the effect of various stress-strain components on a small unidirectional element representing the composite laminate by considering the stress as a point acting on a homogenous fiber-matrix material.

It is obvious that fibers are stronger and stiffer than the surrounding matrix. Therefore, designers are recommended to avoid fractures by trying to align the fiber direction with the loading direction. Although the fibers are stressed more than the matrix, the transverse stress transferred to the surrounding matrix is usually 10 times smaller than the stresses acting along the fiber direction. This transverse stress can be easily resisted by the matrix (Hyer, 1998).

Herein, the composite failure modes to the flexural and buckling tests within the scope of this project are limited to tensile or compressive loading. Thus, the failure modes can be categorized into three types: fiber tensile fracture, fiber micro-buckling and fiber and matrix crushing.

2.2.1 Mode 1: Fiber Tensile Fracture

Tensile fracture occurs when a tensile load is applied along the fiber direction (direction 1) that exceeds the fiber’s load-carrying ability. After the first fiber fails, the load is transferred throughout the surrounding matrix to the neighboring fibers. Similarly, a second fiber will fail as the load

continues to increase, causing load redistribution between the intact fibers. As the load continues to increase, the fracture propagates, and the matrix as well as the remaining fibers fail rapidly in the “Domino Effect” (see Figure 2-2) (Hyer, 1998).

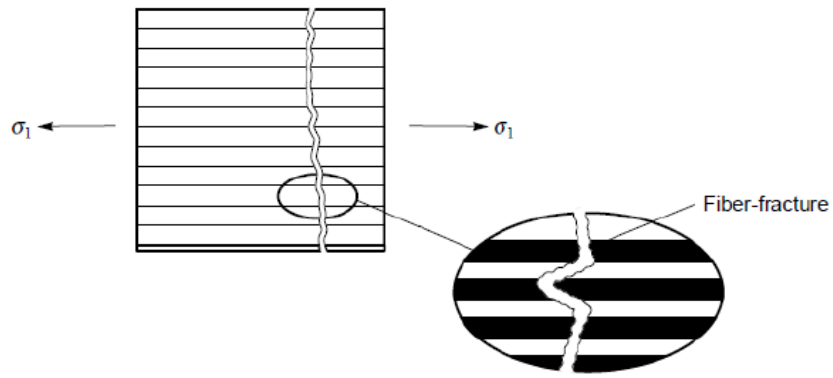

Figure 2-2: Fibre tensile fracture (Hyer, 1998)

2.2.2 Mode 2: Fibre Micro-Buckling "Kinking"

A compressive load along the fiber direction (direction 1) will cause a group or band (W, W= 10 to 15 fiber diameters) of localized fibers to buckle or kink with an inclined angle (β, β = 10 to 30º for most composites). This failure occurs as the matrix yields to restrain the fibers from buckling, and fiber fracture is located at the end of the kink. Fiber misalignment or waviness (ϕ) therefore has a huge impact on the materials’ ability to resist fiber micro-buckling and fiber-direction compressive loads. However, fibers often fail in compression in fiber crushing before the matrix yields and results in kinking, as shown in Figure 2-3 (Hyer, 1998).

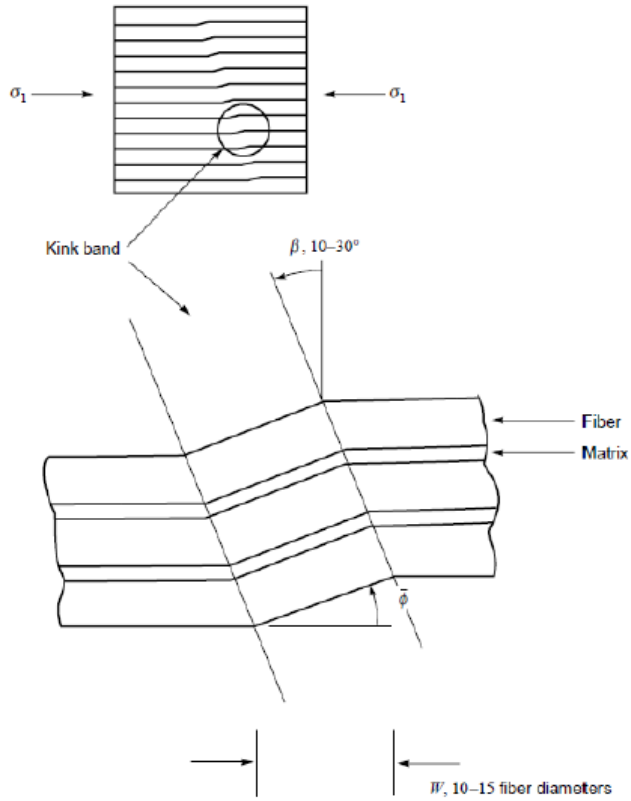

Figure 2-3: Fibre micro-buckling failure (Hyer, 1998)

2.2.3 Mode 3: Fibre and Matrix Crushing

Directions 2 and 3 in the unidirectional composites are weaker than the strength along the fiber direction. Therefore, by applying a compressive load in the direction 2 or 3, perpendicular to the fiber direction, compressive failure will occur due to matrix and fiber crushing, as shown in Figure 2-4. However, the compressive strength in direction 2 or 3 is greater than the tensile strength in the same direction (Hyer, 1998).

Additionally, the material could also fail with the same uniaxial lateral compressive load in a fracture plane oriented ± 54º to the uniaxial load. This behavior can be seen in composites similar to brittle materials such as gray cast iron and concrete, as shown in Figure 2-5 (Hyer, 1998).

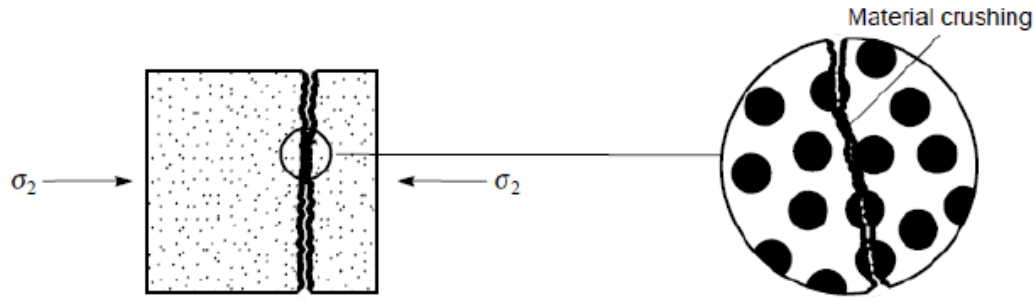

Figure 2-4: Fibre and matrix lateral crushing failure (Hyer, 1998)

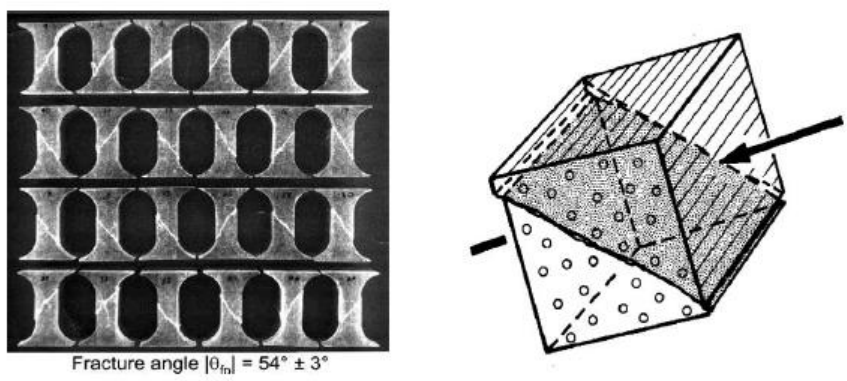

Figure 2-5: Fibre and matrix crushing failure at ± 54º (Hyer, 1998)

2.3 Composite Sandwich Structure

Sandwich structures are made by bonding, adhering or welding two relatively thin face sheets to one thick but very light core material, as shown in Figure 2-6. In composite sandwich structures, the face sheets are made from a composite lamina containing a single-fiber or multi-fiber layers such as carbon, glass or aramid embedded to a polymeric matrix. The light weight core between

the face sheets is commonly made from balsa wood, aluminum honeycomb, Nomex™ honeycomb, Polyvinyl Chloride (PVC) foam or Styrene Acrylonitrile (SAN) foam.

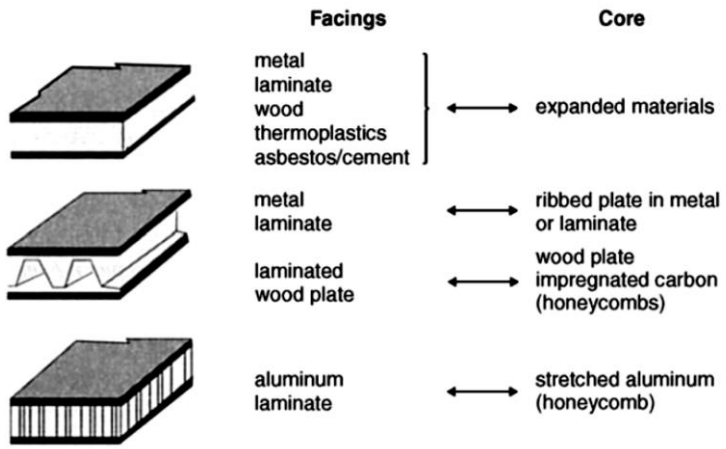

Figure 2-6: Sandwich structure (Gay, Hoa, & Tsai, 2003)

The added advantage of using a composite sandwich structure is remarkable. The structural weight reduction and higher flexural rigidity are very important for design. Moreover, composite sandwich structures offer also good thermal insulation characteristics depending on the core material type. Structurally, sandwich structures behave similarly to an I-beam: the faces act as the I-beam's flanges in resisting the maximum tensile and compressive stress, while the core resists the shear stress as the I-beam's web (Gay et al., 2003).

2.4 Sandwich Panel Flexural Rigidity

The separation between the two face sheets increases the moment of inertia, which also increases the structure's flexural rigidity. Therefore, this increase also reinforces the structure's resistance to bending loads and reduces the out-of-plane deflection. Figure 2-7 shows the increased flexural rigidity (stiffness) by only increasing the core thickness compared to the insignificant increase in total structural weight. This trade-off between a minor increase in total weight and a large increase

in flexural rigidity shows the benefits of using sandwich panels in many application where bending resistance is extremely desirable (Gay et al., 2003).

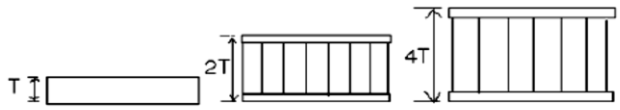

Relative Stiffness	1	7	37
Weight psf	0.910	0.978	0.994

Note: Skin thickness is the same for all examples and overall thickness doubles.

Figure 2-7: Flexural rigidity, lamina vs. sandwich structure (Gay et al., 2003)

Theoretically, the flexural rigidity of sandwich panels is driven from the second moment of inertia equation for face sheets with thickness *t* and core thickness *c*, as shown in Figure 2-8.

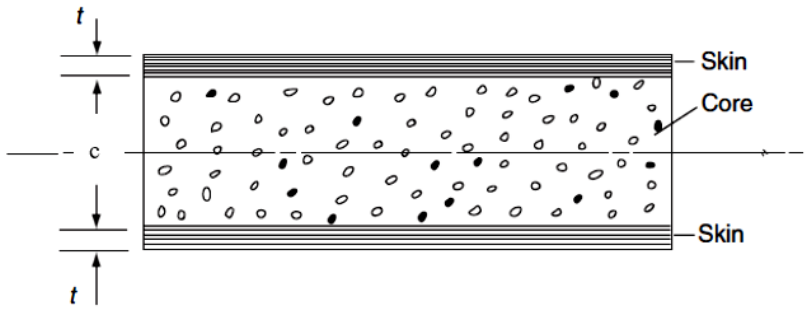

Figure 2-8: Cross section of a sandwich structure (Mallick, 2007)

Thus, the flexural rigidity $(EI)_b$ can be calculated from the following equation:

$$(EI)_b = E_s \frac{bt^3}{6} + 2bE_s t \left(\frac{c+t}{2}\right)^2 + E_c \frac{bd^3}{12} \qquad \text{(2-2) (Mallick, 2007)}$$

where,

Es = modulus of the face material

Ec = modulus of the core material (Ec <<<< Es)

b = Sandwich width

t = Face thickness

d = Core thickness

2.5 Composite Manufacturing

Composite parts or structures are made by directly imbedding the fibers with the matrix to fabricate the finial work piece or product. Unlike metallic structures, finished composite products usually bypass conventional transformation processes such as cutting, welding, drilling or forming. Hence, composite manufacturing methods take completely different approaches for producing composite products. The most common composite manufacturing methods used by the industry are hand lay-up, filament winding, pultrusion, liquid composite molding and thermoplastic composites. The production of finished composite products by combining the fibers and the matrix goes through four manufacturing steps (see Figure 2-9):

- Step (a): Composite main materials can be categorized into dry and liquid materials. The dry materials are exemplified by the fibers that can be found in the form of a fiber bundle, filaments or woven/braided fabrics, while the liquid part usually refers to thermoset resins or thermoplastics in grainy form.
- Step (b): At this level, a prepreg or a towpreg is formed by combining the thermoset or the thermoplastic matrix, respectively, to the fibers to form a single layer called a lamina.
- Step (c): By piling several composite layers on top of each other, a laminate is formed.

- Step (d): This stage represents the final composite product in its finished shape.

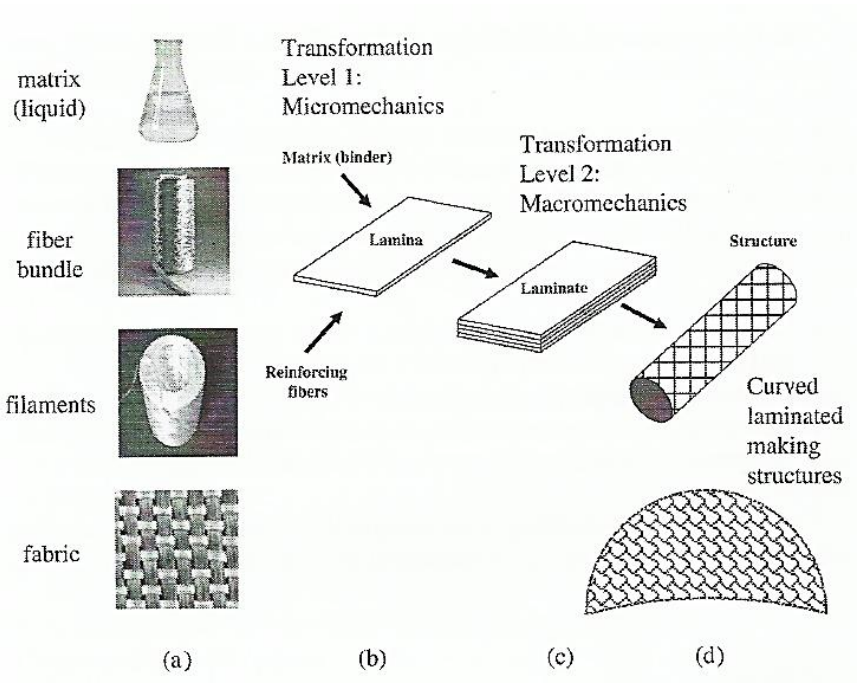

Figure 2-9: Steps of Manufacturing composites (Hoa, 2009)

2.6 Sandwich Panel Manufacturing

The production of a good quality sandwich panel is mainly related to good adhesion between the core and the face sheets. The achievement of a good bond between the composite face sheets and the core is the most difficult manufacturing aspect (Lee, Lee, & Oh, 2004). Therefore, the adhesion quality has a huge effect on the sandwich panel performance and failure modes. (A. Manalo, Aravinthan, Fam, & Benmokrane, 2016) summarized the commonly used sandwich panel manufacturing techniques as follows:

- Wet lay-up: In this technique, fiber impregnation with resin is performed either by hand lay-up or compressed air spray-up. The core is then placed between the wet face sheets and compressed inside a vacuum bag to remove the excess resin.

- VARTM: This simple and economical technique has been used since the 1980s and is known for producing good quality composite laminates with fewer voids and good mechanical performance (Mohamed et al., 2015). Moreover, this technique can be used to produce large and geometrically complex structures. The face sheet impregnation is achieved under a compressed and closed mold through the resin flow caused by the vacuum pressure difference between the resin inlet and outlet.
- Resin Transfer Mold (RTM): This technique uses resin direct injection through a two-sided rigid closed mold cavity to impregnate the face sheet fibers. This technique produces very good quality laminates with fewer voids and is suitable for mass production. However, the flexibility of this technique is limited to small sandwich panels.
- Adhesive bonding: This technique is achieved by bonding the already cured face sheets to the core's top and bottom faces. This bonding process involves the application of an adhesive layer between the core and the face sheets. The complete sandwich panel is then compressed by a weight or hydraulic pressure and cured inside an autoclave oven (Grünewald, Parlevliet, & Altstädt, 2015).

(Krzyzak et al., 2016) studied the effect of manufacturing sandwich panels with hand lay-up, hand lay-up-compress and autoclave techniques on the impact, compression and flexural performance. For all manufacturing techniques, two sandwich panels were made with face sheets either from E-glass mat or E-glass fabric. The autoclave manufactured sandwich panels had a better weight ratio of reinforcement than the hand lay-up and hand lay-up-compress panels, as reflected by their performance. In compression, the specimens failed at a strength rate close to the cores' ultimate strength due to the shear deformation between the core and the face sheets. However, the lowest compressive modulus was recorded for the specimen with fabric reinforcement that was manufactured by hand lay-up. Flexural tests showed a larger improvement in flexural strength for the hand lay-up specimens with mat face sheets than the other specimens due to "loosely placed fibers". However, this result is apparent as the specimens with mat face sheets that were twice as thick as those of the other specimens obviously had greater flexural rigidity. The autoclave specimens absorbed the impact energy much better than the hand lay-up specimens and marginally

better than the hand lay-up-press specimens. Moreover, fabric face sheets absorbed impact energy better than mat face sheets.

2.7 Vacuum Assisted Resin Transfer Molding (VARTM)

As a liquid composite molding manufacturing method, the VARTM manufacturing process has attracted attention recently due to its relatively economical tooling investment and its ability to produce geometrically complex structural shapes. Moreover, the low volatile emissions gained by the closed VARTM mold provides a safer and healthier working environment (Karlsson & TomasÅström, 1997).

The mold used in this process has only one hard side that is usually made from metal, glass or reinforced polymers, while the other open side is covered with a transparent vacuum bag. The preform is stacked in between layers of perforated release film and flow mesh media and is placed on top of the mold's hard side that was previously coated by a release agent to help perform demolding (see Figure 2-10). The resin flows and wets the already vacuumed mold from its inlets to the direction of the vacuum outlets under the low pressure vacuum. The complete wetting process start-to-end time depends on the perform permeability and resin viscosity. Resins with low viscosity and low perform permeability flow easily and wet the reinforcement stack faster than more viscous resins. The flow mesh media ease the resin flow through the stacked layers until it reaches the vacuum outlets before the resin reaches its gel time and stops flowing to avoid dry spots and resin rich areas. As the resin cures or crosslinks at room temperature, the production cycle tends to be too long, as most resin manufacturers recommend at least 24 hours of resin curing before demolding.

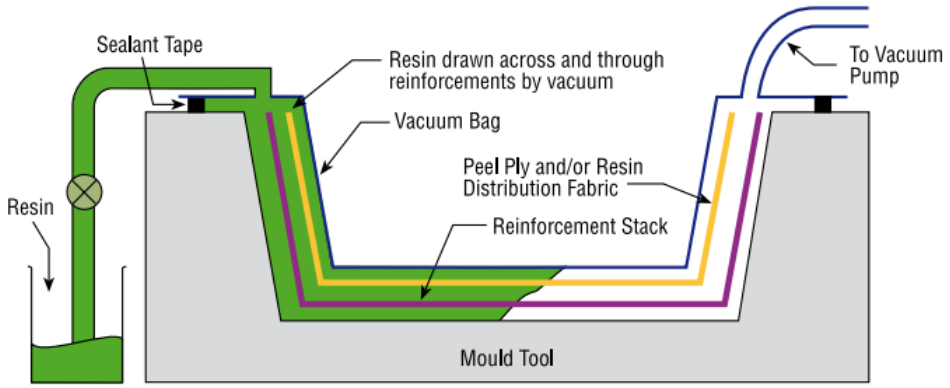

Figure 2-10: VARTM manufacturing set-up ("Gurit, GUIDE TO COMPOSITES,")

2.8 Woven Fabrics

Textile structure composites are fabricated from a single type or many types (hybrid) of fibers in the form of high modulus yarns. The fibers used in textile structure composites are usually made from glass, carbon or aramid fibers. Each type of fiber has its own distinct advantages and performance. The structural and geometric complexity of textile composites meet the need for easy-to-handle composite fabrics. Moreover, good fibers offer deep draw flexibility, dimensional stability and low cost, making textile composites more attractive to the industrial field (Naik, 1994). In recent years, carbon and aramid fibers have begun to be available in textile structure form along with the old textiles made from glass fibers. Composite materials made from woven textiles are commonly used in marine, aerospace and automotive industries due to their easy handling compared to unidirectional (UD) fibrous tapes. In addition, laminates made from woven fabrics provide better out-of-plane mechanical properties such as stiffness, strength and toughness than the tape fibers (Naik, 1994).

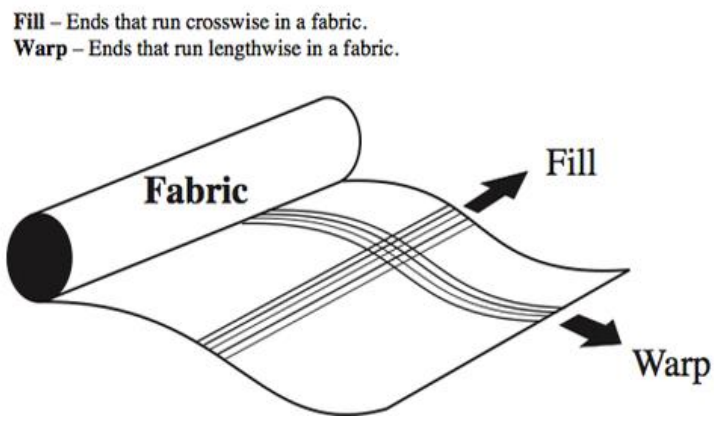

Figure 2-11: Wrap and fill directions in woven fabrics (Young, 2016)

A woven fabric is made by continuously weaving or interlacing yarns made by bundling a number of filament strands in two perpendicular directions (0°/90°). These two directions are known as warp and fill, as shown in Figure 2-11. The mechanical properties of the woven fabric greatly depend on the yarn count per unit length at the wrap and fill sides. As the yarn count number increases per unit length, the mechanical properties such as strength, stiffness and toughness improve. The interlacing process of weaving fiber yarns creates an interlocked undulation structure as the wrap yarns that are twisted on the fill yarns cause an initial fiber crimp. This initial crimp affects the laminate performance in many loading conditions. For example, in tension, the crimped fibers tend to straighten during the tension test, which stresses the surrounding matrix, causing it to fail earlier. Similarly, in a compression test, the pre-micro-buckled yarns stress the surrounding matrix, leading it to fail early. In addition to the fabric and resin stiffnesses, the mechanical properties of the composite lamina made from woven fabric are controlled by the laying orientation, fiber volume fraction and yarn size, count and crimp (Sevkat, 2009). However, it has been shown by (Lightfoot, Wisnom, & Potter, 2013) that the woven fabric failure mechanism is affected by the laminate lay-up procedure and can be minimized by improving the laminate stacking sequence and by reducing ply bridging and ply-ply adhesion.

Woven fabrics comes in many styles of weaving, but the most commonly used styles in the industry are plain woven fabric, 5-harness satin and 8-harness satin (see Figure 2-12). Plain woven fabric provides a balance between performance at both the wrap and fill sides as the number of yarn

counts is equal on both sides. However, plain woven fabric is not easy to drape, and because of the high crimp level of the yarns, the mechanical properties are weaker than other weave styles. The satin style is formed when the yarns repeats itself in a pattern after a number of yarns cross over and under. Although the 5-harness and 8-harness satin fabrics have unequal yarn counts on each side of the fabric, they are preferable due to their lighter weight and ability to drape easily in molds with complex shapes and rounded edges ("Gurit, GUIDE TO COMPOSITES,").

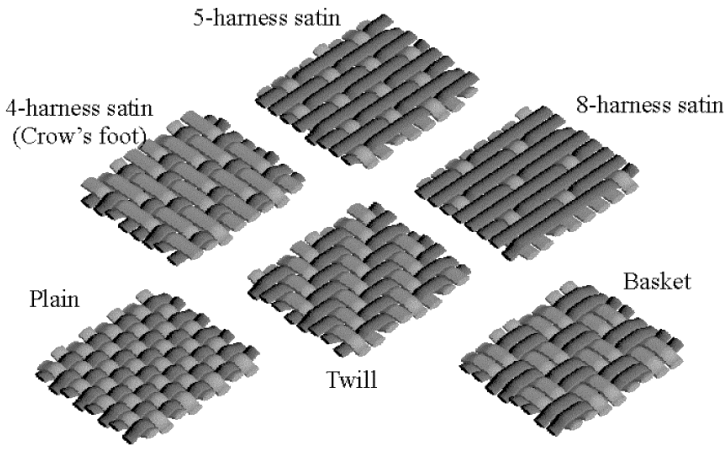

Figure 2-12: Some fabric woven styles (COMPOSITE MATERIALS HANDBOOK, 2002)

2.8.1 Woven Composite Fabric Mechanical Performance under Compression

The load bearing performance of woven fibers differs significantly from that of UD fibers. Hsiao & Daniel (Hsiao & Daniel, 1996) studied the effect of different fiber degrees of undulation on the compressive performance of composites with uniform fiber waviness against a uniaxial compressive load. The degree of undulation was defined as the fraction of the amplitude to the wavelength (A/L: see Figure 2-7), which was calculated for six different undulation configurations including straightened fibers with A/L = zero. The predicted stress-strain curve illustrated in Figure 2-13 shows a decrease in fiber strength as the degree of waviness (A/L) increases. Moreover, with the increasing A/L, the stress-strain curve non-linearity increases. Therefore, with a higher degree of undulation (A/L), the material will behave non-linearly due to the micro-buckling of the fibers.

Therefore, the material performance is also affected by reducing the material's ultimate strength, ultimate strain, modulus and early buckling.

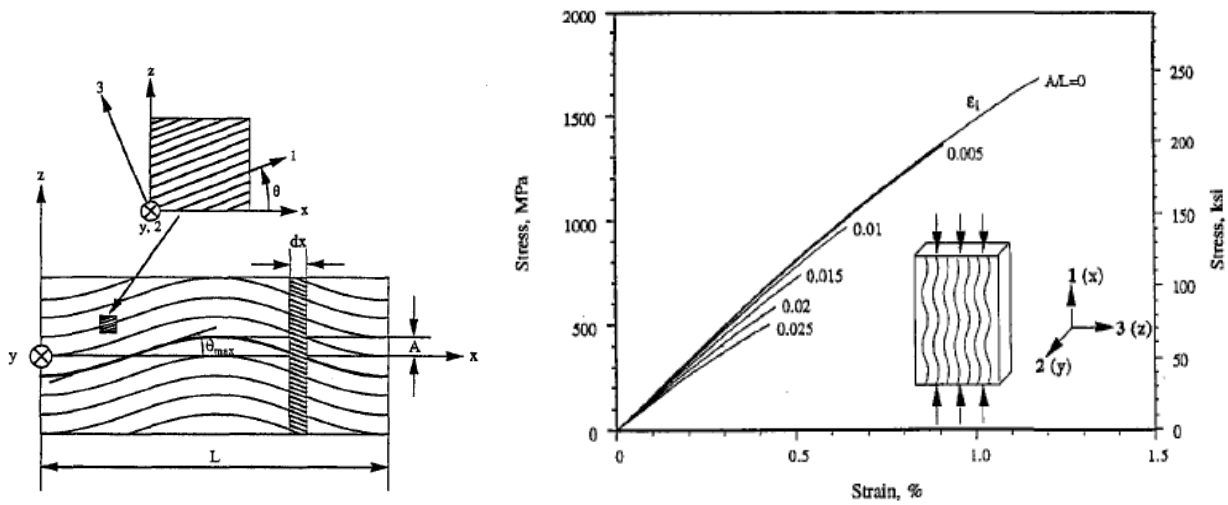

Figure 2-13: Performance of UD woven carbon fibre under compressive load (Hsiao & Daniel, 1996)

2.9 Composite Sandwich Buckling

Structural stability greatly depends on buckling resistance. Buckling occurs when a given structure loses its ability to support a compressive load that causes an out-of-plane deflection or distortion; that loading point is known as the buckling critical load P_{cr}.

2.9.1 Sandwich Panels Buckling Failure Modes

Sandwich panel failure modes are categorized into two main modes depending on whether the buckling occurs globally or locally. In case of the global buckling, the panel will fully bend and deflect away from its original loading axis. In local buckling failure, the failure occurs at a certain area or a point on the sandwich panel's face sheets or in between the panel's core and the face sheets. Examples of local buckling failure are shown in Figure 2-14: shear crimping, face sheet to

core delamination, core crushing or face sheet dimpling (wrinkling) in panels with honeycomb cores. It has been observed experimentally that buckling failure in sandwich panels can start as a global buckling failure that later transforms into one of the local buckling failure modes at a certain loading point, usually P_{cr} (Plates, 1971).

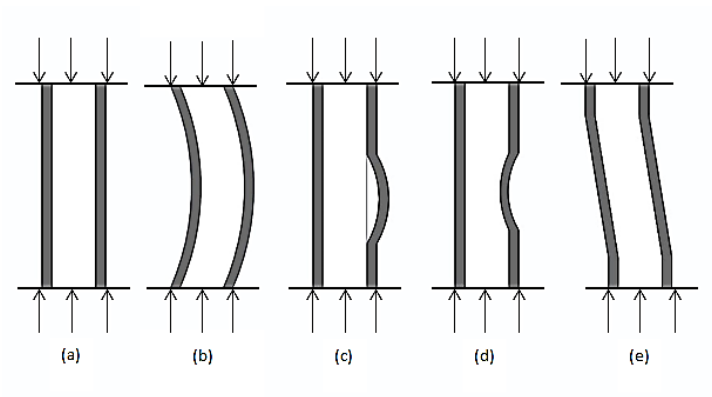

Figure 2-14: Sandwich Panels Failure modes under uniaxial compression load (a) specimen under uniaxial compression, (b) Global buckling, (c) local buckling (face sheet delamination), (d) Local buckling (face sheet crushing), (e) shear crimping

P_{cr} is the load at which the sandwich begins to buckle by forming an out-of-plane deflection w under a compressive load. Theoretically, the out-of-plane deflection starts to increase from w = zero at the moment when the load reaches P_{cr}, leaving the elastic range, and throughout the post-buckling (plastic) range until reaching fracture failure, as shown in Figure 2-15. However, experimental studies have observed an initial and additional out-of-plane deflection that is caused by imperfect specimen dimensions and test preloading or loading misalignment (Carlsson & Kardomateas, 2011). That is, the buckling failure showcases complex linear and non-linear relations between the applied compressive load and both the in-plane displacement and the out-of-plane deflection. In theory, the non-linear behavior starts instantly after the applied compressive load reaches P_{cr}. However, in practical experimental tests, the specimen imperfections cause an initial out-of-plane deflection that increases linearly proportional to the applied load compressive until reaching P_{cr}. This initial relation between the applied load and out-of-plane deflection curve is called the pre-buckling zone. After reaching P_{cr}, the sandwich panels start to buckle by exhibiting

a noticeable out-of-plane deflection away from the specimen's restrained edges, which increases non-linearly proportional to the applied compressive load. This zone in the load and out-of-plane deflection relation curve before fracture failure is called the post-buckling zone. The out-of-plane deflection can be measured by a dial gauge, digital deflectometer or a non-contact short range laser sensor (Carlsson & Kardomateas, 2011).

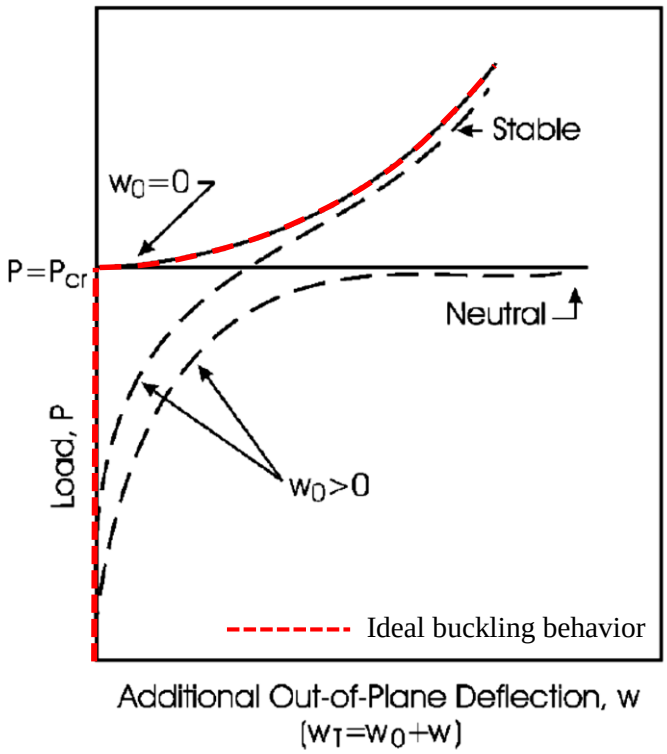

Figure 2-15: Bucking and post buckling stability and neutral behaviour (Carlsson & Kardomateas, 2011)

2.9.2 Analytical Buckling Failure Prediction

The critical buckling load P_{cr} responsible for initiating buckling failure in panels can be analytically predicted by applying the panels' mechanical properties to mathematical formulations developed by studies to calculate P_{cr} under compressive loading. The first buckling failure prediction was

developed by Leonhard Euler (1707-1783). His equation is applicable to only a column pinned at both ends and loaded with uniaxial compressive loading. Later, an extension to Euler's equation was performed to cover the other boundary conditions by adding a correction factor β, as shown in equation 2-3 and Figure 2-16. This correction factor represents the ratio between the column's buckled and non-buckled (zero-bending) lengths

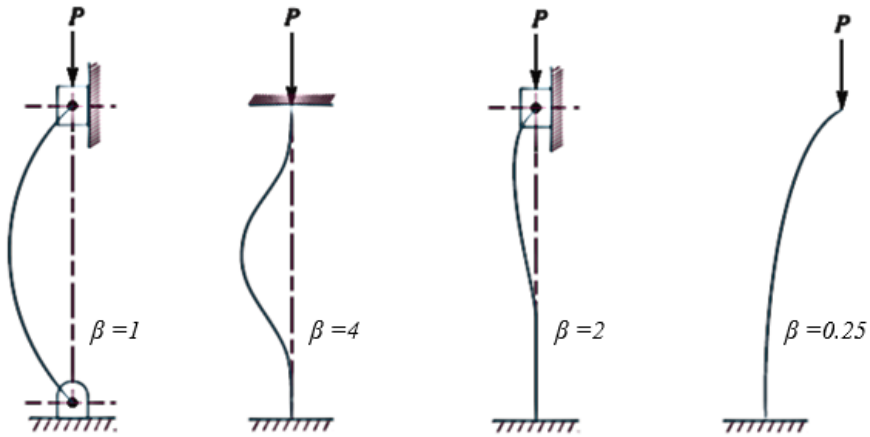

Figure 2-16: Euler's critical buckling fixing conditions (Khurmi & Gupta, 2005)

$$P_E = \frac{\pi^2 (EI)_b}{(\beta L)^2} \qquad \text{(2-3) (Khurmi \& Gupta, 2005)}$$

Further development of the Euler equation was presented by (Engesser, 1891) by adding the effect of transverse shear deformation for a prismatic straight column. Sandwich panels usually fail due to transverse shear deformation because of the large difference between the face sheets and the core strength and stiffness. Therefore, for sandwich panels, it is crucially important to include the effect of the transverse shear deformation when predicting P_{cr} because of its influence on the panel's resistance to failure. (Daniel, Gdoutos, Wang, & Abot, 2002) recommend focusing on developing the core materials to improve the sandwich structure performance, as these materials greatly influence the sandwich panel failure modes. (Haringx, 1948) derived an alternate infinite

buckling load prediction for column buckling with slenderness up to zero. However, the equations produced by Engesser and Haringx were derived from column cases, not for sandwich panels (Bažant & Beghini, 2004, 2006) investigated the previous theoretical predictions with experimental results produced by (Fleck & Sridhar, 2002) for sandwich panels with weak cores and concluded that the Engesser equations provided reasonable results. Another approach was developed by (Allen, 1969) with two quite simple equations: one can be used for panels with thin face sheets and the other for panels with thick face sheets. According to Allen, the face sheets are considered thin when c/t ≥ 5.35. Allen later observed that even for panels with thick face sheets, weak cores in shear and reduced slenderness, the equation for thick face sheets predicts P_{cr} better than the equation for thin face sheets. (Carlsson & Kardomateas, 2011) derived a mathematical elasticity system of equations to calculate P_{cr}. They also compared their solution to other equations and concluded that the Allen thick face sheet equation provided nearly identical results to their elasticity solution, as shown in Figure 2-17. Therefore, Allen's simple thick face sheet equation can provide sufficiently good predictions for sandwich panels.

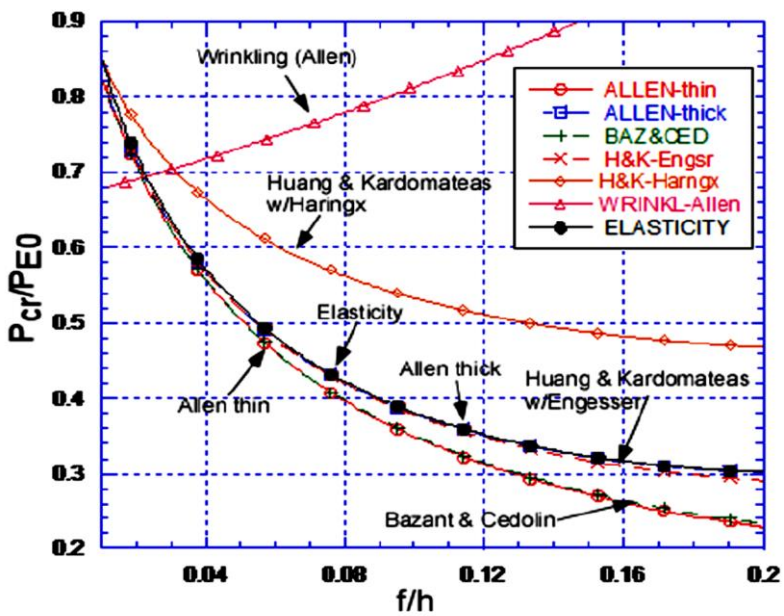

Figure 2-17: Comparison between different analytical solutions to solutions for Pcr (Carlsson & Kardomateas, 2011)

Another widely used approach for predicting P_{cr} is the Shear Deformation Plate Theory (SDPT). This approach draws from the texts of Allen, Plantema and Zenkert to calculate the deflection by adding the bending and shear deformation results together to obtain the total deflection. This approach was mathematically derived and simplified by (Carlsson & Kardomateas, 2011) with the following assumptions: thin face sheets, negligible in-plane stress in the core, and out-of-plane deflection that is independent from the z-coordinate. Therefore, there is good opportunity to compare the P_{cr} predictions from both the Allen Thick Face Sheet Theory (ATFT) and the Shear Deformation Plate Theory (SDPT) against P_{cr} from the experimental work in this study.

2.9.2.1 Allen Thick Face Sheet Theory (ATFT)

An approximate solution for calculating the panels' critical buckling load P_{cr} can be computed by equations (2-4, 2-5, 2-6, 2-7 and 2-8). These equations were developed by (Allen, 1969) for thick sandwich panels (see Figures 2-18 and 2-19). The sandwich can be considered thick if $c/t < 5.35$. In his approach to calculating the critical buckling load, Allen considered two correlated and simultaneously acting displacements during the buckling state. The first displacement is the bending displacement, which is resisted by the face sheets' different bending rigidity about their own centroid axis. The second displacement is created from the shear deformation (strain) of the core resulting from the uniform cross-sectional shear stress affecting the core during buckling. Therefore, additional shear deformation increases the face sheet bending displacement as they have to share the generated shear stress and the additional deflection.

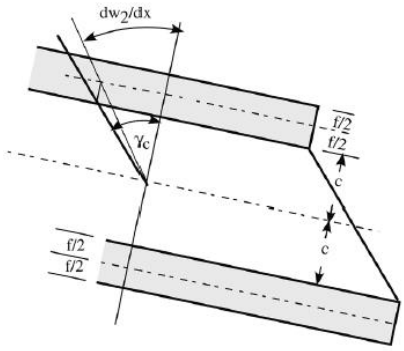

Figure 2-18: Schematic of the additional displacment due to transverse shear and core shear strain (Carlsson & Kardomateas, 2011)

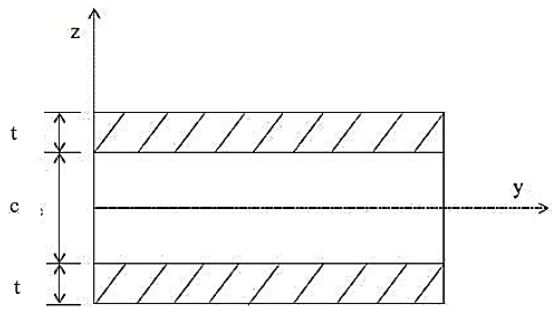

Figure 2-19: Allen thick sandwich

Therefore, due to its accuracy, Allen's thick face equations used in this study.

$$P_E = \frac{\pi^2 E I}{L^2} \qquad (2\text{-}4) \quad \text{(Allen, 1969)}$$

$$P_{Ef} = \frac{\pi^2 E I_f}{L^2} \qquad (2\text{-}5) \quad \text{(Allen, 1969)}$$

$$Pc = AG_c \qquad (2\text{-}6) \quad \text{(Allen, 1969)}$$

$$A = \frac{b(c+t)^2}{c} \qquad (2\text{-}7) \quad \text{(Allen, 1969)}$$

where P_E is the sandwich Euler load, P_{Ef} is the Euler load for the faces only, EI is the sandwich flexural rigidity, EI_f is the face flexural rigidity, A is the area of transverse shear and P_C is the shear buckling load.

The general equation to calculate the sandwich critical load is:

$$P_{cr} = P_E \left[\frac{1 + \frac{P_{Ef}}{P_C} - \frac{P_{Ef}^2}{P_C P_E}}{1 + \frac{P_E}{P_C} - \frac{P_{Ef}}{P_C}} \right] \qquad \text{(2-8)} \quad \text{(Allen, 1969)}$$

2.9.2.2 Shear Deformation Plate Theory (SDPT)

For Shear Deformation Plate Theory (SDPT), a compressive uniaxial load is applied to a rectangular, flat and symmetric sandwich panel. The compressed edge is then compressed by a uniform force N_x until a slight bent mode shape (buckling) is achieved, as shown in Figure 2-20 (Carlsson & Kardomateas, 2011).

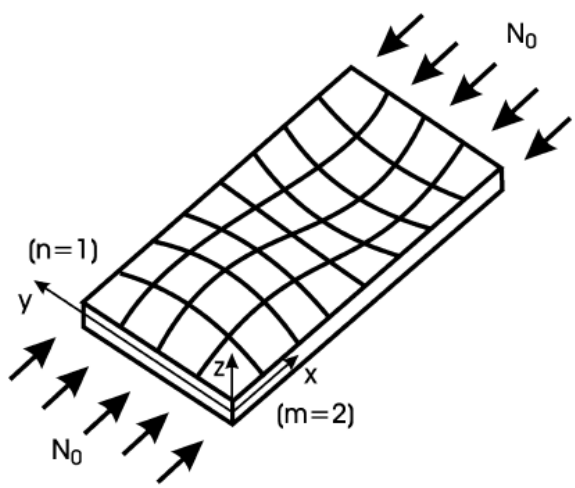

Figure 2-20: Uniaxial buckling load with n =1 and m=2 (Carlsson & Kardomateas, 2011)

From the equilibrium equations for the force and moment resultants represented by (Whitney, 1987), the final derived equation for the uniaxial load applied on a sandwich panel with isotropic core material ($G_{xz} = G_{yz} = G_c$) yields:

$$N_0 = c\left(G_{xz} + \left(\frac{n}{m}\right)^2 \left(\frac{L}{b}\right)^2 G_{yz}\right) - \frac{a^2}{\pi^2 m^2} F_{33} \qquad (2\text{-}9)$$

where

$$F_{33} = \pi^2 \left[\frac{m^2 c G_{xz}}{L^2} + \frac{n^2 c G_{yz}}{b^2} + \frac{n^2 N_x}{L^2}\right] \qquad (2\text{-}10)$$

The variables m and n are integers that represent the number of sine waves generated by the effect of the loading conditions on a panel's long and short edges, respectively, as shown in Figure 2-20.

2.9.3 Numerical Buckling Analysis

The buckling behavior of columns and panels under compressive load represents a clear case of geometric non-linearity. The gradual non-linear load increase against both the in-plane displacement and out-of-plane deflection curves shows the structural instability. The huge increase in the out-of-plane deflection accompanied by the small increase in the in-plane displacement indicates the occurrence of buckling in experimental compression tests. Therefore, to simulate the buckling behavior, a finite element (FE) model with non-linear numerical solver capabilities need to be used to simulate the relation between the load and the out-of-plane deflection.

The aim of building the static FE model is to simulate the buckling behavior of a column and/or a panel in order to obtain the P_{cr} responsible for the buckling failure and the buckling mode shapes. In addition, the model has to plot the relation between the applied compressive load and the out-of-plane deflection to compare these values to the experimental data registered by the non-contact

laser sensor. In most FE commercial packages, there are two types of buckling analysis: linear buckling, also known as eigenvalue buckling analysis, and non-linear buckling analysis.

The linear buckling analysis predicts the theoretical P_{cr} similar to the Euler solutions mentioned in Section 2.8.2 (Manual). Therefore, it is recommended, especially in this study, to disregard this type of analysis as it is limited to perfectly linear structures and does not consider structural imperfections. In contrast, the non-linear analysis provides nearly accurate results by analyzing the gradual load increase until structural instability occurs. Non-linear analysis can include the large deflection effect on the model, which is essential in simulating buckling models. The non-linear solver depends on solving the model in an iterative step-by-step manner. The solver starts with an initial iterative value to solve the problem. Hence, the solution contains an error estimate that can be used to adjust the current iteration to calculate the following iteration. This iterative process is repeated step-by-step until the error estimate becomes less than the defined threshold. In the same fashion, the non-linear solution uses an incremental solution. The load is divided and applied as load steps and solved in intermediate solutions obtained from the incremental load steps. The following load steps use the solution from the current load step with an error estimate; in the case of a high error estimate value, the load step is divided into smaller load steps. This repeated process continues until the solution diverges. The non-linear solver used in this study is part of the commercial FE package ANSYS V13.0. The solver uses the Newton-Raphson iteration method (Appendix A) to solve the non-linear problems in ANSYS.

2.10 Hybrid Composites

Hybrid composites are made by assembling two or more different fiber types, such as carbon, glass and aramid, merged together by a resin matrix to create a laminate. Hence, laminate hybridization yields unique laminate properties compared to the properties of each individual fiber component. When merging different types of fibers, having different fiber diameters does not affect the lamina's fiber content as the small fibers fill the gaps between the large fibers. Incorporating fibers with varying diameters increases the lamina's total fiber friction, which can improve the lamina's mechanical properties (Swolfs, Gorbatikh, & Verpoest, 2014). Hybrid composites are available in

two main forms that categorized based on the position of the fibers within the lamina plies: intra-ply and inter-ply hybrids (Short & Summerscales, 1979). An intra-ply hybrid lamina is formed when each fiber surrounds the other fiber type intimately, and they can be formed as a two-fiber or mixed fiber ply. The other inter-ply hybrids combine different types of fibers in the form of stacked plies, where each ply is made from one fiber type. The stacked inter-ply hybrids can be seen as an individual fiber ply or as a sandwich lamina with a face sheet made from one fiber type and a core made of a different fiber type. An illustration of the hybrid types is shown in Figure 2-21. Effectively, hybrid composites help designers to produce structures that feature "*balanced strength and stiffness, balanced bending and membrane mechanical properties, balanced thermal distortion stability, reduced weight and/or cost, improved fatigue resistance, reduced notch sensitivity, improved fracture toughness and/or crack arresting properties and improved impact resistance*" (Chamis & Lark, 1977). The use of hybrid composites is significantly efficient in applications where the longitudinal and lateral performances are critical to the application. In hybrid laminates, each fiber type contributes its own local performance advantages to the laminate's global performance and simultaneously eliminates unwanted disadvantages. Tailored hybrid performance advantages can be found in applications when reducing catastrophic brittle failure, such as by combining high modulus fibers with low modulus fibers. Hence, improvements in the hybrid moduli, elastic behavior and failure prediction are achievable (Chamis & Lark, 1977). This elastic behavior improvement is desirable in Structural Health Monitoring (SHM) systems for early damage detection (Swolfs et al., 2014).

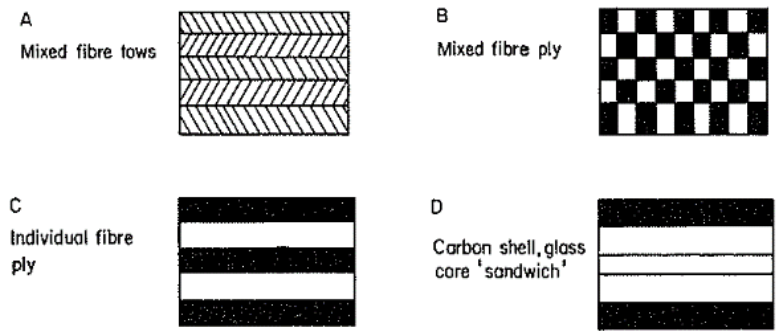

Figure 2-21: Types of hybrid composites (Short & Summerscales, 1979)

2.10.1 Hybrid Composite Theory

The elastic modulus E_c of a single fiber composite can be calculated by knowing the elastic modulus and volume fraction of the fibers (*f*) and the matrix (*m*):-

$$E_c = V_f E_f + V_m E_m \qquad (2\text{-}11)$$

The composite's total volume fraction must be unity:

$$V_c = V_f + V_m = 1 \qquad (2\text{-}12)$$

For a hybrid composite made from two types of fibers (*a* and *b*), equations (2-11) and (2-12) become:

$$E_c = V_a E_a + V_b E_b + V_m E_m \qquad (2\text{-}13)$$

$$V_c = V_a + V_b + V_m = 1 \qquad (2\text{-}14)$$

The value of the matrix stiffness is considerably small when compared to the fiber stiffness, and it does not contribute to the overall composite stiffness. Thus, V_m is neglected.

$$E_c = V_a E_a + V_b E_b \qquad (2\text{-}15)$$

Equation (2-15) assumes that the composite lamina fails when the Low Elongation (LE) fiber fails first and that the fiber strain failure is not distributable to the High Elongation (HE) fibers. In addition, the fractured fibers that fail become shorter than the critical length and are assumed to have no stress concentration effect on the fibers that have not failed. A representation of an equation (2-15) is illustrated in Figure 2-22; the dashed line (AD) is known as the Rule of Mixture (ROM).

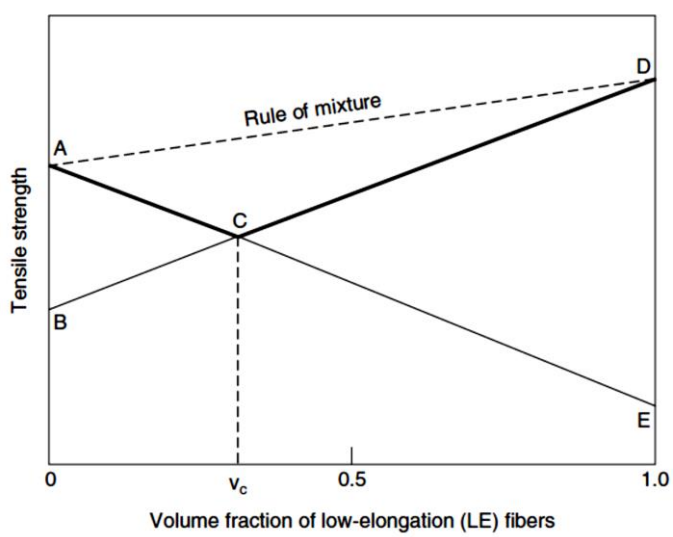

Figure 2-22: Tensile strength variation model in interply hybrid laminates (Mallick, 2007)

Two expressions for the tensile strength of a composite made from LE and HE fibers were proposed by (Hayashi, 1972). The first expression represents the strength of the hybrid correlated to LE

fibers (equation 2-16), while the second expression represents the strength of the HE fibers (equation 2-17):

$$\sigma'_c = V_{HE}\, E_{HE}\, \varepsilon'_{HE} \qquad (2\text{-}16)$$

$$\sigma'_c = V_{LE}\, E_{LE}\, \varepsilon'_{LE} \qquad (2\text{-}17)$$

In the AE line, the HE fiber strength starts from point A, where the fiber volume of the LE fibers equals zero, and ends at point E, where the fiber volume of the LE fibers is at its maximum (equation 2-16). Similarly, the DB line represents the strength of the LE fibers starting from its maximum volume fraction at point D to its zero volume fraction at point B (equation 2-17).

From equations (2-16) and (2-17), the predicted hybrid composite strength for different compositions when the HE fibers contribute to the composite's load-carrying capacity can be obtained by the following equations:

$$\sigma'_c = (V_{LE}\, E_{LE} + V_{HE}\, E_{HE})\, \varepsilon'_{LE} \qquad (2\text{-}18)$$

$$\sigma'_c = V_{HE}\, E_{HE}\, \varepsilon'_{HE} \qquad (2\text{-}19)$$

By setting equations (2-18) and (2-19) equal, the hybrid's minimum strength will occur at a certain point of the volume fraction:

$$(V_{LE}\, E_{LE} + V_{HE}\, E_{HE})\, \varepsilon'_{LE} = V_{HE}\, E_{HE}\, \varepsilon'_{HE} \qquad (2\text{-}20)$$

After further rearranging equation (2-20) becomes:

$$\frac{1}{V_{HE}} = \frac{1+E_{HE}}{E_{LE}}\left[\frac{\varepsilon'_{HE}}{\varepsilon'_{LE}} - 1\right] \qquad (2\text{-}21)$$

From equation (2-21), (Gunyaev, 1977) derived a mathematical expression in terms of failure due to stress. Thus, the calculated value is presented in Figure 2-22 as point C.

$$V_c = \left(\frac{1+\sigma_{HE}}{\sigma_{LE}} - \frac{E_{HE}}{E_{LE}}\right)^{-1} \qquad (2\text{-}22)$$

Therefore, the hybrid's minimum strength follows the elongation of the low strain fiber:

$$\sigma'_m = (1 - V_c)E_{LE}\varepsilon'_{LE} \qquad (2\text{-}23)$$

Experimental tensile tests on hybrid laminate show a smaller ultimate strength than the ultimate strengths of both LE and HE fibers. Due to the modulus and strength contribution of the HE fibers to the lamina ultimate strain rate, the ultimate strain of the LE increases. Therefore, the catastrophic failure of the LE fibers is retarded, and the hybrid lamina fails in a controlled mode. Conversely, the hybrid ultimate strain is less than the ultimate strain of the HE fibers. Moreover, the tensile hybrid modulus falls in between the values of the LE and HE moduli (See Figure 2-23) (Mallick, 2007).

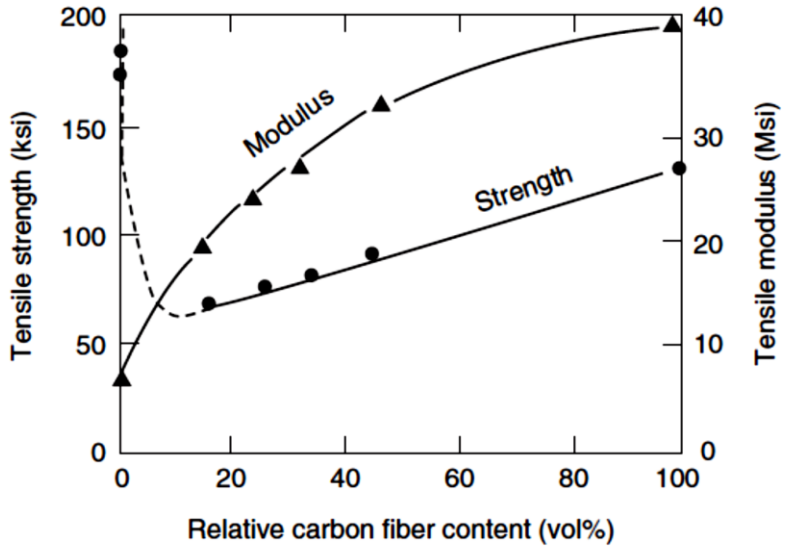

Figure 2-23: Variations of the tensile strength and modulus of a carbon/glass composite (Mallick, 2007)

2.10.2 Hybrid Effect

The hybrid effect was first defined by (Hayashi, 1972) in studies on the hybrid performance, examining the improvement of the failure strain value from the failure stain values of LE carbon fibers, as shown in Figure 2-24. His study reported a 45% increase in the hybrid's failure strain from the failure strain value exhibited by all-carbon fiber specimens. Hayashi's results and conclusions were encountered by several researchers who believe in the validity of the rule of mixture for hybrid composites. This argument ended in favor of Hayashi as later studies supported his hybrid theory over the rule of mixture (Swolfs et al., 2014). Another definition of the hybrid effect was later introduced by (Summerscales, 1983) as the deviation from the values represented by the rule of mixture in either positive or negative values (Swolfs et al., 2014). However, this simple definition could not be applied to all mechanical properties such as for bending conditions when the modulus remained almost constant for different glass/carbon stacking sequences within the lamina. In addition, some mechanical performance such as tensile strength is actually bilinear. (Swolfs et al., 2014) suggested advanced and complex theories such as the classical laminate theory

to define the hybrid effect. To date, there has been no universal agreement on defining the hybrid effect; this subject needs more collaborative advanced research in the hybrid composite field.

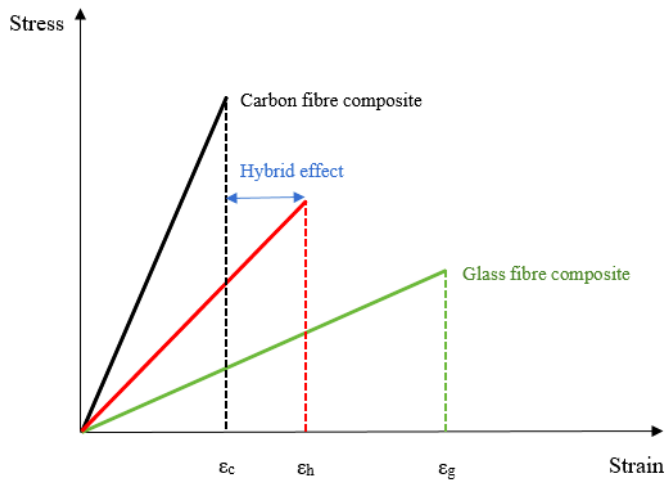

Figure 2-24: Hybrid effect as proposed by Hayashi

The HE formation was first hypothetically explained in UD composites by (Bunsell & Harris, 1974) as the result of the different thermal contractions between the fibers within the hybrid lamina. For example, during the crosslinking process of the matrix material, the temperature increases, causing the UD glass fibers to expand in length, while the carbon fibers remain nearly still. After full curing, the matrix gradually cools down to room temperature, causing the glass fibers to shrink back, while the carbon fibers remain at almost their original length. Therefore, residual stresses are generated internally, with the carbon fibers in compression and the glass fibers in tension; the interfacial shear stress between the fibers and the matrix occurs at zero load. Further research on the residual stress influence on the hybrid effect reported that the residual stress contributes only a maximum of 10% to the hybrid effect. (Manders & Bader, 1981) developed a statistical model for hybrid failure other than failure caused by thermal effects. They also discussed two more hypotheses for the HE formation in UD composite laminates. The first hypothesis was related to structural fracture mechanics (thermodynamics), and the second hypothesis was related to a statistical failure model. The fracture mechanics theory assumes that failure is a result of a

propagating pre-existing internal cracking zone. However, composite structures are inhomogeneous and anisotropic in their elastic and fracture performance. Thus, the first fiber failure does not lead to total structural failure because of the stress redistribution within the neighboring fibers through the matrix. In addition, the crack-included defect zone should be larger than the fiber diameter; therefore, the material behaves homogenously, correlated with fracture mechanics theory. The statistical failure theory assumes that all fibers are identical and are initially stressed evenly; failure occurs at a certain stress level by propagating from the weakest point inside the structure. They suggested the use of the Weibull distribution to model the fiber strength from the random sequential fiber failure determined from the weakest link. (Swolfs et al., 2014) discussed a forth possible hypothesis to explain the HE effect by reviewing the work of several researchers (Xing, Hsiao, & Chou, 1981); (Xia & Ruiz, 1991); (Hedgepeth, 1998) on the dynamic stress concentration of UD composites. Under dynamic loading and after fiber breakage, the fibers spring back to create a temporary stress concentration that is 15-27% higher than the static stress concentration as a result of the stress wave travelling along each fiber. This dynamic stress concentration was obtained using the shear lag approach developed by Hedgepeth. Further development of the Hedgepeth approach was used to obtain the dynamic stress concentration along the fiber length not only at the fiber breakage plane. In effect, the stress concentration factor obtained for glass fibers was 20% higher than that for carbon fibers, suggesting that each fiber type behaves differently. Another important model for hybrids consists of two rows of glass and carbon fibers that were theoretically studied by (Xing et al., 1981). Their model simulates the fiber breakage by propagating two independent, out-of-phase stress waves travelling through each fiber type, causing a lower stress concentration than those made from carbon fibers only. Thus, the hybrid effect should always be present.

2.10.3 Bridging Effect

The fiber bridging effect was used to explain the failure development in hybrid composites made from UD fibers (Kretsis, 1987). The HE fibers tend to bridge the broken LE fibers and arrest failure development. This delays the failure strain of the LE fibers and allows these fibers to continue their load-carrying ability as their weakest link is excluded. For example, a bundle of UD hybrid fibers

with a certain degree of dispersion is loaded uniformly under a certain loading condition. As the load increases, the strain also increases until one of the LE fibers loses its load-carrying ability and breaks. This fiber breakage creates a radial stress concentration failure zone as the stresses redistribute to the neighboring fibers. The resulting stress redistribution transfers 5-15% (Swolfs et al., 2014) of the stress from the failed fiber to the neighboring fibers within the stress concentration radial failure zone. In parallel, the matrix surrounding the failed fiber experiences a shear load that transfers stresses back to the failed fiber. Then, the HE fiber surrounding the failed LE fiber will bridge the broken fiber, allowing the broken fragments to increase their failure strain capacity. The failed fiber will then contribute to the bundle total load-carrying capacity and increase the total failure strain.

2.10.4 Experimental Hybrid Composites Mechanical Performance

The experimental works studying the existence of the unexpected hybrid effect when combining LE and HE fiber mechanical properties were performed shortly after introducing the carbon fibers to the existing glass fibers. Section 2.9.2 showed that the first reported experimental work on hybrids was performed by (Hayashi, 1972). His pioneering work and results encouraged further experimental studies on hybrids; since then, many researchers have studied the experimental performance of hybrid composites under different loading conditions. Loading conditions such as tensile, flexural, compressive, impact and fatigue have been thoroughly studied and reviewed. The progressive improvement of composite manufacturing and testing procedures is shown by comparing the new publications to the old publications between the 1970s and the 1990s. The carbon fiber mechanical properties have also improved recently compared to the carbon fibers manufactured 25 years ago (Swolfs et al., 2014). The new carbon fibers have more failure strain than the 1% failure strain (1.3% for T300 and 1.7% for T700) reported for the old carbon fibers and have less scatter in strength performance. The appearance of scatter strength has a huge influence on the hybrid effect. The absence of scatter strength of LE fibers leads to zero hybrid effect; as the scatter strength increases, the hybrid effect will also increase (Swolfs et al., 2014). Moreover, the introduction of experimental tests standards in the 1990s unified the test protocols and added more credibility to the experimental outcomes.

The next sections will discuss the tensile, compressive and flexural experiments to date and how they are related to the subject of this study on the experimental mechanical buckling performance of composites.

2.10.4.1 Tensile, Compressive and Flexural Hybrid Effect

(Hayashi, 1972) first studied hybrid composites by testing the tensile performance of UD hybrid UD carbon/glass (with a ratio of 1:4). The resulting tensile failure strain was 45% larger than the reference failure strain from all-carbon specimens. This improvement in the failure strain from the LE fibers was defined by Hayashi as the hybrid effect.

(Phillips, 1976) studied the tensile failure of hybrid composites and developed two theories to explain the failure mechanism of hybrids with carbon and glass fibers. The first failure theory suggested that one of the weakest carbon tows will fail at its normal failure strain. Despite being broken, the discontinued carbon tow will still remain in contact with the surrounding glass-reinforced matrix. The broken carbon tow will continue sharing the load and contributing to the total stiffness. The remaining unbroken carbon tows become stronger and resist more failure strain. The second theory proposed that the arresting effect of the glass fibers on the sudden crack propagation across the cracked section of the carbon fibers. In hybrids with a high glass to carbon ratio, catastrophic crack propagation failure is less likely.

(Manders & Bader, 1981) reviewed the effect of the hybrid ratio and the degree of fiber dispersion within the hybrid lamina. They studied the hybrid effect of inter-ply UD carbon layers sandwiched between UD glass layers. The enhanced failure strain of the carbon fibers was up to 35% in tensile-carbon strength fiber and up to 45% in the tensile modulus. This hybrid effect was observed at a very small core thickness; indeed, the layer debonding was also limited due to core thickness. Conversely, no hybrid effect was observed in the failure strain at a high core thickness. The high level of fiber dispersion and the low level of carbon fiber helped to increase the hybrid effect percentage.

(Kretsis, 1987) reviewed the work of several researchers on the tensile performance of UD and multidirectional MD hybrids in tension. He concluded that the tensile modulus obeys the rule on

mixture unless there is an incorrect fiber volume fraction estimation. In contrast, the bilinear tensile strength behavior does not follow the rule of mixture. He defined the hybrid effect as the deviation domain continued by the rule of mixture as the upper bound and the failure criterion of maximum elongation as the lower bound. This hybrid effect can be quantified as a percentage increase from the reference failure strain. In addition to confirming the existence of the controversial hybrid effect, he also emphasized the definition of the hybrid effect and scientific experimental studies. For hybrid flexural performance, the bending test should be carefully monitored as the flexural strength and modulus are not sufficient alone to characterize the material properties. He reported that the reviewed studies used a specimen size ratio of 1:30 to suppress the effect of the inter-laminar shear stress, limiting the value of the experimentally obtained flexural modulus.

(Benard, Boukhili, & Gauvin, 1991) studied the tensile properties of a hybrid composite laminate made from a bidirectional intra-ply glass/carbon fabric in compression compared to a laminate made from carbon fibers. The study confirmed that by using a simple and linear mathematical model combined with CLPT, a prediction of the mechanical properties of the complex intra-ply configuration is achievable. The hybrid laminate failed due to the LE fiber ultimate strain.

(Davies & Hamada, 2001) studied the flexural hybrid effect for materials made from UD T700S carbon and silicon carbide fibers for six specimens. They found that the silicon carbide exhibited a higher compressive-to-tensile ratio than the carbon fibers as it provided more resistance on the compression side. Hence, the flexural strength increased by 22%. The concept of placing the glass fibers at the compressive side while placing the carbon fiber at the tension side is currently valid and has been supported by several studies (Dong & Davies, 2012); (Dong, Duong, & Davies, 2012). In their comprehensive review, (Swolfs et al., 2014) supported this concept and identified that under this concept, the failure mode changes from the usual failure at the tension side to a crushing failure at the compression side that is caused by the stress concentration resulting from the compression rollers.

(Dong et al., 2012) experimentally tested an intra-ply hybrid composite made from S-2 glass and TR30S carbon by adding glass fibers to the surface of the carbon fibers at different glass content ratios in three-point bending tests. A positive hybrid effect was obtained by substituting carbon layers with glass layers at the compression side. Laminates with glass layers placed at the

compression side, such as in their specimens G1C4 and G2C3, performed better than the specimens made from all-glass and all-carbon layers. These experimental results were reinforced by microscopic observations that showed a common failure at the compression side of the test specimens. An FEA was also used to simulate the experimental procedures, and its results agreed with the experimental results with respect to the flexural modulus and strength. Therefore, glass fibers resist compression better than carbon fibers on the compression side of the specimen, yielding the highest compression strength.

(Dong & Davies, 2012) tested nine hybrid specimens made from eight layers of UD S-2 glass and T700S carbon fibers in an intra-ply configuration in three-point bending tests. The specimens varied from all-carbon specimens to all-glass specimens by gradually replacing carbon layers with glass one layer at a time. They observed that to achieve a higher flexural strength, the glass fiber volume fraction should be greater than the carbon volume fraction. The overall maximum flexural strength was obtained in the hybrid specimen with a 0.125 ratio of glass to carbon plies and 50% volume fraction for both carbon and glass fiber contents. This hybrid specimen performed 43.46% and 85.57% better than the all-carbon and all-glass specimens, respectively

(You, Park, Kim, & Park, 2007) studied the benefit of the tensile hybrid effect for materials to be used in concrete structures. They tested six pultruded hybrid rods against two reference specimens made from all-glass and all-carbon. Three of the six hybrid rods were fabricated using a vinylester resin matrix, and the other three used unsaturated polyester. The hybrid rod configurations were divided into three different designs: the carbon fibers as the core, the carbon fiber at the surface, and dispersed intra-ply. The carbon and glass fiber volume fractions by weight were 23% and 37%, respectively, for all of the hybrid rods. Their hybrid effect was defined as the improvement in the ultimate strain compared to the reference all-carbon specimen. Therefore, the ultimate tensile strain hybrid effects for the three hybrid deigns were 26-27%, 9-13% and 14-33% for the three configurations.

(Pandya, Veerraju, & Naik, 2011) studied the hybrid effect of two hybrid specimens (H1 and H2) against two baseline specimens made from woven all-carbon and all-glass fabrics. Specimen H1 had a sacking sequence of carbon and glass layers of [G3C2]s, whereas H2 had the carbon layers at the outer side of the lamina: [C2G3]s. The carbon fabric was T300 8-harness satin, and the glass

fabric was plain woven E-glass. The tensile test was performed according to ASTM standard D3036-76 and showed a 90.4% increase in the H1 ultimate tensile strain compared to the all-carbon specimen and a 42% increase in strength compared to the rule of mixture (Figure 2-25). The compressive test was performed under the conditions of ASTM standard D3410 and provided a 10.6% increase in compressive strength for H1 compared to the results calculated from the rule of mixture (Figure 2-25).

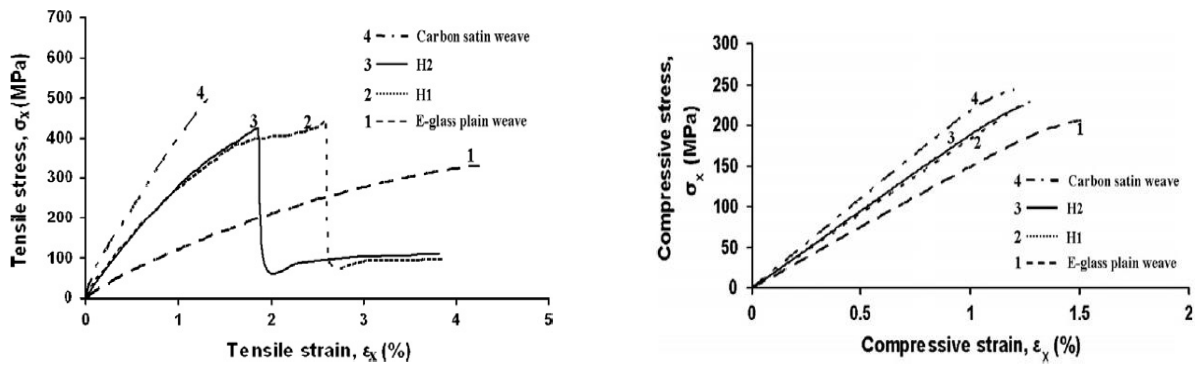

Figure 2-25: Pandya et al. hybrid effect of hybrid specimens under tensile and compressive loading (Pandya et al., 2011)

(J. Zhang, Chaisombat, He, & Wang, 2011) tested five laminate configurations made with different stacking sequences using plain woven E-glass and T300 2/2 twill carbon fabrics to examine the hybrid effect influence on the tensile, compressive and flexural properties. An upper limit was set by the all-carbon eight-layered lamina $[C]_8$, and a lower limit was set by the all-glass eight-layered lamina $[G]_8$. In between, three additional hybrid laminates were made to study the hybrid effect by arranging the glass and carbon layers in different stacking sequences: $[C_2G_2]$s, $[CG_3]$s and [CGCG]s. The experimental tests were conducted following ASTM standards for the tension and 3-point bending tests and the NASA short block test fixture for the compression tests. Next, an analytical solution for both tensile and compressive properties was derived from the linear rule of mixture, while a theoretical solution was obtained to calculate the bending strength. In the tension and flexural tests, the experimental results agreed with the analytical results, showing no

unpredicted hybrid effects (see Figure (2-26 (a), (b), (c), (d) (e)) The $[C_2G_2]$s lamina gave the same tensile resistance as the [CGCG]s lamina and showed a positive hybrid effect in the flexural tests. On the other hand, the compression results showed strong evidence of experimental differentiation from the analytical results due to the hybrid effect. The two samples with the same ratio of glass-to-carbon layers (50:50) showed a slight difference in their resistance. The [CGCG]s laminia resisted more than the $[C_2G_2]$s lamina and strained more than all the other samples (see Figures 2-18 & 2-19). This improvement in compression resistance may be due to a bridging effect. The hybrid effect in compression is considered to be negative as the $[C_2G_2]$s resistance is less than that of [CGCG]s. (Yeter, Erkliğ, & Bulut, 2014) studied the hybrid effect on the experimental buckling behavior of hybrid plates made from a combination of UD carbon, glass and aramid fibers with different symmetrical and asymmetrical ply orientations. They also numerically studied the effect of different shapes of delamination "cutouts" in addition to the test specimens' length-to-width ratio (L/d) on buckling performance. They concluded that the asymmetrical [0/90]6 plate with carbon plies at the outer side delivered the highest buckling load. In contrast, the smallest buckling load was shown by the asymmetrical [0/90]s with glass plies placed at the outer side. In addition to the effect of the length-to-thickness ratio of the specimens, their numerical study investigated the effect of different delamination shapes (circle, triangle, rectangle and ellipse). They found that the buckling load increases with increasing (L/d). Moreover, their numerical parametric study showed that specimens with an elliptical cutout buckled less than other cutout shapes, while the square cutout delivered the highest buckling resistance.

(Jin Zhang, Supernak, Mueller-Alander, & Wang, 2013) investigated the flexural 3-point bending and flatwise compression performance of trapezoidal corrugated sandwich panels with and without foam filling and with hybrid (glass: carbon = 50:50) face sheets compared to two reference all-glass and all-carbon face sheets. Under bending load, the hybrid panels performed slightly better than the all-glass and all-carbon panels due to the alternating sequence of glass-carbon lay-up within the upper face sheet affected by the compressive loading. In addition, placing the carbon layers at the outer side of the face sheet and increasing the corrugation angle maximized the flexural strength. The flatwise test was executed by applying a low-speed quasi-static compression load. Despite having medium energy absorption between the all-glass and all-carbon specimens, the

hybrid panels filled with foam delivered the best crush force efficiency. Indeed, this might be considered as a “hybrid effect” where the glass fibers arrest the sudden failure of the carbon fibers.

(Irina, Azmi, Tan, Lee, & Khalil, 2015) reviewed the tensile and flexural performance of hybrid laminates made from woven plain carbon fabric, woven plain E-glass fabric and stitched bi-axial (±45) E-glass fabric against three reference specimens made from each fabric alone. Their test specimens had different carbon-to-glass fiber content ratios in the forms of $[CG_2]_6$, $[G_{stitched}C]_6$ and $[C(G_{stitched})_2C]$. The best tensile and flexural performance was delivered by the hybrid specimen $[CG_2]_6$ compared to the other hybrid specimens. However, the obtained experimental results from the tested specimens could not be related to each other as they differed in fiber content ratios and types. In fact, comparing the hybrid specimens with the plain woven E-glass to the specimens with stitched E-glass is improper. Regardless of this improper comparison, their study supports the existence of the hybrid effect when mixing two or more composite fibers in one lamina.

(Hai, Mutsuyoshi, Asamoto, & Matsui, 2010) studied the hybrid effect of constructing an FRP I-beam with hybrid carbon-glass flanges and GFRP webs. The manufactured beams had two flange-to-web (bf/bw) width ratios that they categorized as (i) small flange or (ii) large flange. For each type of the constructed I-beams, three specimens with different carbon fibers volume content ratios were made (52%, 33% and 14%). The recorded data of the out-of-plane deflections were captured using linear voltage displacement transducers and laser transducers. In addition, they recorded the beams’ strain distribution using strain gauges. The experimental results showed that the small flanged beams exhibited a liner, stable, and brittle delamination failure at the compressed interfacial layer of the top flange compared to the unstable, non-linear behavior of the large flanged beams. Additionally, they noticed that in flanges with a high carbon volume content ratio, the specimens tended to fail earlier. Hence, they suggested that a higher carbon fiber content ratio within the specimens’ flanges resulted in higher chances of delamination failure. However, the carbon fiber layers tend to fail earlier due to their low strain rates and stress concentration at the loading points, which causes fiber crushing failure. Their non-linear 3D FEA model results had a good level of agreement with the experimental and theoretical results. However, they did not present the experimental in-plane and out-of-plane non-linear post-buckling regions when comparing the experimental results to the numerical results.

(Zhao, Zhang, & Wu, 2012) manufactured four hybrid sandwich panels and two baseline all-carbon and all-glass face sheet panels using VARTM. Later, they tested their panels against a low velocity impact test and Compression After Impact (CAI) test setup. They observed that the hybrid specimens absorbed the impact energy better than the all-carbon specimen but poorer than the all-glass specimen. The catastrophic failure of the carbon fibers was witnessed microscopically in the modes of matrix and core cracking and fiber breaking and debonding. On the other hand, the all-glass and hybrid specimens suffered from matrix and core cracking, de-bonding and some fiber breakage. As a result, the specimen performance compared to the CAI test was affected by the impact failure, which caused the all-carbon specimen to fail earlier than the other specimens. However, the hybrid specimens with two carbon layers at the outer side of the face sheet lamina performed better than the other hybrids, which might be considered a hybrid effect.

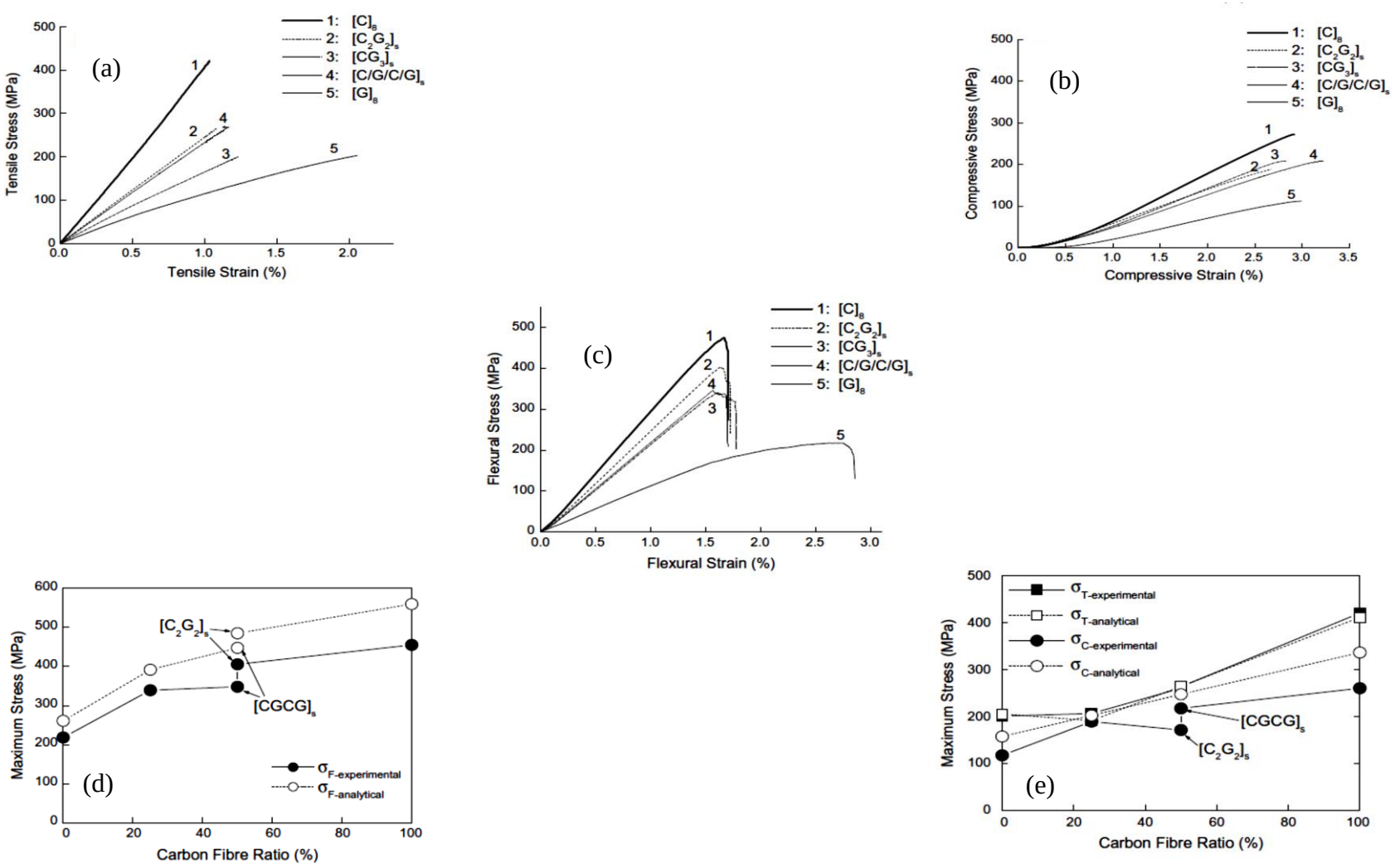

Figure 2-26: Zhang et al. (a) tensile stress-strain curve. (b) compressive stress-strain curve. (c) flexural stress-strain curve (d) experimental vs. analytical flexural results. (e) experimental vs. analytical tensile and compressive results

CHAPTER 3 EXPERIMENTAL PROCEDURE

3.1 Manufacturing

Foam cores used for VARTM manufactured sandwiches are usually perforated or grooved to enhance the resin flow and avoid dry spots. However, this technique has the disadvantage of increasing the weight. (Halimi, Golzar, Asadi, & Beheshty, 2013) fabricated six different sandwich panels with rigid PVC foam cores using the VARTM technique with a DM at the upper side of the mold only. Each panel had a different pattern of perforated holes drilled through the core's thickness that were used to assist the resin flow during the VARTM process. The sandwich wetting process started by wetting the upper face sheet first; then, the resin passed through the holes to the lower face sheet that distributed the resin in a radial direction. However, specimen number 6, as illustrated in Figure 3-1, produced unacceptable dry spots due to the small diameter of the holes and the long distances between each hole. Thus, it can be concluded that the resin flow at the lower face sheets is affected by the hole dimensions and patterns. As a result, the wetting time was improved by 40%, and the panel weight was slightly increased by 3.6%.

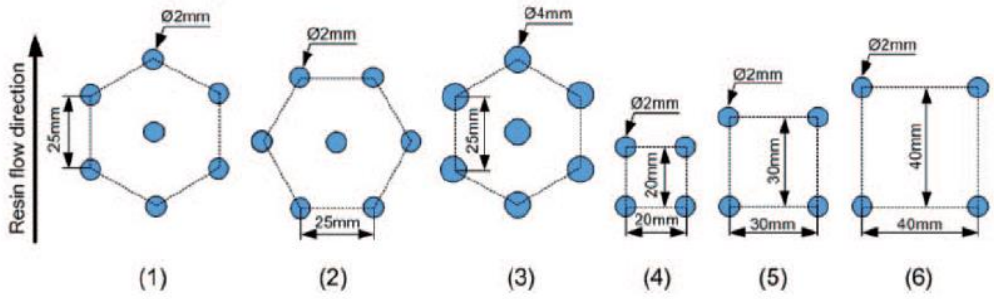

Figure 3-1: Grooved foam core patterns

Under flexural 3-point bending tests, the panels were cut into two aspect ratios (10 and 20). It has been observed that specimens with an aspect ratio of 10 failed due to shear stress, while the specimens with an aspect ratio of 20 failed under tensile stress. The debonding fracture test on the specimens with planted Teflon strips showed an improvement compared to the reference (with

solid PVC core) specimen critical load and fracture toughness, particularly the specimen with pattern number 3 shown in Figure 3-1. The benefit of using solid foam cores instead of the precut cores is to ensure a completely homogeneous specimen after cutting the test specimens. In reality, the industry uses foam cores with bleeder holes or superficial knife-cut grooves to ensure complete resin infusion through both faces (see Figure 3-2). These precut foam cores might endanger the homogeneity of the test specimens with resin rich spots, which might also affect the specimens' performance. Hence, the test specimens might have an unequal number of resin rich spots from one specimen to another that certainly affect the panel behavior. These premade cuts and grooves help resins with low permeability to flow easily and completely wet both face sheets simultaneously. However, using precut foam cores is not desirable in this study as they are intended to eliminate the effect on buckling behavior. Furthermore, a number of tests were made in our lab by other students to infuse the resin completely through the upper face via the bleeder holes for the lower face, but this did not produce panels with acceptable quality (see Figure 3-3). A solution to this quality problem is to use a solid plain core and to infuse both face sheets simultaneously by placing the infusion mesh and peel plies at both face sheets (see Figure 3-4).

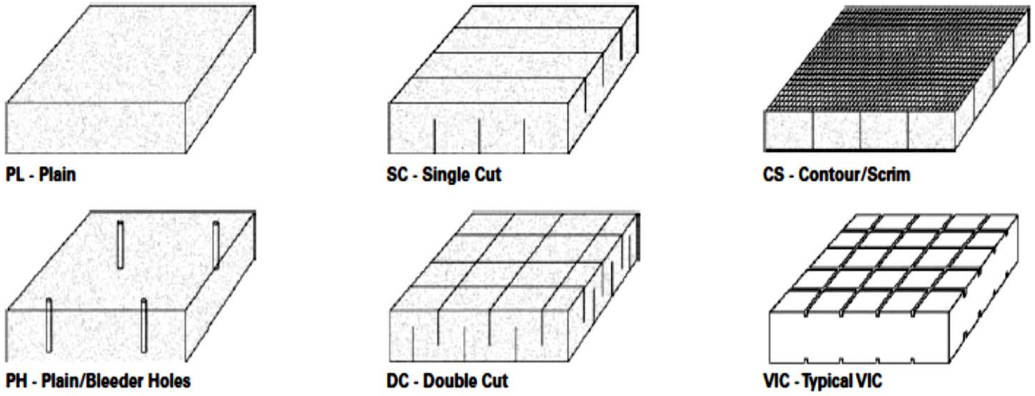

Figure 3-2: Types of commercial foam cores ("Gurit, GUIDE TO COMPOSITES,")

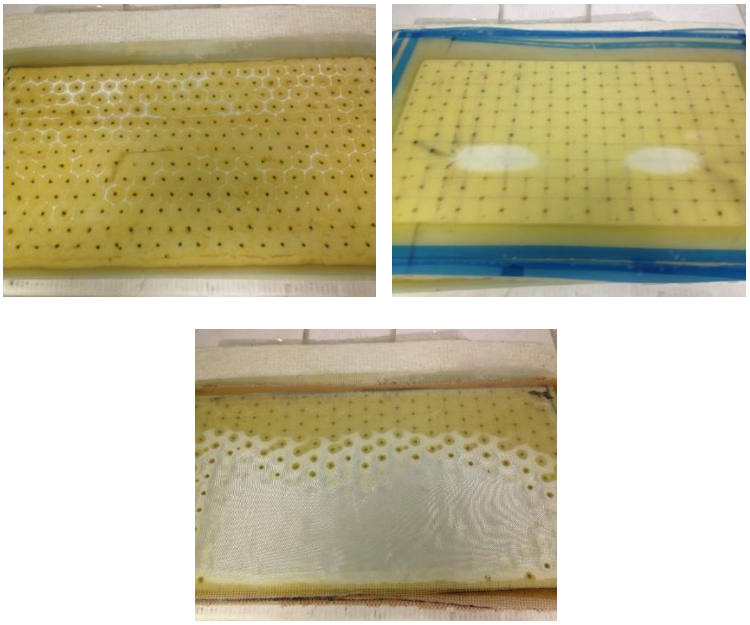

Figure 3-3: Dry spots and resin rich areas in the VARTM samples

The VARTM process produces specimens with better core to face bonding compared to the favorable alternative of vacuum after hand lay-up (Gaiotti & Rizzo, 2012). (Zhao et al., 2012) numerically modeled the resin flow of the VARTM process used in manufacturing composite sandwich panels with rigid polymethylacrylic imide (PMI) foam cores that have unidirectional grooves and channels. They found that the wetting time needed to impregnate the panels' face sheets can be controlled by the existence of a distribution medium (DM) and its ratio to the perform, the resin inlet pattern and location. They divided the resin inlet sources into linear and point sources located at the perform center and the short and long edges. The fastest wetting time was achieved when the DM covered the whole perform (DM/Perform = 1). Moreover, a shorter wetting time can be achieved by implementing a central liner resin inlet source parallel to the perform's short edges. Therefore, the VARTM process with double face sheet infusion ensures complete face sheet wetting on both sides of the sandwich panels with minimal defects such as dry and resin rich spots.

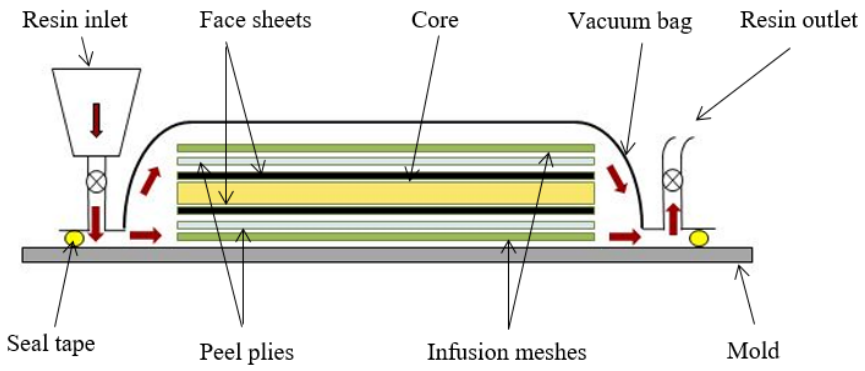

Figure 3-4: VARTM mold

3.1.1 Manufacturing Process

The eight sandwich panels were programmed to be manufactured locally inside one of the lab facilities at the department of Mechanical Engineering at Polytechnique de Montreal. A wooden table with a glass surface was used as the hard mold side for the VARTM infusion process. The glass surface produces parts with a smooth and glossy surface. Before starting the material lay-up, the glass surface was cleaned from dust and wiped with acetone to remove any residues from previous usage. Next, a double face synthetic rubber sealant tape model AT-200Y supplied by Airtech International Inc. was placed along the glass surface edges. Then, a layer of release agent was spread on the glass surface and allowed to dry for 10 minutes. After the release agent had dried, the materials were cut and laid-up from in the following order: infusion mesh - peel ply - fiber plies – core - fiber plies - peel ply - infusion mesh. A spiral polyethylene tube was cut into two tubes, and each tube was placed along each short edge. The spiral tubes allowed the infused resin to enter the mold from one of the short edges and to exit the mold from the other edge. A solid polyethylene tube was cut into two tubes, and each was connected to the spiral tubes as the outer side of the entry and exit tubes outside the bagged area. The vacuum reservoir is needed to protect the vacuum pump from damage when the vacuumed excess resin exits the mold and collects inside the vacuum reservoir unit. The resin exit tube was then connected to the vacuum reservoir,

which was also connected to a central vacuum line. Figure 3-4 shows the final mold preparation before applying the air leakage tests and epoxy resin infusion. Vacuum trials were performed twice each and lasted for 20 minutes: to test the mold against leakage, the resin entry tube was clamped, and the vacuum line was disconnected from the vacuum reservoir unit. Any drop in internal pressure indicates the presence of improper sealing that leads to air leakage. The stability of the internal pressure was monitored at the vacuum reservoir pressure gauge. The applied pressure was approximately 30 in Hg. After the success of the vacuum tests, the resin was mixed with the hardener at a ratio of 4:1, as recommended by the resin manufacturer. The resin mixture was then infused through the entry tube and flowed over the panel's upper and lower face sheets completely before reaching its gel time of 70 minutes. As soon as the excess resin started to exit the vacuumed panels, both the entry and exit tubes were clamped tightly to maintain a steady mold internal pressure and to avoid any leakage. Finally, the panels were kept at room temperature for 24 hours for complete curing before demolding. Figure 3-5 and Table 3-1 show the materials used in the panel fabrication.

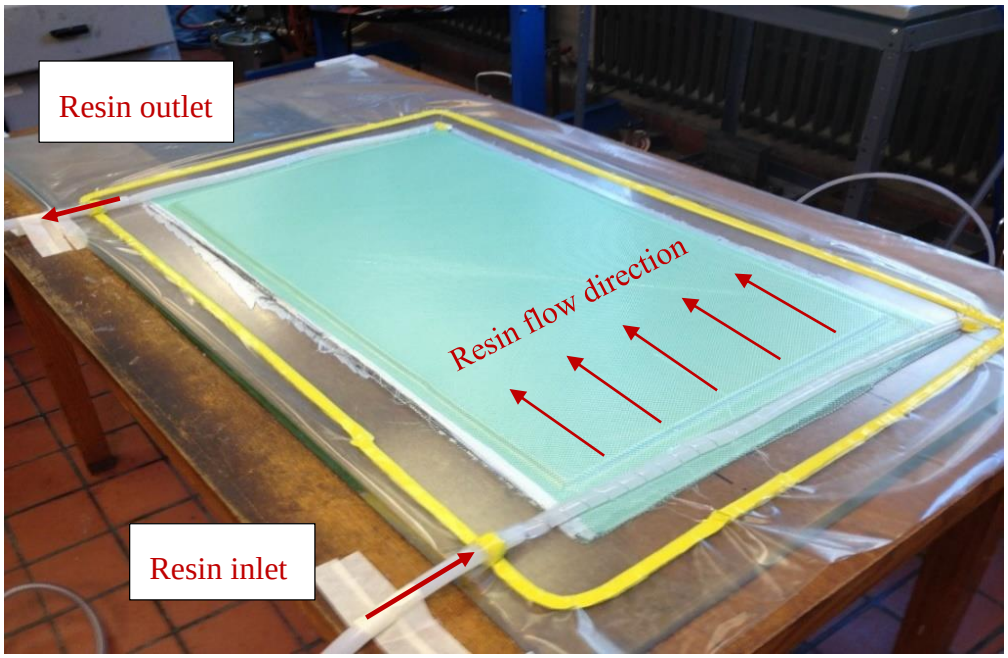

Figure 3-5: Sandwich panel before resin infusion

Figure 3-6: 7781 8H glass and 94101 plain 3k T-300 carbon Fibres fabrics and SAN core

Table 3-1: The materials used in manufacturing the sandwich panels

Material	Remark
Carbon fibre	Plain 3k T-300 wave carbon fiber style (94101) supplied by Freeman manufacturing and supply company.
Glass fibre	Woven 8HS glass fiber style (7781) supplied by Hexel®.
Core	Styrene Acrylonitrile (SAN foam) core model Corecell™ foam A300 supplied by Gurit
Resin	Epoxy resin supplied by Renshape® solutions model (RenInfusion™ 8601/Ren® 8602)

3.1.2 Face Sheet Fibre Volume Fraction V_f

The theoretical calculation of the laminate's strength and modulus depends on knowing or assuming the value of either the fiber volume (V_f) or weight (w_f) fractions (Mallick, 2007).

Experimentally, the ratio of the net fiber content to the matrix content after subtracting the void content is determined by the manufacturing process and quality.

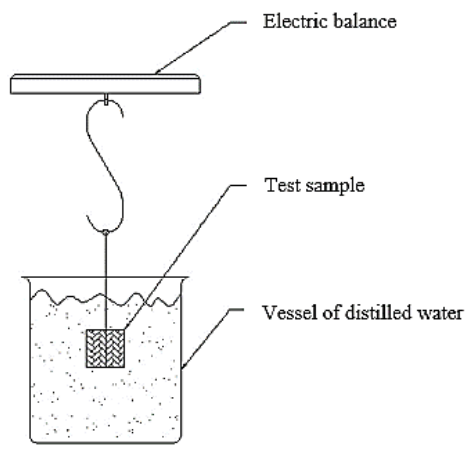

Figure 3-7: ASTM D792-00 standard test methods for density and specific gravity (Relative Density) of plastics by displacement

The volume fraction V_f for all of the face sheets were measured and calculated according to the standard procedure of ASTM D792-00, as illustrated in Figure 3-7. The calculated V_f for the all-glass and all-carbon laminates were 47% and 54%, while the hybrid laminates H1-H6 provided an approximate overall value of 53%. Therefore, the highest volume fraction was calculated for the all-carbon T300 plain wave laminates, followed by the hybrids and then the 8-HS all-glass. It was also noted that the addition of the carbon layers at the ratio of 2:2 increased the volume fraction of the all-glass laminate by 6%. This improvement could be due to the density variance between the two types of fibers that resulted in better resin impregnating during the infusion process.

3.2 Test Specimen Design and Face Sheets Arrangements

The buckling failures of composite sandwich panels are mostly governed by the mechanical properties of the face sheets and the core material together with the panel dimensions. Each of these three independent parameters contains a number of dependent variables that can influence the

sandwich panel buckling performance and their failure modes, as illustrated in Figure 2-14 in Section 2.8.1. For instance, the core-dependent variables, such as the density and stiffness, substantially control the sandwich panel performance due to the large difference in density and stiffness between the core material and the composite face sheets. The difference between the main sandwich panel components leads to early failure by buckling or surface wrinkling. Therefore, it is quite common for sandwich panels to fail due to the core's shear deformation before the failure of the face sheets (Carlsson & Kardomateas, 2011). In a similar manner, the face sheet-dependent variables, such as thickness, fiber type and orientation, matrix mechanical properties, and flexural rigidity, significantly contribute to the sandwich panel performance in several loading conditions. For example, a high stiffness unidirectional carbon fiber face sheet provides better bending and out-of-plane deflection resistance compared to an equal thickness unidirectional glass fiber face sheet. This advantage of face sheets made from carbon fibers over glass fibers is referred to as the inherent high stiffness characteristic of carbon fibers. Finally, the sandwich panel dimension-dependent parameters of length, width, core thickness and face sheet thickness contribute to the sandwich panel performance along with the other dependent variables. In particular, the greater the increase in the core or face sheet thickness is, the more rigidity is achieved. Moreover, the more the sandwich panel dimensional slenderness increases, the less core shear deformation is obtained, and the more face sheet resistance increases (Fleck & Sridhar, 2002). Therefore, to concentrate more on the performance of the face sheets, it is necessary to mitigate the parameters and variables that are not related to the face sheet response to buckling during the experimental tests. Correspondingly, the same core material and thickness must be used for all sandwich panels. In addition, the test samples should have the proper dimensional aspect ratio (slenderness) to suppress the failure caused by the core's shear deformation during buckling tests and to allow the face sheets to demonstrate their part in resisting the buckling load. Thus, the changing variables are only the face sheet fiber type and the assortment of different lay-ups of glass and carbon fiber layers within the face sheet, which affects its physical properties and flexural rigidity.

As previously discussed (Kretsis, 1987), the physical performance of hybrid unidirectional glass/carbon laminate with a high glass-to-carbon fiber ratio has a negative and positive hybrid effect in compression and bending tests, respectively. Therefore, the desired hybrid effect can be achieved when the number of glass fiber layers within the face sheet lamina is equal to or greater

than the number of carbon fiber layers. This observation offers a wide range of different ratios of stacking sequences of glass and carbon fiber layers that require extensive manufacturing and testing efforts to cover all of the options. The two hybrid glass/carbon fabrics tested by (Pandya et al., 2011), $[G_3C_2]_s$ and $[C_3G_2]_s$, failed at approximately the same ultimate compressive strength and ultimate strain rates. Furthermore, by placing the glass fiber at the tension side and the carbon fibers at the compression side within the lamina, an improvement in flexural performance was observed (Swolfs et al., 2014). The symmetric lay-up does not deliver the optimal flexural resistance. The conclusion drawn from (J. Zhang et al., 2011) for the occurrence of both negative and positive hybrid effects for compressive and flexural performance with the 2:2 carbon/glass ratio was quite interesting. Buckling failure start as a pure compression state; at a certain loading point (P_{cr}), the test specimen bends, and the specimen's flexural rigidity and bending resistance become more effective. Therefore, in light of J. Zhang's conclusion and to focus more on obtaining an apparent hybrid effect, the face sheets in this study have a 2:2 glass/carbon ratio with 2 layers of glass and carbon fibers with the matrix. The ratio of 2:2 carbon-to-glass fibers provides a total of six different stacking sequences of carbon and glass layers that can be used to manufacture six sandwich panels with hybrid face sheets laminates. The face sheet flexural rigidity (EI_f) plays a huge rule in buckling resistance and the face sheets' tendency to deflect toward the out-of-plane direction. Therefore, the sandwich panels were labeled and numbered according to increasing values of EI_f from H1 to H6. Additionally, two baseline sandwich panels were made of all-carbon face sheets (S8) and all-glass face sheets (S1) to represent the upper and lower limits of the buckling test parameters, respectively. Figure 3-8 shows all possible glass-to-carbon stacking sequences for a hybrid face sheet made from 4 layers of fibers using the 2:2 stacking ratio.

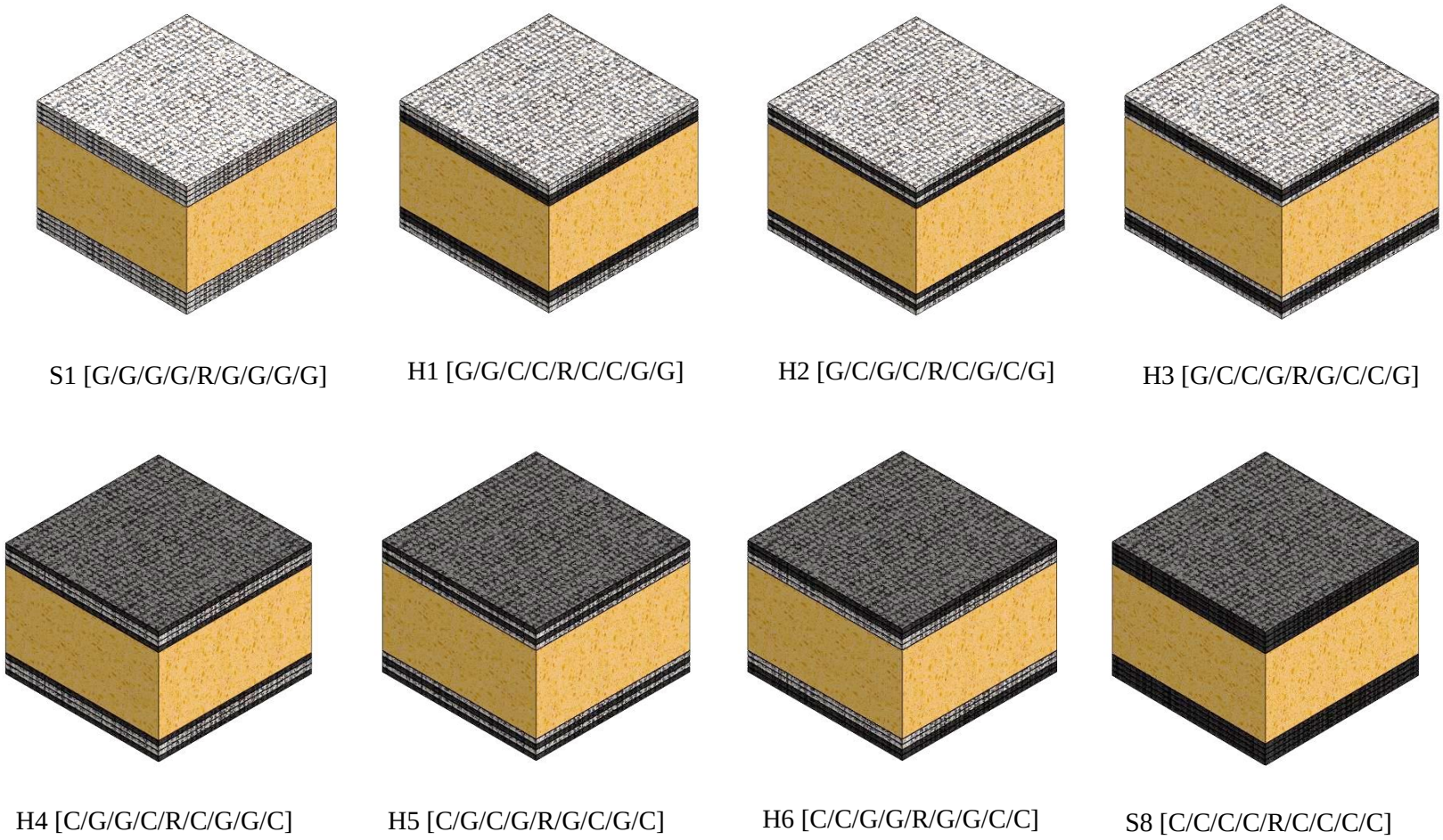

Figure 3-8: Sandwich panel configurations

3.3 Experimental Critical Buckling Load (P_{cr})

The experimental test setup must exhibit an out-of-plane deflection by allowing the sandwich panel to globally buckle toward a direction perpendicular to the sandwich panel's surface. This out-of-plane deflection is achievable with uniaxial compression loading while supporting the panel's top and bottom vertical edges either with simply supported or fixed boundary conditions. The support-free vertical edges allow out-of-plane deflection to occur. Several experimental studies have revealed that buckling is more indicative from the data extracted from the out-of-plane readings than those from in-plane deformation. Thus, to measure the out-of-plane deflection at any point on the deflected surface, it is recommended to use deflectometers or non-contact laser displacement sensors (Carlsson & Kardomateas, 2011). The deflectometer is limited to only measuring one side of the sandwich panel that deflects in the direction against the deflectometer spring-loaded measuring ball-tip. In contrast, non-contact laser sensors will measure the deflection at any point on both sides of the sandwich panel when they are set back-to-back. The recorded readings represent the change in the reflected laser beam, which measures the distance change between the laser sensors and the deflected face sheets. For example, by placing them in a back-to-back position at the center of both face sheets, the readings will represent the positive deflection and the negative deflection. Hence, the non-contact laser sensors serve the purpose of this study well by measuring the deflection of both sides of the sandwich panel. A comparison between the widely used methods of recording experimental values of P_{cr} is summarized in Table 3-2.

Table 3-2: Comparison of the instrumentations used in experimental tests

	P_{cr}	**In-plane displacement**	**Out-of plane deflection**	**Back-to-Back**	**Accuracy**
Strain Gauge	yes	yes	no	yes	High
Deflectometer	yes	no	yes	no	Modrate
Non-contact laser sensor	yes	no	yes	yes	High

3.4 Buckling Test Specimens Dimensions

The main objectives of this study are to examine the buckling behavior of sandwich panels and to measure the out-of-plane deflection of the hybrid face sheets in order to determine the hybrid effect on both observations. The sandwich panels are higher in rigidity compared to composite laminates due to the sandwich panels' greater thickness and their tendency to bend toward the out-of-plane direction. In addition, the premature shear deformation failure of the core should be minimized to let the face sheets exhibit their buckling and out-of-plane resistance characteristics. Therefore, a proper length-to-width aspect ratio must be selected to ensure a successful experimental test.

Preliminary standard compression tests were performed on sandwich panels made from glass and carbon fiber face sheets only with different aspect ratios to select the best aspect ratio for the study objectives. The first compression test was performed according to ASTM D7137/D7137M with an aspect ratio of L/b = 1.5. Both specimens failed under compression due to core's shear deformation at approximately the same loading level but different in-plane displacements and compression moduli, as shown in Figure 3-9.

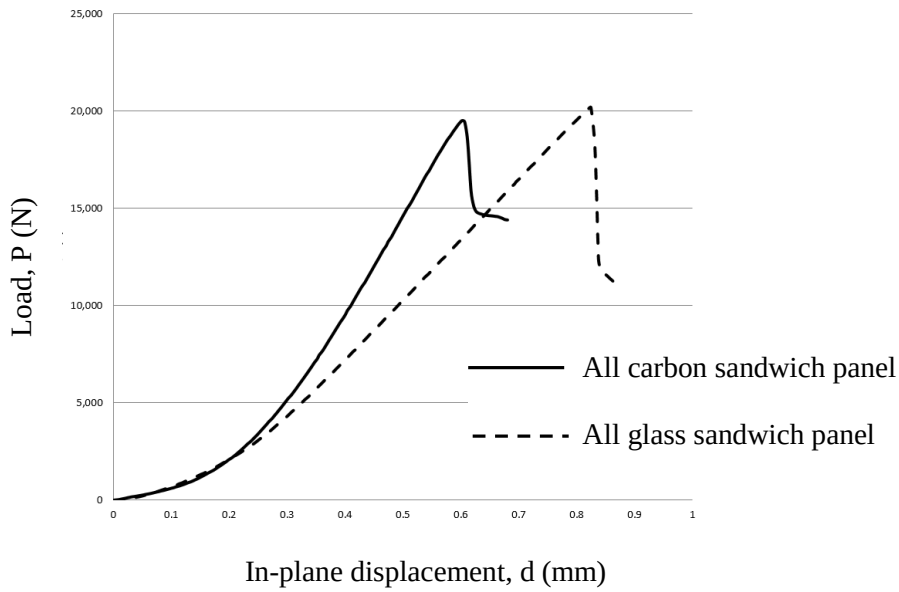

Figure 3-9: Load vs. in-plane displacement for sandwich panels made from all-carbon and all-glass face sheets

Next, tests were conducted according to ASTM C364/C364M-07 for sandwich panels with only all-carbon fibers face sheet to determine whether buckling occurred in the highly stiffened face sheets; if buckling occurred in the high stiffness all-carbon face sheets, it will obviously happen in lower stiffness face sheets such as glass fibers and hybrids. Thus, specimens with aspect ratios of L/b = 3 and 4 were tested under a uniaxial compression load, and the out-of-plane deflection was measured by back-to-back reflex non-contact laser sensors to capture both the negative and positive deflections. The specimen with L/b = 3 failed under compression at 6 kN with no significant out-of-plane deflection. The specimen with L/b = 4 provided a modest buckling behavior and out-of-plane deflection (see Figure 3-10 and 3-11). This modesty is due to the occurrence of P_{cr} at a small in-plane displacement (d < 0.5 mm). From previous results, it is clear that the all-carbon face sheet sandwich panel started to exhibit buckling behavior at an aspect ratio of L/b = 4, as shown in Figures 3-10 and 3-11.

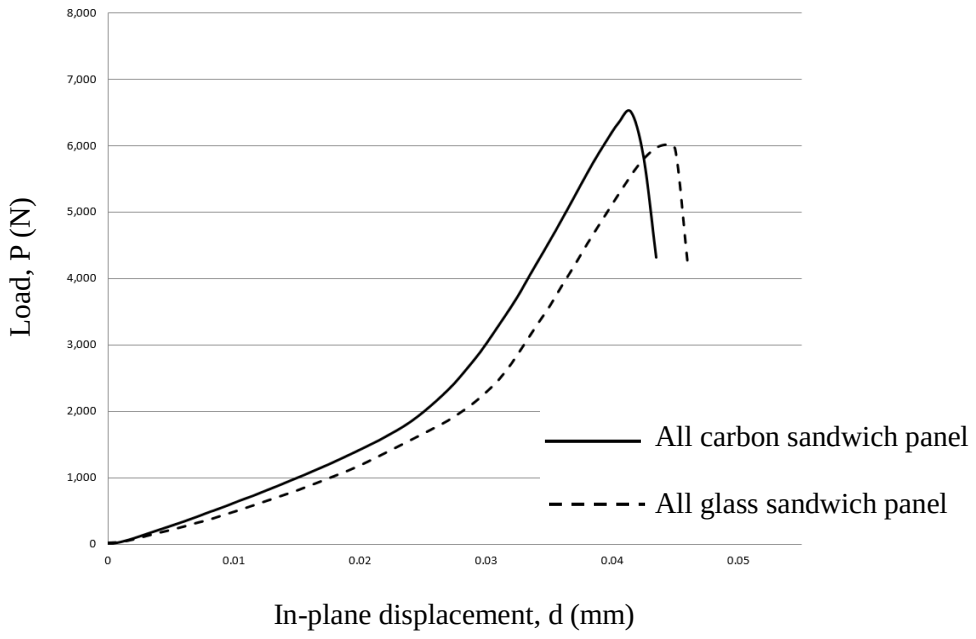

Figure 3-10: Load vs. in-plane displacement for the samples with L/b = 4 and 3

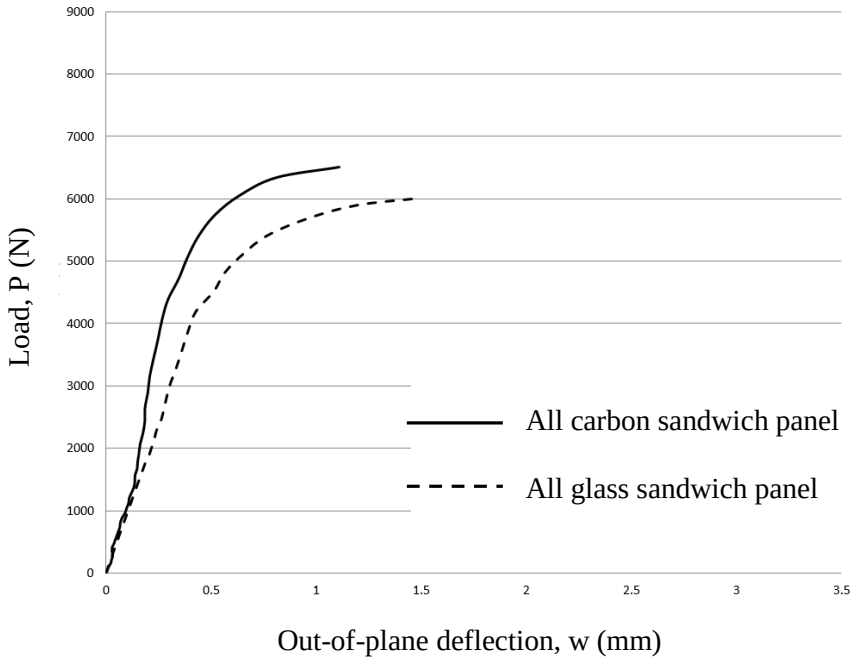

Figure 3-11: Load vs. out-of--plane deflection for the samples with L/b = 4 and 3

Despite being designed to test the properties of the sandwich panels, ASTM D7249/D7249M-6 can be beneficial for designing the size of the buckling test specimens. The similarities between the two tests in recording the face sheet deflection performance when the specimens under buckling reach their critical buckling load and start to bend is analogous to the bending test designed for this standard. Therefore, the specimen size in this study was guided by the aspect ratio of L/b ≈ 8 for specimens designed according to ASTM D7249/D7249M-6, heightening the effect of the face sheet contribution against buckling. Under these circumstances, the test specimens have an aspect ratio of L/b = 8. Accordingly, preliminary experimental tests were performed with specimens 406 cm (16 in) long and 51 cm (2 in) wide. These specimens were cut by a water-cooled diamond table saw from three sandwich panels made from all-glass, hybrid and all-carbon face sheets. As mentioned in Section 3.2, each hybrid face sheet contained 2 layers of carbon fibers and 2 layers of glass fibers. The layers were laid-up in an alternating sequence starting with a glass fiber layer: [GCGC]. All three sandwiches were tested under a uniaxial loading condition and constrained according to ASTM C364/C364M-07. The out-of-plane deflection was captured at the center of both face sheets (back-to-back) by the non-contact laser sensors. As a result, all specimens including the highly stiffened all-carbon specimen demonstrated buckling failure rather than compression or crushing failures. The effect of the core shear deformation failure was minimized, allowing the face sheets to contribute to resisting buckling. All specimens provided a recordable and clear out-of-plane deflection with a good deflection allowance between P_{cr} and the failure load (see Figures 3-12 and 3-13).

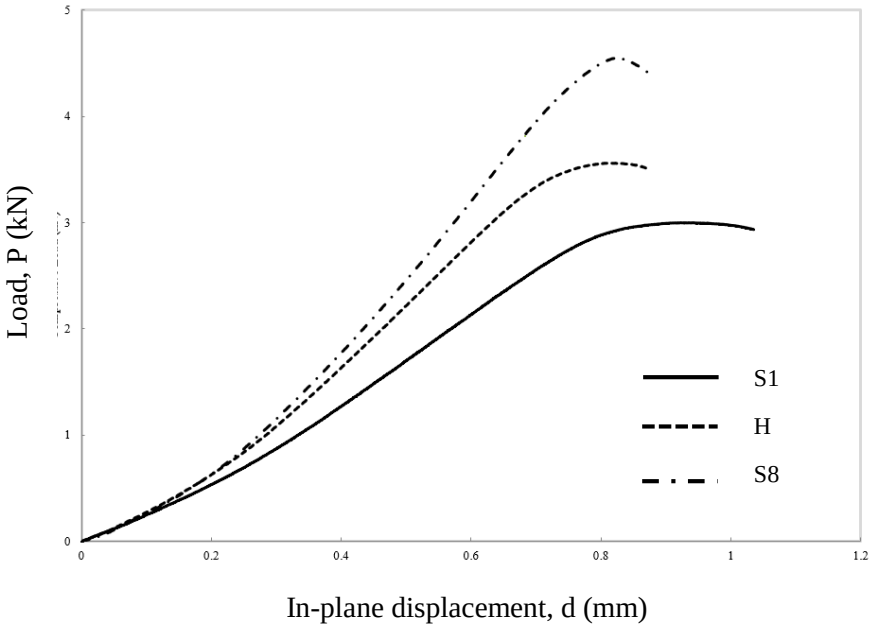

Figure 3-12: Compressive load vs. in-plane displacement

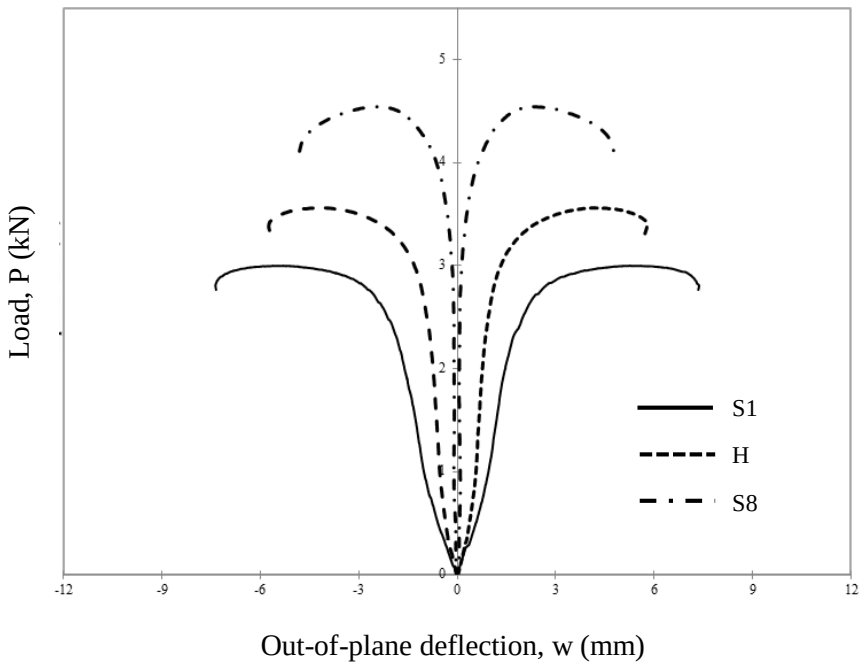

Figure 3-13: Compressive load vs. out-of-plane deflection

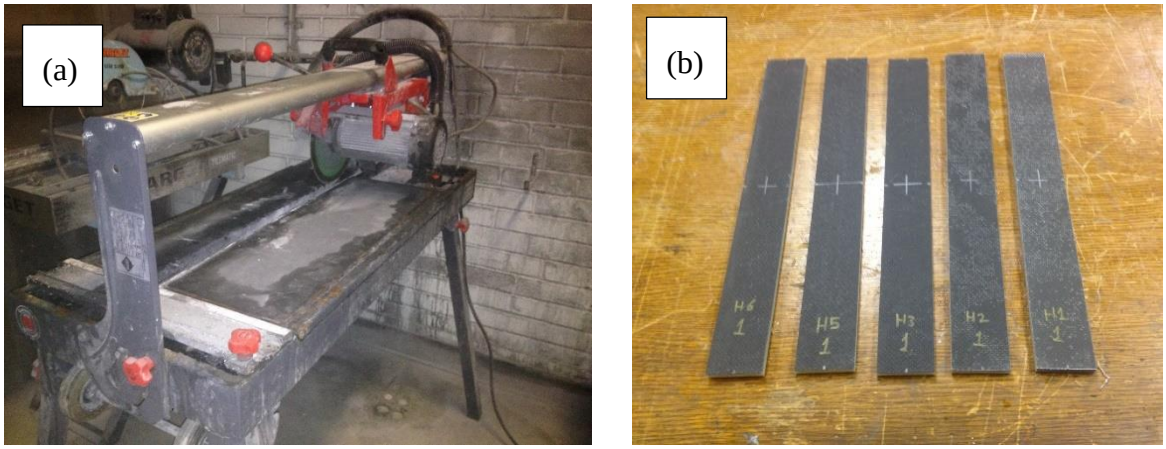

Figure 3-14: (a) diamond cutting table saw. (b) buckling test specimens

As expected, the hybrid sandwich panel improved the buckling resistance compared to the all-glass sandwich due to the 21.7% increase in the face sheet stiffness. Despite the hybrid specimen buckling earlier than the all-carbon specimen, the hybrid specimen improved the natural catastrophic brittle failure of carbon to a less brittle (and more similar to glass fiber) failure. This improvement is very important in structures that implement a Structural Health Monitoring (SHM) system. Therefore, from the above preliminary experimental test results, the aspect ratio of L/b =8 delivered clear buckling behavior accompanied by an obvious out-of-plane deflection that can be used for other hybrid specimens in this investigation. Thus, eight sandwich panels were made and cut by a diamond table saw into five specimens for each panel, as shown in Figures 3-14 (a) and (b).

3.5 Flexural 3-Point Bending Test

The symmetrical arrangement of the glass and carbon layers within both face sheets along the neutral axis of the sandwich panels under bending creates a distinct flexural rigidity for each face sheet. This unequal situation of face sheet flexural rigidity within the same sandwich panel under flexural loading certainly contributes to the existence of a hybrid effect. As mentioned earlier, the hybrid effect was shown for samples with different stacking sequences of carbon and glass fiber layers within composite laminates. Therefore, as a part of the complex behavior of buckling, a

simple 3-point bending test was performed according to ASTM C393/C393M-11 for all hybrid sandwich panels involved in this study.

3.5.1 3-Point Bending Test Set-up

The experimental test was performed on an MTS-810 universal testing system according to ASTM C393/C393M-11 for at least three specimens per sandwich panel type. The test machine was hydraulically operated with a capacity of 100 kN. The test fixture was mounted between the machine's stationary lower head and the upper moving head, as shown in Figure 3-15. The machine's upper cross head was set to travel downward at a constant speed of 6 mm/min. The applied force and the downward traveled displacement were both recorded for all test specimens.

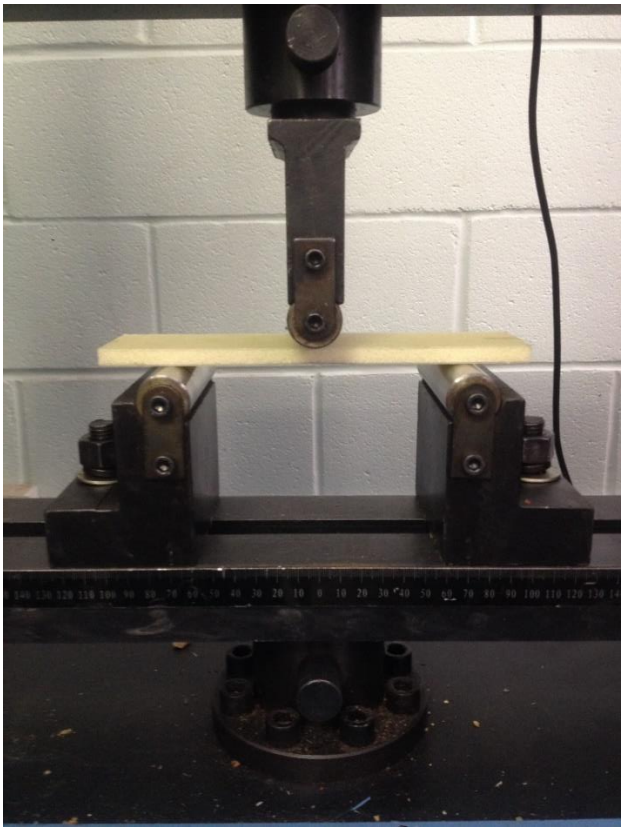

Figure 3-15: 3-point bending test set-up

3.5.2 Bending Test Results

The recorded experimental data showed an increased out-of-plane deflection proportional to the load applied at a constant speed by the test machine's traveling cross head until a certain load point (P_{ult}) where the specimen failed due to shear deformation. From Figure 3-16, it can be observed that at a certain load point, the curves tend to yield and form a transition zone between the yield load point P_{yld} and P_{ult}. This transition zone reflects the specimens beginning to yield against the additional applied load and the specimen's tendency to not carry more load. Therefore, it is very important to locate P_{yld} and P_{ult} and their deflection points w_{yld} and w_{ult} for all specimens. The yield load P_{yld} was extracted as the point where the linear part of the load vs. deflection curve starts to diverge from its tangent by forming the transition zone. This conservative method of data extraction is discussed in full detail in Section 3.7.1; the load vs. deflection curve behaves similarly to the load vs. out-of-plane deflection curve generated by the buckling experimental test. From the extracted values of both the ultimate and yield loads from the curves shown in Figure 3-17, a calculation was performed to obtain the yield and ultimate facing stress σ_{yld} and σ_{ult} together with the core shear stress τ_{cs} by employing the following equations:

$$\sigma = \frac{P\,S}{2t\,(d+c\,)b} \qquad \text{(3-1) (ASTM, 2011)}$$

$$\tau = \frac{P}{(d+c)b} \qquad \text{(3-2) (ASTM, 2011)}$$

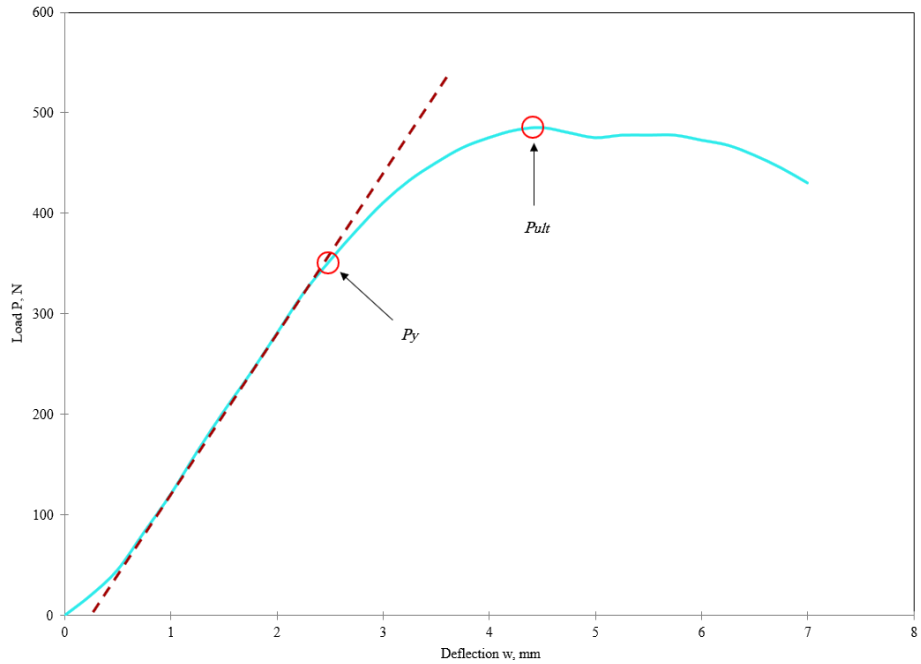

Figure 3-16: The extracted P_{yld} and P_{ult} from the load-deflection curve

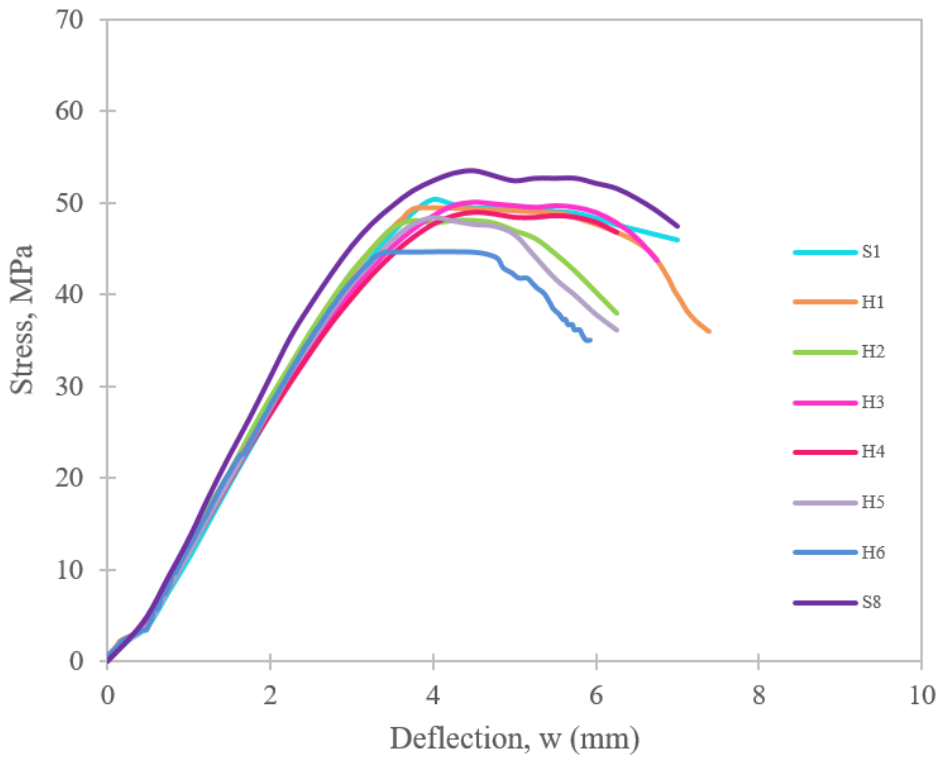

Figure 3-17: The experimental stress-deflection curves of the 3-point bending test

The extracted values of P_{yld}, P_{ult}, w_{yld} and w_{ult} along with the calculated values of σ_{yld}, σ_{ult} and τ_{cs} are presented in Table 3-3.

The standard 3-point test was intended to mainly examine the core shear properties. However, from the obtained results, it was observed that how the hybrid specimens performed against the applied load depended on their stacking sequence of carbon and glass layers within their face sheets. In general, all tested specimens eventually failed when the core's generated shear stress reached the core's maximum allowable shear strength of 0.6 MPa mentioned in the core's data sheet at P_{ult} (see Table 3-3). This maximum shear stresses were calculated from equation (3-2) by substituting the load P value with P_{ult}.

From Figure 3-19 (a), S1, H1 and H2 yielded at approximately the same load value of 360, 360 and 365 N, respectively which might be due to laying the glass fiber at the exterior side of the specimens. Hybrids H3 and H4 yielded at 350 N, which was 2.8 and 4.1% less than H1 and H2, respectively. Then, a decrease in the yielding load was shown by H5 at 330 N. This huge decrease is 9.6% less than H2 and 5.7% less than H3 and H4. Hybrid H6 performed better than H5 and failed close to H3 and H4 at 345 N. It was observed that by gradually replacing the carbon fiber layers toward the outer side (tension side) of the specimens, the lower the yielding loads provided, as shown by H3, H4, H5 and H6. This observation agrees with the results elaborately explained in the literature review. Finally, specimen S8 yielded at 370 N as a result of its high stiffness.

Despite yielding at different levels of loading points, Hybrids H1, H2, H3 and H4 yielded at approximately the same deflection values as S1, ranged from 2.87 mm to 2.80 mm, as shown in Figure 3-19(b). These results support the P_{yld} results of the same hybrids as they yielded at approximately the same P_{yld} values. The highly stiffened specimens H5, H6 and S8 deflected less than other specimens as they also have the highest flexural rigidity delivered by placing the carbon fiber layers at the outer sides of the specimens. The 9.1% clear drop on w_{yld} from H4 to H5 suggests that H5 and H6 perform more efficiently in terms of yield load and deflection resistance compared to other hybrids.

Table 3-3: 3-Point bending test results

	P_{yld}, N (CV)*	w_{yld}, mm (CV)	P_{ult}, N (CV)	w_{ult}, mm (CV)	σ_{yld}, MPa (CV)	σ_{ult}, MPa (CV)	τ_{cs}, kPa (CV)
S1	360 (±0.80)	2.87 (±0.02)	455 (±1.10)	4.12 (±0.02)	39.7 (±0.01)	50.0 (±1.10)	592 (±1.10)
H1	360 (±2.41)	2.80 (±0.01)	445 (±2.34)	4.0 (±0.001)	40.5 (±2.28)	50.0 (±2.16)	591 (±2.12)
H2	365 (±0.80)	2.84 (±0.01)	425 (±1.68)	3.50 (±0.01)	41.0 (±1.13)	47.0 (±1.07)	558 (±1.00)
H3	350 (±2.47)	2.83 (±0.02)	440 (±0.66)	4.18 (±0.02)	39.4 (±2.49)	49.0 (±0.58)	584 (±0.66)
H4	350 (±0.82)	2.87 (±0.01)	445 (±0.65)	4.19 (±0.02)	39.4 (±0.88)	50.0 (±0.58)	591 (±1.77)
H5	330 (±0.87)	2.61 (±0.01)	430 (±0.67)	3.99 (±0.05)	36.5 (±1.04)	48.3 (±1.56)	571 (±1.58)
H6	345 (±0.80)	2.87 (±0.02)	461 (±1.10)	4.12 (±0.02)	37.8 (±1.46)	45.0 (±0.00)	533 (±2.80)
S8	370 (±0.80)	2.87 (±0.02)	462 (±1.10)	4.12 (±0.02)	40.8 (±0.00)	53.0 (±0.56)	629 (± 0.52)

* (CV): coefficient of variance

After reaching their yield points, the specimens pass through the transition zone, where the rate of applied bending load to deflection starts to decrease gradually up to the loading point where the specimens fail and lose their structural integrity. This failure loading point signifies the ultimate load that specimens can carry before failure. Therefore, at this ultimate load point, it is interesting to analyze the specimens' ultimate load resistance and their maximum allowable deflection to determine the effect of the different hybrid face sheet stacking sequences on the ultimate performance. The ultimate load P_{yld} and P_{ult} can be substituted into equation 3-1 to find the face sheet stresses σ_{yld} and σ_{ult}. From Table 3-3, the ultimate face sheet stresses provided the same performance as the ultimate shear stresses for all specimens as this test was designed to test the core shear properties. Therefore, the face sheet stress performance of all specimens resemble the core shear stress performance as the specimens mainly failed due to core shear deformation. The ultimate deflection for all hybrids other than H2 and H6 were approximately equal to the ultimate deflection of S1. Hybrids H2 and H6 again provided the best lower deflection resistance due to their stiff performance. However, H2 performed better than H6 with respect to the yield performance. Figure 3-19 (a, b, c and d) shows the tradeoff using highly yielded H2 on the ultimate performance of the desired design specimen. Hybrid specimen H6 delivered the least performance of all the hybrid specimens by failing the earliest at the lowest stress rates. This weak performance of H6 suggests that this sequence of carbon and glass layers is not preferable for resisting flexural loading. Specimen S8 performed the best in resisting the applied flexural load by delivering the highest P_{yld}, τ_{cs}, and σ_{fc} as a result of its higher flexural rigidity and stiffness.

All tested specimens exhibited the same failure mode, which is actually three failure modes occurring in sequence one after the other. The first failure mode occurred as a global deflection failure when the specimens started to bend under the exerted load. The second failure mode was caused by a core-face debonding failure between the weak core and the strongest and highly stiffened face sheets caused by the shear stresses generated between the core and the face sheets. As the load continued, the stress concentration increased at the contact area between the specimens' upper face sheets and the roller attached to the test machines' upper moving head. This last mode of failure can be described as a fiber and matrix crushing failure, as explained in Section 2.8.1. Accordingly, the tested specimens show the first, second and third modes of failure as explained previously. Figure 3-18 shows an example test specimen with the three failure modes in a picture taken by a Celestron© digital microscope equipped with a 2 MP digital camera with a maximum

zoom of 150x. The effect of the bending failure mode is clearly shown by the intersecting dashed red lines between the core and both face sheets. The bending trace on the upper face sheet is clearer than that on the lower face sheet due to the crushing failure of the highly stressed contact area. By zooming in further on the crushed zone, the fiber-matrix fracture across the face sheet lamina can be visibly observed, and the foam core is clearly compressed. The crushing zone contained fractured and delaminated fibers. On the other hand, there is no sign of any failure other than global bending failure at the lower face sheet. Thus, the lower face sheet did not fail under the tensile stresses during the global bending failure. With this in mind, it was observed that the stacking sequence of the carbon and glass layers within the face sheets strongly affects their performance, as thoroughly discussed in the literature. Indeed, it was shown that by placing the carbon fiber layers at the outer side of the upper face sheets lamina, the lamina tends to crush earlier than when the outer layer is a glass fiber layer. This might occur due to the higher tensile or compressive failure strain of the glass fibers compared to the carbon fibers. In addition, the impact energy absorption of the carbon fibers is less than that of the glass fibers (Mallick, 2007), which might influence the resistance of the impact effect caused by the moving roller attached to the test machine upper head during loading.

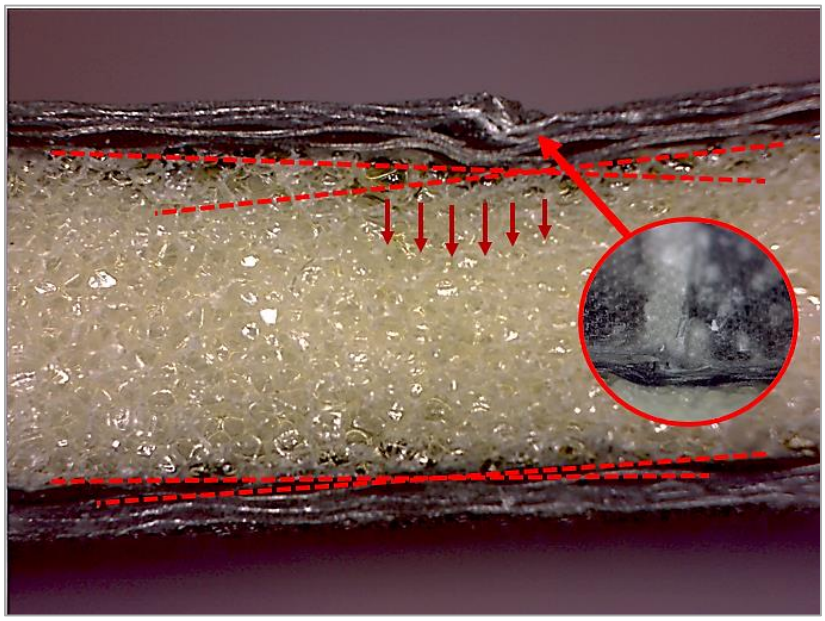

Figure 3-18: Microscopic bending failure zones view

In conclusion, hybrid H2 performed better than the other hybrids with respect to the yield load despite having less flexural rigidity than H3, H4, H5 and H6. However, hybrid H2 ultimately deflected less than the other hybrids except for H6. Therefore, the unique performance of hybrid H2 supports the occurrence of the hybrid effect for specimens made with the same carbon-to-glass inter-ply ratio with different stacking sequences within their face sheets. These results can help to better understand the buckling behavior of hybrid sandwich panels as they pass through a complicated compression-bending loading condition during a buckling test.

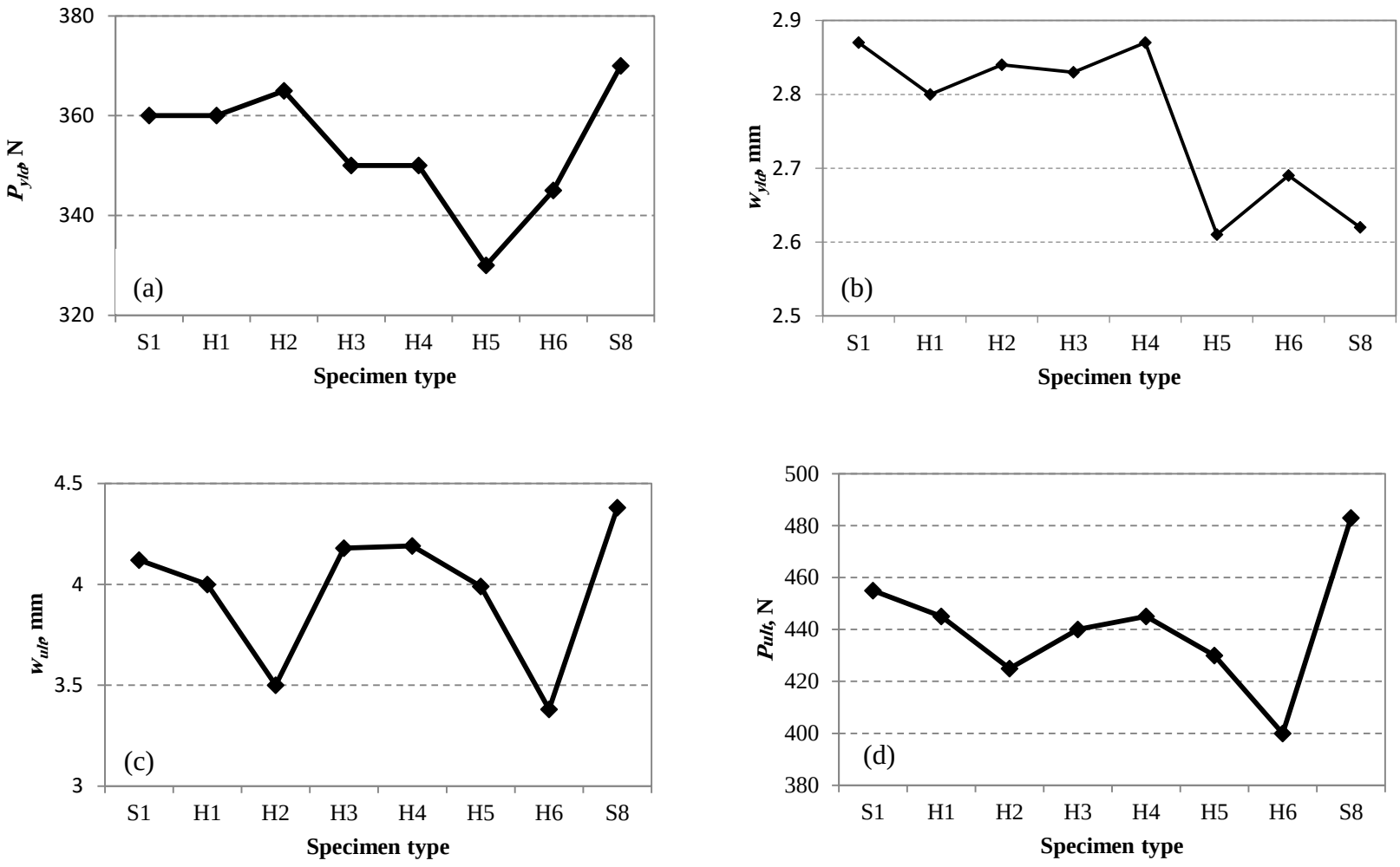

Figure 3-19: (a) P_{yild} for all tested specimens. (b) w_{yild} for all tested specimens. (c) (a) w_{ult} for all tested specimens. (d) P_{ult} for all tested specimens

3.6 Buckling Test Set-up

The buckling test was performed according to ASTM C364/C364M-07 using a hydraulically operated 600-ton universal test system AMSLER equipped with a 10 kN load cell, as shown in Figure 3-20. All specimens were tested in a controlled displacement procedure at room temperature. However, AMSLER is capable of performing force controlled tests. The mounting fixture used in the buckling tests had two main parts, and each part had a fixed support boundary condition. The mounting fixture was used to fix the specimens' short (2 in) horizontal edges at the top and the bottom, while the vertical edges were left unconstrained. A proper alignment between the fixed test specimen central axis and the test machine cross head motion axis was set to minimize any misalignment errors that affect the reliability of the results. Next, a uniform compressive pressure was applied through the controlled displacement of the test machine upper moving head at a rate of 1 mm/min by compressing the specimens against the machine's fixed bottom bed. The loading continued until the specimen reached its failure loading point P_{ult}.

Figure 3-20: AMSLER 600-ton universal test machine

The data recording of the out-of-plane deflection (*w*) was set to be measured by the non-contact laser displacement sensor with a high spatial resolution of 8 µm and a large working distance of 30 ~ 80 mm. For each specimen, a pair of laser sensors were positioned back-to-back and were focused on the center point of the specimen on each face sheet. Two wenglor®-CP08MHT80 reflex non-contact laser beam sensors were used to capture the positive and negative out-of-plane deflections, as shown in Figure 3-21. A custom-written code in LabVIEW® was used to record the compressive load, applied in-plane displacement and out-of-plane deflection at consistent time intervals.

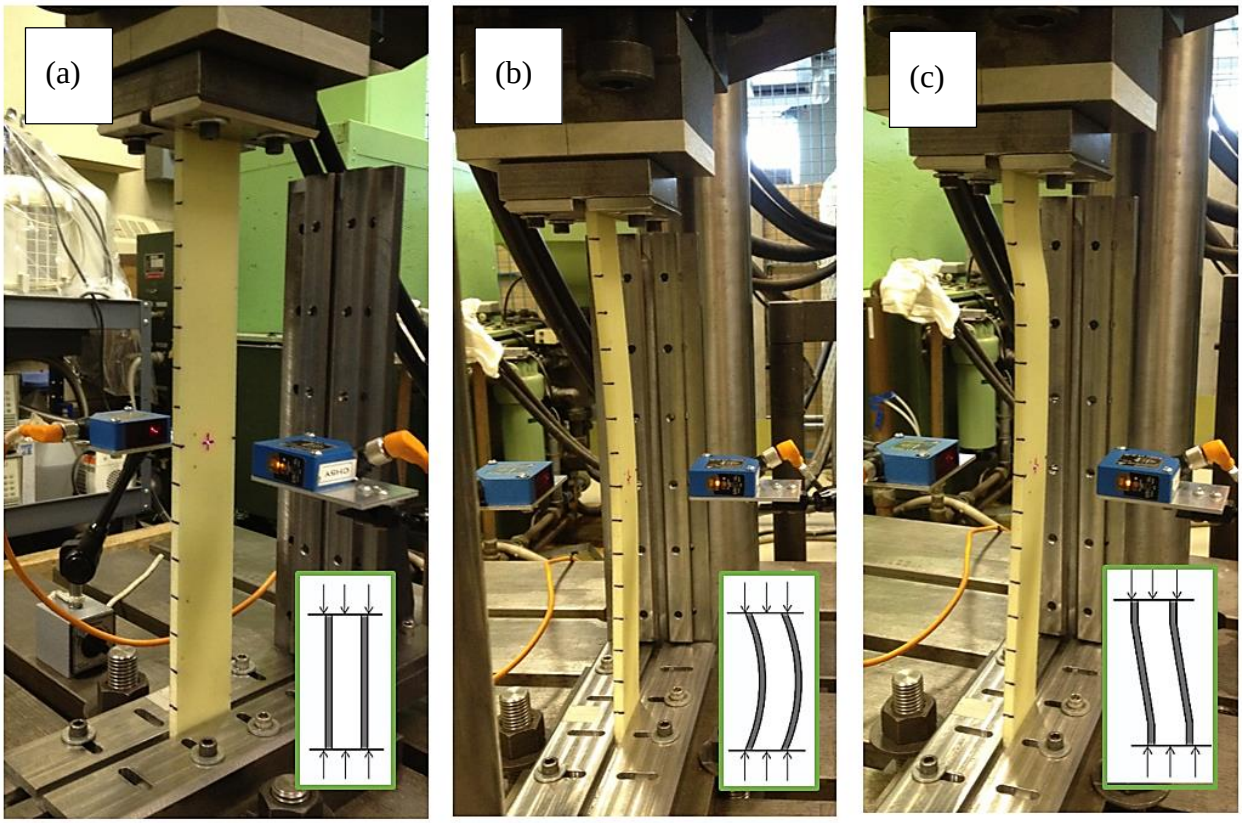

Figure 3-21: Buckling test set-up. (a) specimen under pure compression loading. (b) specimen starting to deflect (global buckling failure). (c) shear crimping failure of specimen.

3.7 Experimental Test Results

3.7.1 The Extraction of P_{cr} from the Experimentally Recorded Data

Historically, the extraction of P_{cr} from experimental data taken from buckling performance tests of engineering structures was obtained using a number of different methods such as Southwell, top of the knee, strain reversal and the average stress per unit method (Figure 3-22). In fact, there is a lack of consensus about which P_{cr} extraction method provides the most accurate critical buckling load point from experimental data curves.

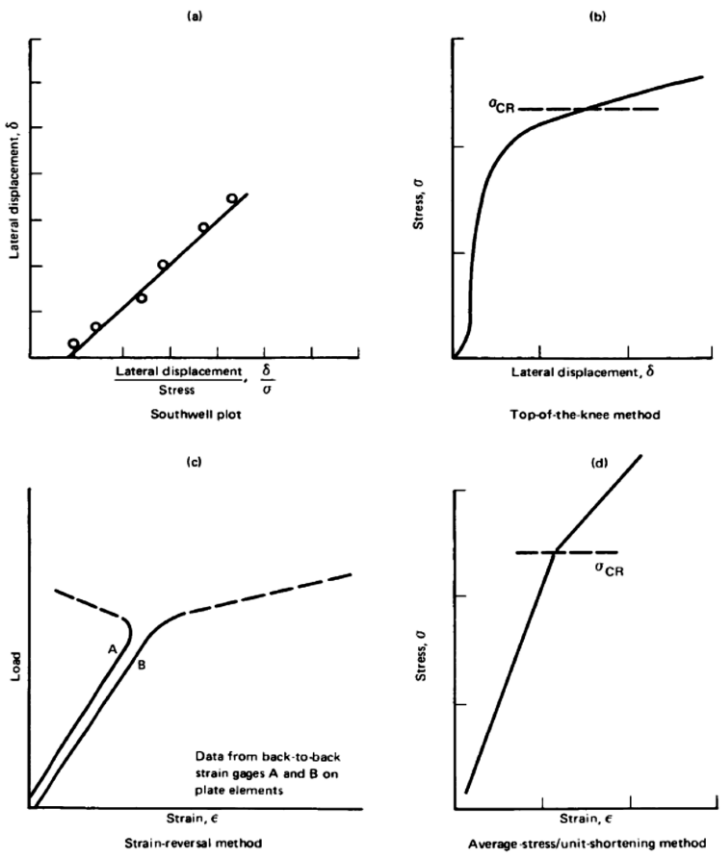

Figure 3-22: Methods of extracting P_{cr} from experimental data. (a) Southwell plot, (b) top-of-the-knee method, (c) Strain-reversal method and (d) average stress/unit-shortening method (Plates, 1971)

(Marouene, Boukhili, Chen, & Yousefpour, 2016) studied the buckling and post-buckling behavior of variable stiffness composite panels and proposed a conservative method to extract P_{cr} from their load-displacement curves. First, they divided the load-displacement curve into four consecutive zones that describe the buckling behavior of panels during the buckling test. The tested panels initially exhibited non-linear behavior (Zone I) caused by the initial geometric loading-surface imperfections. In Zone II, the panels showed a compressive linear behavior that signifies the panels' linear elastic properties, followed by a non-linear transition path (Zone III) that represents the buckling starting point. Ideally, in perfect panels, P_{cr} can be identified as a distinguishable bifurcation point at the load-displacement curve. However, due to test and specimen imperfections, P_{cr} occurs within the non-linear transition path; the transition zone was defined as the bounded path between the tangents of the Zone I and Zone IV. Finally, Zone IV displays the continuation of the panels' non-linear buckling failure until failure. Therefore, they considered P_{cr} to be the load point where the load-displacement curve starts to diverge from its linear pre-buckling curve between Zone II and III. A graphic explanation of the method proposed by Marouene et al. is illustrated in Figure 3-23.

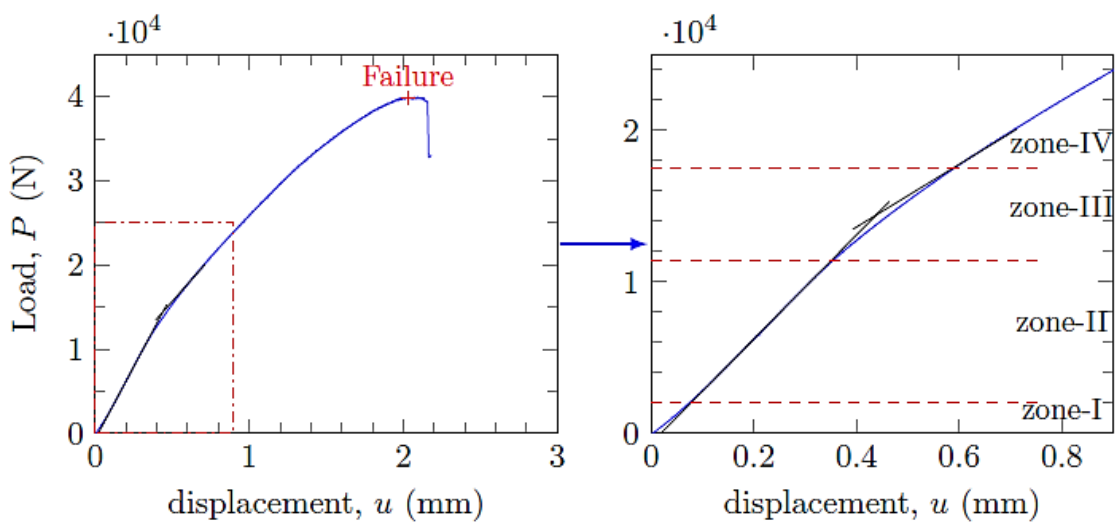

Figure 3-23: Experimental buckling curve divided into 4 zones (Marouene et al., 2016)

In sandwich panels, the extraction of P_{cr} from the experimental data has been studied by (Minguez, 1986) for various support conditions. In his study, Minguez used the Southwell method to determine P_{cr} as the slope of the fitted curve between the out-of-plane displacement w and the applied load P. Later, this study was criticized by (Chau, 1987) for using a method that was constructed strictly for columns. Moreover, the Southwell method sensitivity is highly dependent on the number of data points from the experimental data used to obtain P_{cr} as the slope of the curve between w and w/stress (Carlsson & Kardomateas, 2011).

Experimentally, the sandwich panels will buckle after undergoing a compression state followed by a compression-flexural state that continues until crimp failure. This buckling behavior is relatively similar to the buckling behavior of composite panels tested by (Marouene et al., 2016), and its load-displacement curves can also be divided into four zones. Therefore, the investigated P_{cr} will be extracted by following his conservative method. The complexity of the loading condition effects on the sandwich panels that varied between compression and bending and its influence on the hybrid effect was the aim of this study.

3.7.2 Buckling Test

The back-to-back non-contact laser sensors read the out-of-plane deflection of both sides of the specimens. The moving face sheet provides negative readings as the distance between the specimen and the laser sensors decreases. Conversely, the other face sheet tends to move away from the laser sensor, so the distance between the specimen and the sensor increases, which is recorded as a positive reading. With every test specimen, the positive deflection readings of the laser sensors record smaller P_{cr} values than the negative deflection readings for the same specimen whether it deflected to the right or to the lift. Hence, at a certain point of loading, one of the two face sheets buckled slightly earlier than the other one. Then, the buckled face sheet directed the out-of-plane deflection toward the other face sheet, causing load redistribution and exciting the second face sheet to buckle. As a result, global buckling occurred, and the specimen deflection permitted the specimen to leave Zone 1 and enter Zone 2, as shown in Figure 3-24. After reaching P_{cr}, the sandwich panels lost their integrity as a whole intact structure and their ability to maintain stiffness.

The initial side deflection suppressed the symmetrical character of the sandwich panel face sheets, causing unequal load resistance as each face sheet had its own flexural rigidity. By increasing the load, the specimens in Zone 2 deflected more, and their resistance decreased gradually until core-face sheet debonding failure caused by the transverse shear deformation occurred, as shown in Zone 3. Therefore, the hybrid effect of using different stacking sequences of carbon and glass fiber layers are clearly shown in Table 3-3 and Figure 7. The average P_{cr} is the average value of the P_{cr} extracted from the positive and negative out-of-plane curves for the same type of specimens. At least 4 specimens from each hybrid type and 3 S1 and S8 specimens were tested and recorded.

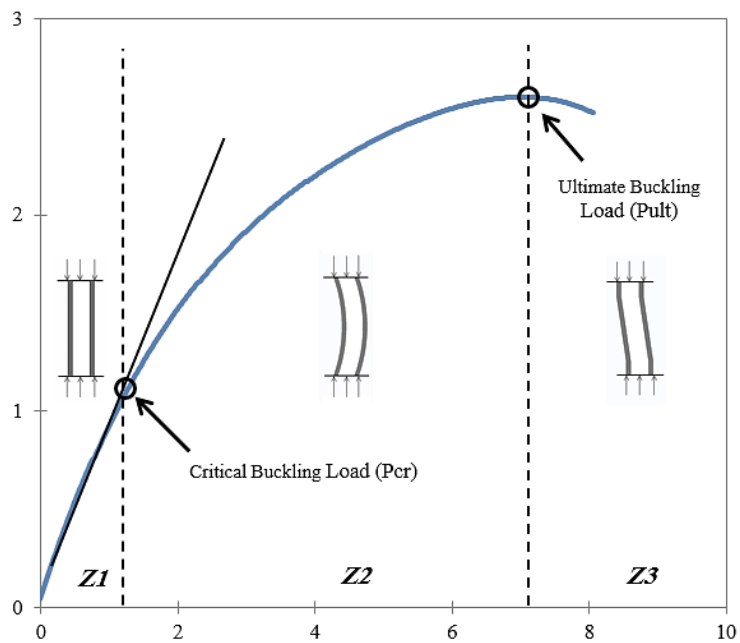

Figure 3-24: Specimens failure zones on the load vs out-of-plane deflection curve

Table 3-4: Buckling test experimental results

	P_{cr} [Exp], N			W_{max}, mm (CV)	P_{ult}, N (CV)	d_{ult}, mm (CV)
	P_{cr} [-w] (CV)*	P_{cr} [+w] (CV)	Avg P_{cr} (CV)			
S1 [G_4/R/G_4]	1528 (±17)	1562 (±52)	1545 (±35)	6.66 (± 0.32)	2609 (± 223)	1.39 (± 0.08)
H1 [G_2C_2/R/C_2G_2]	1873 (±42)	1981 (±75)	1927 (±59)	5.56 (± 0.41)	3312 (± 279)	0.88 (± 0.08)
H2 [GCGC/R/CGCG]	2313 (±94)	2407 (±111)	2360 (±102)	4.76 (± 1.01)	3706 (± 161)	0.86 (± 0.10)
H3 [GC2G/R/GC2G]	1961 (±115)	2087 (±127)	2024 (±121)	4.88 (± 0.97)	3578 (± 191)	0.86 (± 0.04)
H4 [CG2C/R/CG2C]	2083 (±47)	2096 (±61)	2090 (±54)	4.55 (± 0.37)	3449 (± 28)	0.78 (± 0.03)
H5 [CGCG/R/GCGC]	1992 (±53)	2074 (±30)	2033 (±41)	4.93 (± 1.04)	3429 (± 129)	0.87 (± 0.04)
H6 [C2G2/R/G2C2]	1934 (±73)	1988 (±76)	1961 (±75)	5.06 (± 0.54)	3251 (± 118)	0.95 (± 0.11)
S8 [C4/R/C4]	2584 (±53)	2584 (±66)	2584 (±59)	1.83 (± 0.52)	4366 (± 207)	0.79 (± 0.01)

* (CV): coefficient of variance

From Figure 3-25, the failure mechanism of each panel differs due to the difference in the flexural rigidity controlled by the positions of the carbon and glass layers within the face sheet lamina. This asymmetrical effect of the face sheets during buckling was analyzed for each layer within both sheets, and the fiber layers were numbered from the bottom layer to the top as L1-L8. For example, in H1, the face sheet elastic properties, such as E_x and E_y, were the same as they both have the same number of carbon and glass layers. Thus, both face sheets resist and perform similarly under compression load, as observed in Zone 1. However, when the test specimens entered the buckling of Zone 2, the specimens' flexural rigidity started to resist the bending action. The symmetrical stacking sequence of glass and carbon layers between L1-L4 and L5-L8 created two distinct flexural rigidities acting simultaneously. Hence, the face sheet with L1-L4 layers had the carbon fibers at the tension side and the glass fibers at the compression side, while the other face sheet with L5-L8 had the carbon fibers on the compression side and the glass fibers on the tension side. This transformation from Zone 1 to Zone 2 and the effect of the unequal flexural rigidity of the face sheets contributed to the hybrid effect.

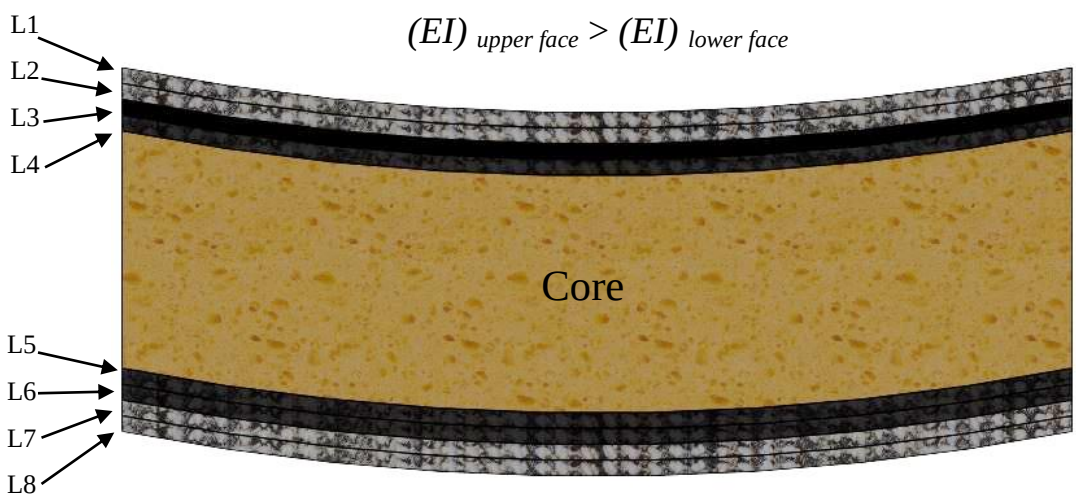

Figure 3-25: Sandwich panel face sheet lay-up and different flexural rigidities of the face sheets during bending

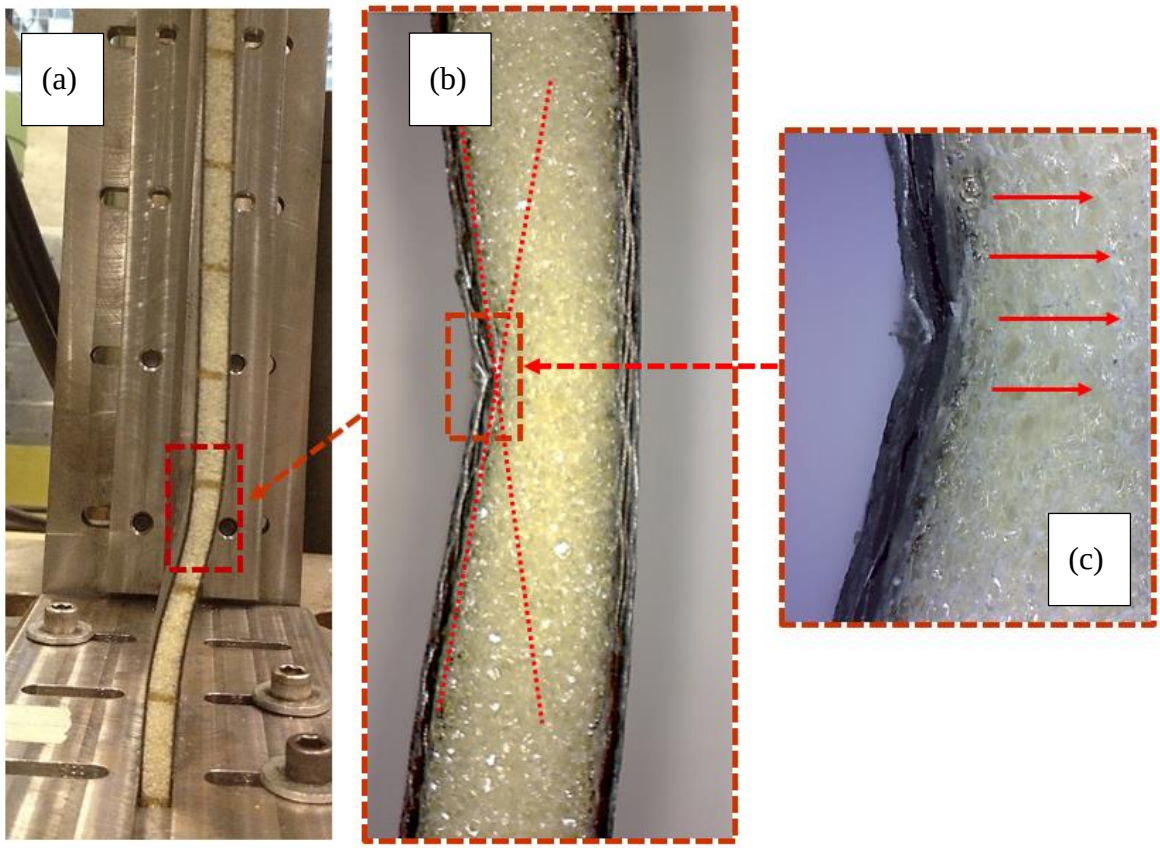

Figure 3-26: : Microscopic buckling failure zones: (a) shear crimping failure, (b) failure zone at 10x zoom, (c) failure zone at 150x zoom

Using a digital microscope, the area of the shear crimping failure that was followed by the initial global buckling failure was investigated, as shown in Figure 3-26. Figure 3-25(b) clearly shows that the specimen's face sheet with positive deflection readings from the non-contact laser sensor was compressed at intersection of the dotted red lines. This compressed area is where the debonding between the core and the deflected face sheet occurred due to the transverse shear stresses generated between the core and the face sheet. In addition, the other deflected face sheet never failed and continued in an intact condition. However, by increasing the load, the compressed face sheets continued to compress the foam core up to a load level where the failed face sheet lamina started to crush under the applied load, causing fibers fractures and delamination. In spite of this failure, the tested specimens continued to carry the applied load at a lower load level until their final failure.

3.7.3 Load Vs. In-plane Displacement

The compressive load exerted by the test machine's controlled displacement cross head was measured by the machine's 10 kN load cell and recorded by LabView® at consistent time intervals at a speed of 1 mm/min. In general, all of the tested specimens clearly buckled under the gradually applied compressive load, as shown in Figure 3-27. The specimens went through all of the typical buckling zones explained in Section 3.7.2 until failure. The specimens' ultimate load and failure displacement were easy to find at the maximum recorded load. In contrast, the extraction of P_{cr} from the load vs. in-plane displacement curve was not easy. Thus, the P_{cr} extraction was taken from the load vs. out-of-plane curve recorded by the non-contact laser sensors.

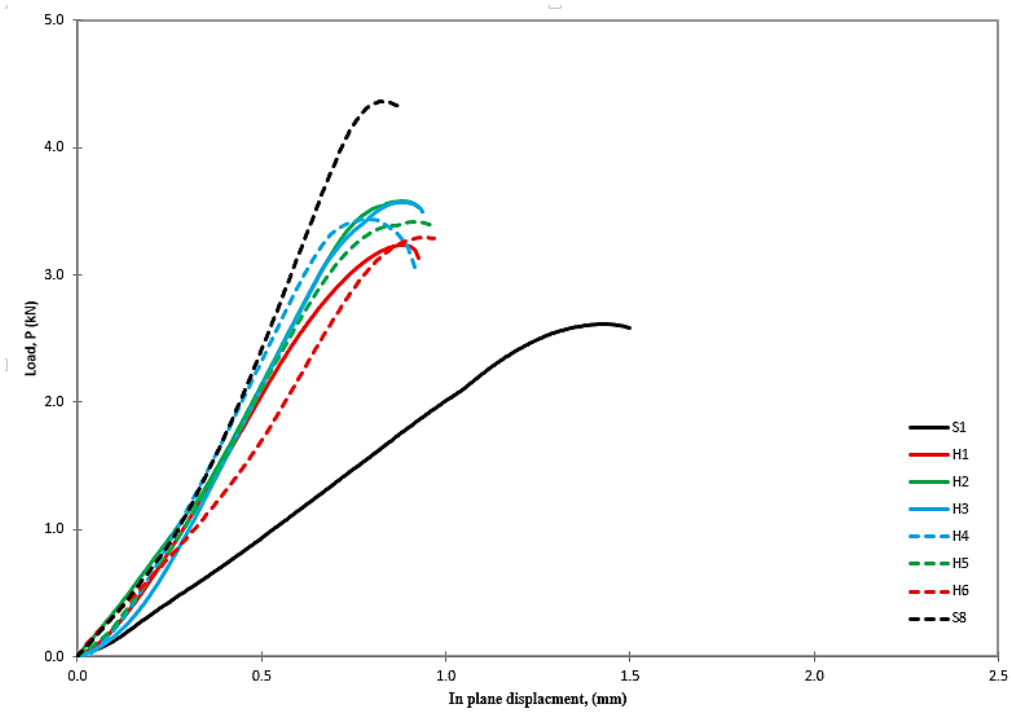

Figure 3-27: : Load vs. In-plane displacement performance

Figures 3-27 and 3-28 show an apparent hybrid effect for the hybrid samples compared to the two reference baseline specimens of sandwich panels made from all-glass or all-carbon face sheets. All specimens started the compression test and performed as an intact structure by bearing the compressive load caused by the controlled in-plane displacement of the test machine's crosshead. After reaching buckling load P_{cr}, the specimens started to behave non-linearly with a reduction in the effective axial stiffness with increasing load. Under these circumstances, the specimens started to bend away from their original plane position, leading to out-of-plane deflection that is physically denoted as global buckling failure. This failure occurs when the specimens' core shear strength is not able to resist the core's shear deformation. Thus, the specimens reached their maximum strength, and shear crimp failure occurred at a location close to one of the specimen's short, clamped edges. In fact, the specimens continued to carry a lower load than its initial capacity until final failure.

The addition of carbon fibers improved P_{ult} of the all-glass specimen by a varied range of 19.8–29.6% between all six hybrid specimens. Hybrid H2 provided the maximum P_{ult}, while H6 failed with the smallest P_{ult}. Therefore, a communal positive hybrid effect on P_{ult} can be observed due to the variation of P_{ult} among hybrid specimens, as shown in Figure 3-28. The relatively stiff hybrid performance of H2 caused the specimen to resist more loading than the other hybrids, which lead to a better P_{ult}. The relative stiffness of H2 was caused by the alternating sequence of carbon and glass layers within the face sheets, which allowed the occurrence of the bridging effect during Zone 1. Furthermore, the P_{ult} of H2 provided a hybrid effect that was 3.5%, 6.9%, 7.5% and 12.3% larger than those of H3, H4, H5 and H6, respectively, and 15.1% less than the P_{ult} of S8. On the other hand, hybrid H6 failed earlier because the glass fiber layers L5 and L6 were located at the tension side in one of the deflected face sheets. Although the P_{ult} values of the hybrids were less than that of the all-carbon specimen S8, the hybrids (except for H4) had improved the ultimate failure in-plane displacement d_{ult} of S8 by 8.1 – 16.8%.

From Figure 3-29, S1 delivered the highest d_{ult} value as it was less stiff than the other specimens. On the other hand, the highly stiffened specimen S8 failed earlier than the other specimens at 0.79 mm. Hybrids H1, H2, H3, H5 and H6 failed at approximately the same in-plane displacement, which ranged from 0.86 to 0.95 mm. Hybrid H4 failed at approximately the same in-plane displacement (d_{ult}) as S8 (0.78 mm). This might happen due to positioning two carbon layers L4

and L8 at the compression sides of both face sheets. This carbon fiber layers positioning was only found in H4; according to previous studies mentioned in the literature review, the carbon fibers are weaker when placed at the compression side of the laminates. Therefore, a negative hybrid effect was observed for H4, and a positive hybrid effect was observed in the ultimate in-plane displacement failure for the other hybrids. All of the hybrids except H4 arrested the catastrophic buckling failure of S8, and they had greater load bearing capacity than S1.

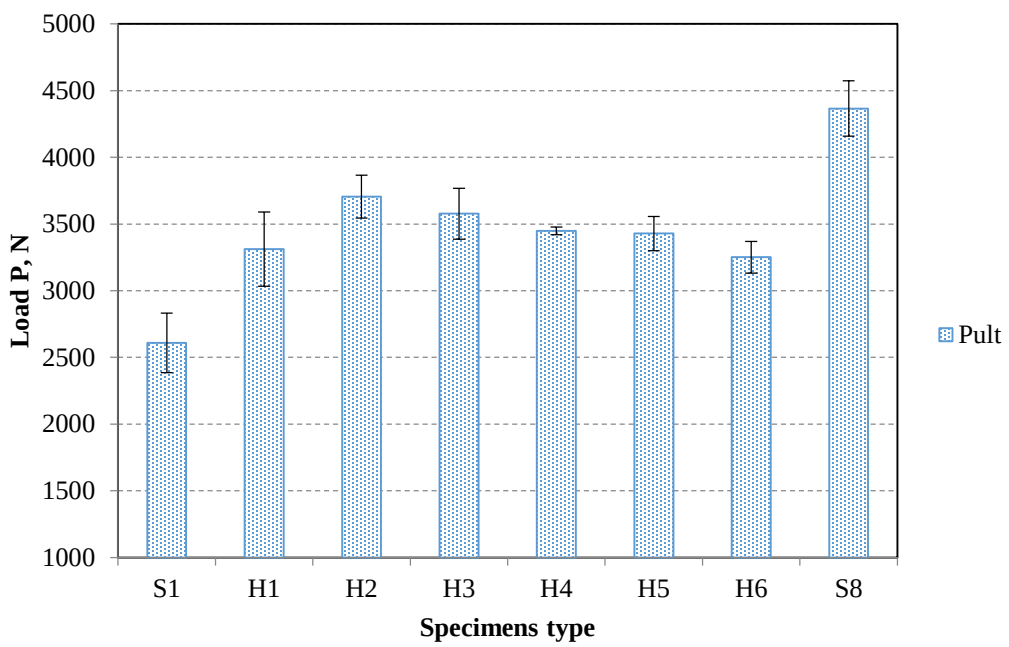

Figure 3-28: P_{ult} load for all tested specimens

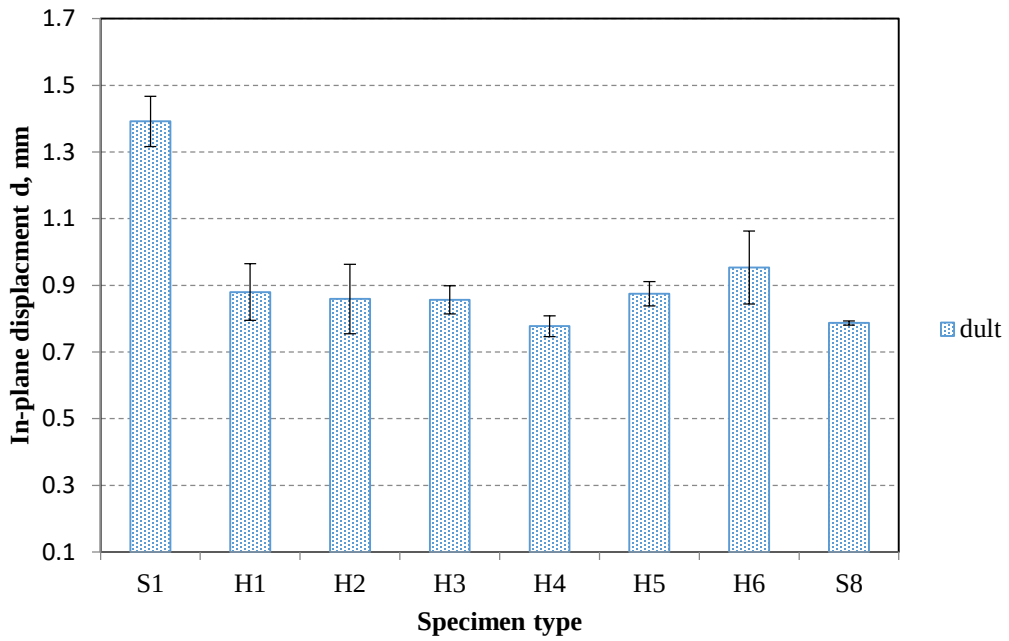

Figure 3-29: d_{ult} load for all tested specimens

3.7.4 Load Vs. Out-of-plane Deflection

The collected data from the back-to-back non-contact laser sensors for the hybrids and the reference baseline specimens are illustrated in Figure 3-30. Section 3.4 showed that the tested hybrid specimens clearly buckled under the applied load. Thus, the accompanied out-of-plane deflection with buckling also occurred and was recorded in the same fashion at regular time intervals. Here, the hybrid effect of the average P_{cr} is related to the deviation of the experimental results from the analytically calculated values of P_{cr}.

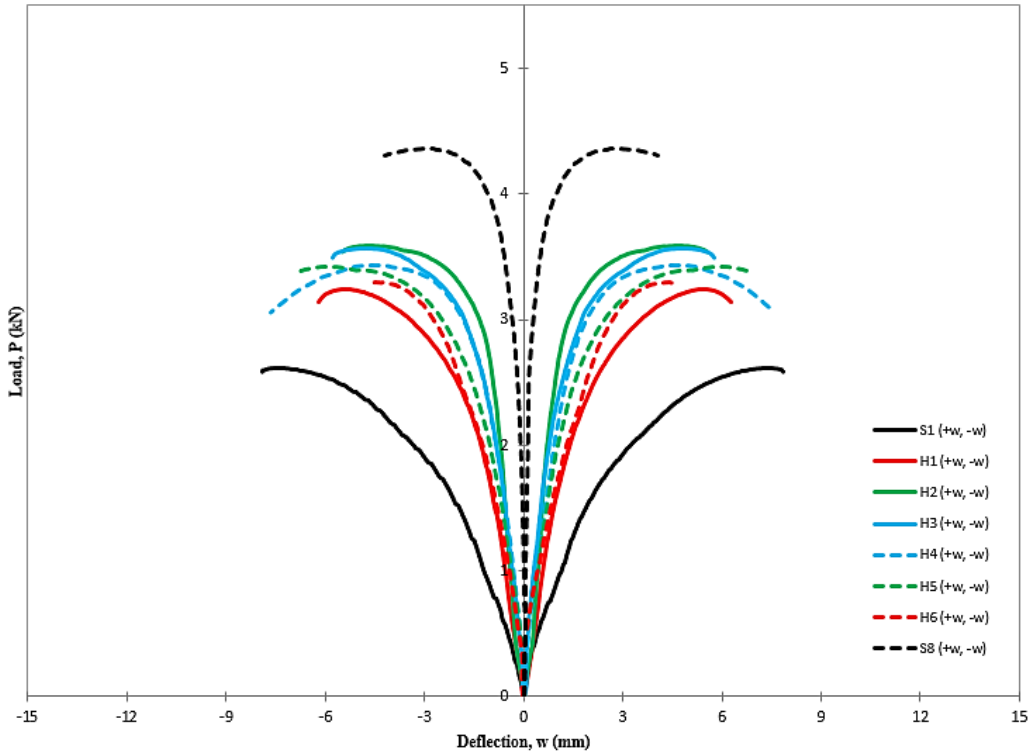

Figure 3-30: Load vs. out-of-plane deflection

From Figure 3-31, hybrid H1 placed 50% of the low stiffness glass layers at the outer side of the face sheets (L1, L2, L7 and L8), causing the sandwich to buckle at a load approximately 20% greater than the buckling load of S1 but less than that of the other hybrid specimens. Similarly, H6 buckled earlier than H2, H3, H4 and H5 due to its lower longitudinal stiffness E_x, but it buckled later than H1 because of the higher flexural rigidity delivered by the outer carbon layers (L1, L2, L7 and L8) resisting both positive and negative out-of-plane deflection (+*w* and -*w*). Hybrid H6 slightly improved P_{cr} by 1.7% from the P_{cr} value of H1. In both hybrids, the high stiffness carbon fibers layers reached their maximum allowable elongation, while the glass fibers continued to carry the load until fracture. Hybrids H3 and H4 showed a similar balanced performance. Both positive and negative deflections (+*w* and –*w*) of the face sheets had the same type of fiber layers (L1: L8) in the deflection direction; these hybrid layers acted as expected by improving the sudden failure nature of carbon fibers. The P_{cr} of H3 and H4 improved the buckling resistance of H6 by 3.2% and 6.2%, respectively. Hybrid specimen H5 buckled earlier than H3 and H4 as its face sheets were

less stiff. The large difference in EI_f for both face sheets in H5 caused failure in the positively deflected face sheet, which is represented as a failure in layer L5 followed by layers L6 and L7; load redistribution transferred more load to the negatively deflected face sheets, causing it to buckle. On the other hand, hybrid panel H2 benefited from the difference between the face sheets' EI_f. The bridging effect of the alternating stacking sequence of the fiber layers during the compression period in Zone 1 helped to delay buckling. The positively deflected face sheet had two carbon fiber layers L5 and L7 that helped to delay the buckling failure. Thus, hybrid panel H2 provided a positive hybrid effect that was 14.2%, 11.4%, 13.9% and 16.9% greater than those of H3, H4, H5 and H6, respectively. Moreover, the P_{cr} of H2 is only 8% less than the P_{cr} extracted from the all-carbon specimen S8.

The maximum out-of-plane deflection is the maximum distance traveled by the center point on the deflected face sheet from its original planar position to a new position in space through a perpendicular path. Here, only the positive deflection is analyzed to avoid duplication. It has been shown that w_{max} of the all-glass specimen S1 was improved by at least 16.6% by adding the carbon fibers. The values of w_{max} for the hybrids ranged from 16.6% to 31.7%, proving the presence of a hybrid effect compared to S1. However, the coefficient of variance for the hybrid w_{max} values suggest that all of the hybrid specimens failed at approximately the same value, as shown in Figure 3-32. Therefore, the hybrid specimens might finally failed as a result of the face-core debonding influenced by the shear deformation failure.

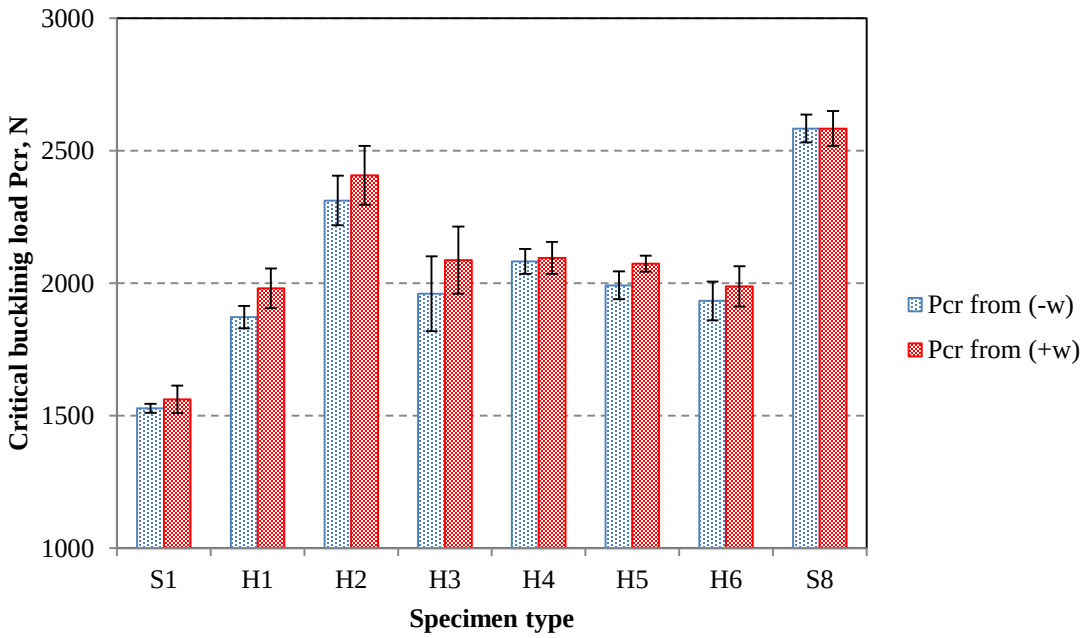

Figure 3-31: Pcr extracted from both +*w* and –*w*

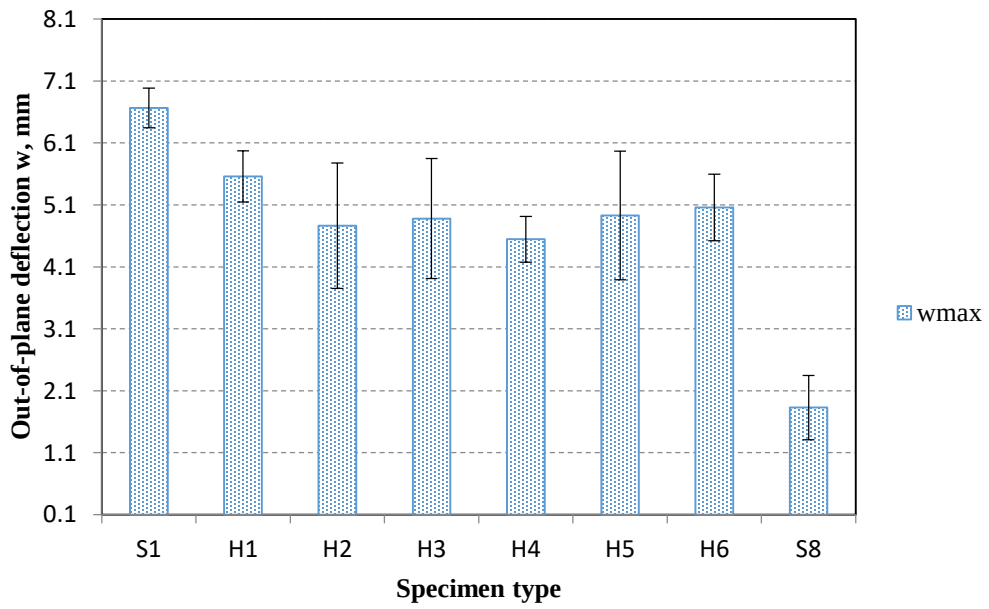

Figure 3-32: w_{max} load for all tested specimens

CHAPTER 4 NUMERICAL MODELING

The numerical simulation of composite structures can be modeled using either micro-mechanical or macro-mechanical methodologies. In the micro-mechanical scale, the relation between the fibers and the matrix can be fully studied in detail. However, this type of numerical modeling is expensive when used to model real applications (Kreja, 2011). On the other hand, macro-mechanical modeling can easily simulate composite structures by modeling the composite laminate as a number of stacked and bonded homogenous layers that represent an intact body. Studies on macro-mechanical composite modeling have two distinct approaches for modeling and simulating composite structures. These two modeling approaches are Equivalent Single Layer (ESL) and Discrete Layer (DL) modeling. For ESL modeling, the laminate is molded as a homogenous single layer structure with equivalent mechanical properties calculated from the macro-mechanical properties of each layer within the lamina. Initial studies on ESL modeling used CLPT developed by Kirchhoff-Love as a formulation for thin laminate with non-linear or large displacement applications (Jones, 1999); (Vinson, 1975); (Rohwer K., 2005); (Ambartsumyan, 1970). However, CLPT did not reflect the practical transverse shear deformation that was considered later with the development of the SDPT theory; creating a universal model is difficult. As a result, the importance of including the SDPT formulation in numerical modeling led to the development of DL modeling as a multi-layered structure. Sandwich panels can be modeled as multi-layered structure with special modeling compliance adjustments to numerically simulate the existence of the relatively light and weak core and its interaction with the face sheets (Kreja, 2011). In sandwich panels, the core does not transmit load as much as the face sheets due to its low in-plane performance. However, the core's shear stiffness and its resistance to shear deformation must be considered when modeling sandwich panels due to the core's effect on the sandwich panel performance. (Marcinowski, 2003) developed a non-linear sandwich panel model with an 8-node shell element by simulating the face sheets as thin membranes without flexural stiffness. (Das, Barut, Madenci, & Ambur, 2005) used the High Order Shear Deformation (HOSD) formulation to model a sandwich panel using a triangular element with 3 nodes and 39 DOFs. (Tanov & Tabiei, 2000) used their parametric *Sandwich Homogenization Procedure* to model a homogeneous sandwich shell solved using the CDPT formulation. Further research used the industrial and educationally available commercial FEA packages to design and model composites structures. (Rolfes & Rohwer, 1997) developed their own code to adjust and improve the implementation of CDPT

formulation used to simulate the transverse shear stiffness of laminated composites modeled using MSC Nastran by neglecting the membrane forces. (Hu, 1995) used ABAQUS to construct a non-linear model to study the non-linear buckling behavior of a composite plate under a uniaxial compressive load as well as its relation to in-plane shear stress and failure criteria. (Sze, Chan, & Pian, 2002) non-linearly modeled 8 sets of famous benchmark composite problems using ABAQUS and noticed solution convergence difficulties with automatic load increments for maximum loads.

In this chapter, two numerical models are developed to simulate the experimental behavior of specimens in a 3-point bending test and buckling test. Each numerical model was simulated and solved using the ANSYS Mechanical APDL V13.0 FE package.

4.1 Flexural 3-Point Bending Model

The model for this numerical analysis were derived from both the ESL and DL modeling methods for both face sheets by first calculating the equivalent mechanical properties of each hybrid face sheets considering the different stacking sequences. Obviously, the difference in stacking carbon and glass layers within face sheets laminates in symmetrical or asymmetrical forms results in different mechanical properties. Hybrids H1 and H6 share the same mechanical properties as they have the same stacking sequence of both carbon and glass layers but in reverse order. Therefore, the numerical results for H1 and H6 have the same values. The same is true also for H2 and H5 as well as H3 and H4, as they have the same stacking sequences. Second, each face sheet was modeled as a DL with four layers stacked on top of each other but with each layer having the same hybrid equivalent properties (see Figure 4-1 (a)). This modeling method is used later to obtain the stress distribution across the thickness of the modeled sandwich panels.

The FE numerical model was initially created as a 2D area representing the experimental test specimens. The 2D area was then defined as a sandwich panel by entering the stacking sequence of carbon and glass layers along with the middle core. The thickness of each composite layer was obtained from equation 4-1 by calculating the coefficient of equilibrium k for the woven fabrics used (see Figure 4-1 (b)). The model was then meshed using the shell element Shell 281, as shown

in Figure 4-2, and was constrained at the short edge using simply supported conditions ($U_x = U_z = 0$). The exerted load was set to be a displacement along the model's short center line parallel to the short edges to simulate the loading conditions of the experimentally controlled displacement, as shown in Figure 4-3 (a).

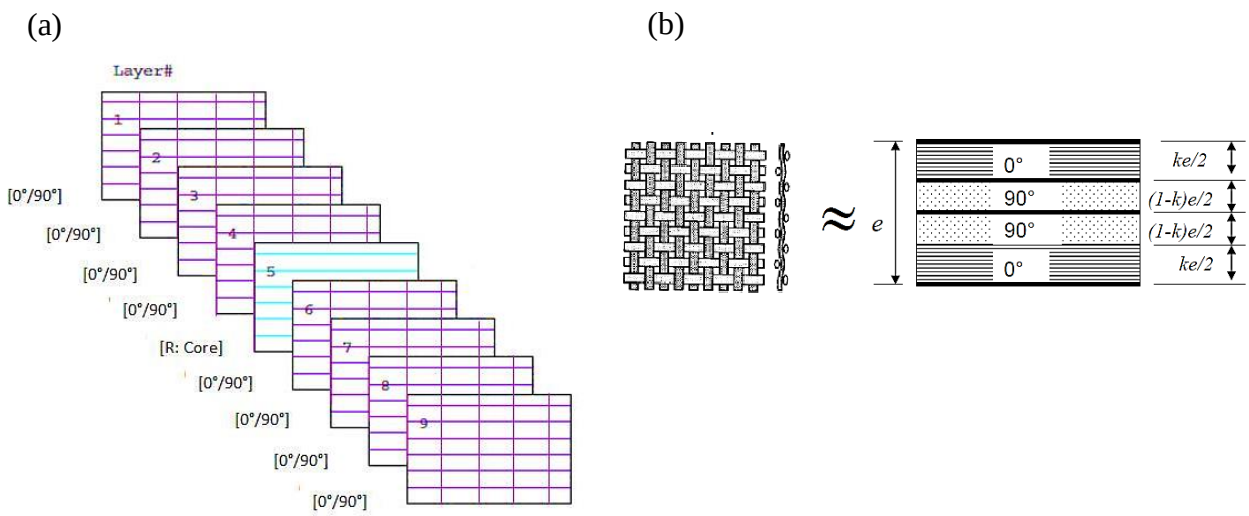

Figure 4-1: (a) The arranged layers of the sandwich panel model. (b) the woven fabric equivalent ply thickness

$$k = \frac{N_{warp}}{N_{warp} + N_{fill}} \qquad (4\text{-}1)$$

where

e: ply thickness

k: coefficient of equilibrium

N_{warp}: fiber count per inch in the warp direction

N_{fill}: fiber count per inch in the fill direction

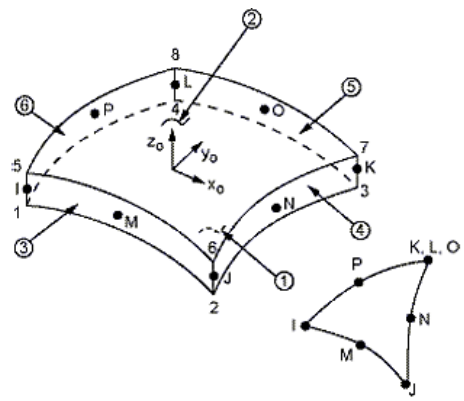

Figure 4-2: Shell 281 geometry ("ANSYS V13.0 User Manual ")

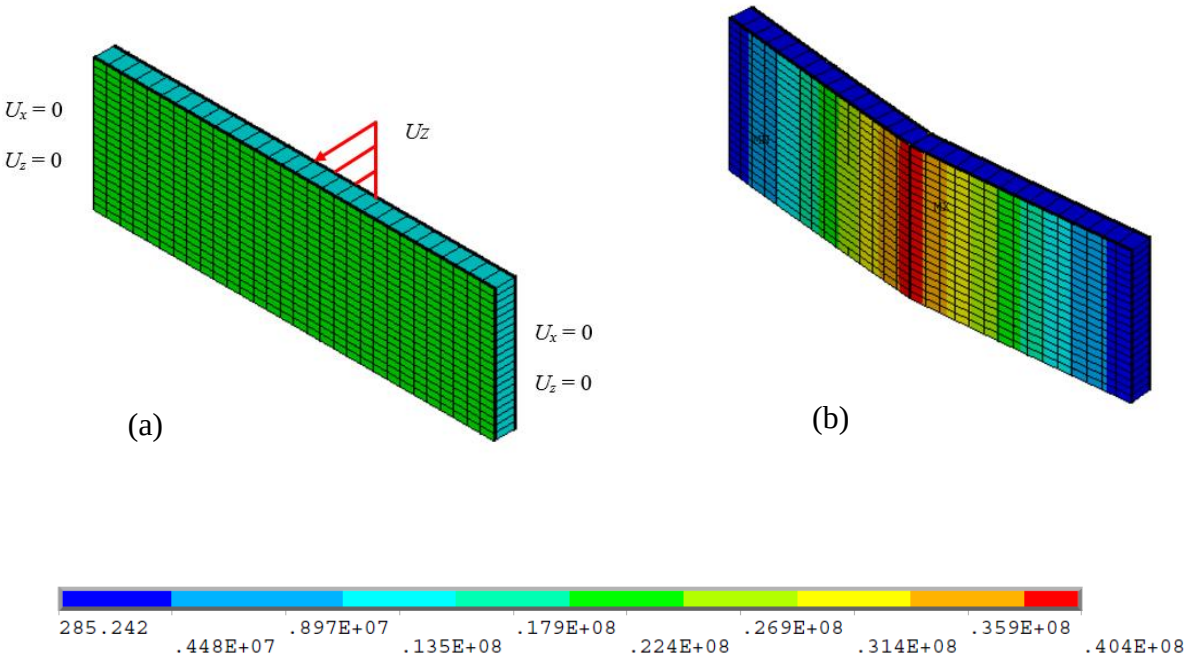

Figure 4-3: (a) The 3-point bending models with the applied load and boundary conditions. (b) Von-mises stress distribution

4.1.1 Materials Properties

The mechanical elastic planar properties of the woven carbon and glass composites used in this study were quoted from standard statistical experimental tests published in a handbook by the U.S. Department of Defense. This handbook was developed as a joint venture between the Department of Defense and the FDA and was published as guidelines for military and commercial products by establishing valid reference design values for certification and vendors. Thus, the obtained statistical standard results had a good level of reliability for the current numerical analysis. This high level of reliability was due to the use of commonly used modern materials with newly established test standards such as the compression test standard ASTM D695 Boeing modified. All statistical parameters such as the mean, maximum, minimum and CV values were calculated for each material property (see Appendix A). Hence, it was better to use the mean values as the elastic properties for the carbon and glass composites used in this study. In addition to the core properties, the values of the elastic properties for the plain woven carbon and 8-harness satin glass composites are listed in Table 4-1. For hybrid laminates, the properties were calculated using the classical laminate plate theory CLPT using ANSYS Mechanical APDL V13.0. For each hybrid lamina, the stacking sequences of the carbon and glass layers generated the properties of the six hybrid configurations according to the following equations obtained from several loads applied to the lamina shown in Figure 4-4:

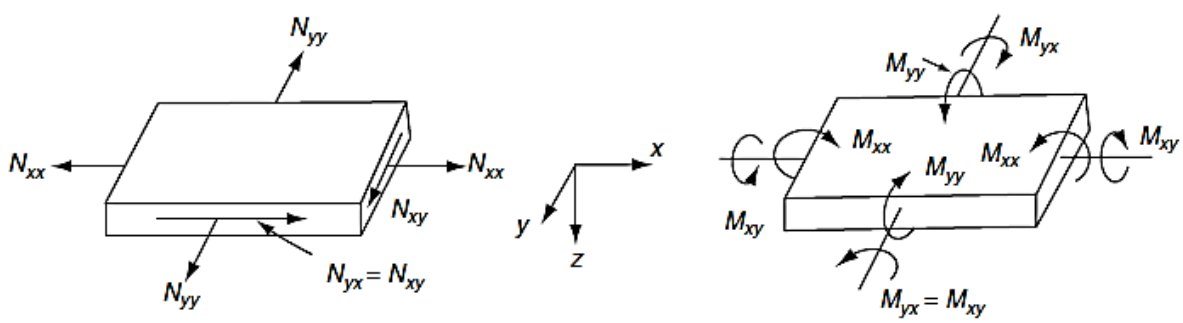

Figure 4-4: Normal, bending and twisting loads applied on a lamina (Mallick, 2007)

$$\begin{bmatrix} N_{xx} \\ N_{yy} \\ N_{xy} \end{bmatrix} = [A] \begin{bmatrix} \varepsilon^{\circ}_{xx} \\ \varepsilon^{\circ}_{yy} \\ \gamma^{\circ}_{xy} \end{bmatrix} + [B] \begin{bmatrix} k_{xx} \\ k_{yy} \\ k_{xy} \end{bmatrix}$$

$$\begin{bmatrix} M_{xx} \\ M_{yy} \\ M_{xy} \end{bmatrix} = [B] \begin{bmatrix} \varepsilon^{\circ}_{xx} \\ \varepsilon^{\circ}_{yy} \\ \gamma^{\circ}_{xy} \end{bmatrix} + [D] \begin{bmatrix} k_{xx} \\ k_{yy} \\ k_{xy} \end{bmatrix}$$

where [*A*], [*B*] and [*D*] represents the extensional, coupling and bending stiffness matrices for the laminate.

$$[A] = \begin{bmatrix} A_{11} & A_{12} & A_{16} \\ A_{12} & A_{22} & A_{26} \\ A_{16} & A_{26} & A_{66} \end{bmatrix}$$

$$[B] = \begin{bmatrix} B_{11} & B_{12} & B_{16} \\ B_{12} & B_{22} & B_{26} \\ B_{16} & B_{26} & B_{66} \end{bmatrix}$$

$$[D] = \begin{bmatrix} D_{11} & D_{12} & D_{16} \\ D_{12} & D_{22} & D_{26} \\ D_{16} & D_{26} & D_{66} \end{bmatrix}$$

The elements of the stiffness matrices can be calculated from the following equations:

$$A_{mn} = \sum_{j=1}^{N} (\bar{Q}_{mn})_j (h_j - h_{j-1}),$$

$$B_{mn} = \frac{1}{2} \sum_{j=1}^{N} (\bar{Q}_{mn})_j \left(h_j^2 - h_{j-1}^2\right),$$

$$D_{mn} = \frac{1}{3} \sum_{j=1}^{N} (\bar{Q}_{mn})_j \left(h_j^3 - h_{j-1}^3\right),$$

The laminate properties are calculated by substituting A_{mm}, B_{mm} and D_{mm} into [A], [B] and [D], respectively; after solving the equations, the laminate mechanical properties are calculated using the following equations:

$$Nx = h\,\sigma_{xx}$$

$$Ex = \frac{\sigma_{xx}}{\overset{\circ}{\varepsilon}_{xx}}$$

$$Ey = \frac{\sigma_{yy}}{\overset{\circ}{\varepsilon}_{yy}}$$

$$\gamma_{xy} = \frac{\overset{\circ}{\varepsilon}_{yy}}{\overset{\circ}{\varepsilon}_{xx}}$$

$$G_{xy} = \frac{A_{66}}{h}$$

Table 4-1 shows similarities in the longitudinal, transverse and shear mechanical properties of the hybrid face sheets in H1 and H6, in H2 and H5, and in H3 and H4. This similarity corresponds to the similarity in the [A], [B] and [D] face sheet matrices. However, the flexural rigidity E_{fr} values do not show this pattern of similarities. Therefore, a numerical hybrid effect for this model with hybrid face sheets could provide an apparent hybrid effect. The values of the out-of-plane modulus

were obtained from the model developed by (Naik, 1994), which he used to calculate E_z for various composite fabrics dependent on the fabric geometry; the calculated modulus E_z for the fabrics were taken from (Chretien, 2002). As there are no available data for hybrid composite properties, some property values were assumed and averaged to simulate numerical analysis. In specimen S8 and all of the hybrid specimens, the shear moduli G_{xz} and G_{yz} were assumed to be equal to G_{xy}. In the hybrids, the Poisson's ratios v_{xz} and v_{yz} were also assumed to be equal to the value of the calculated v_{xy}. Finally, the E_z values for the hybrids were assumed to be the average between the glass fibers and carbon fibers as the hybrid lamina contained equal contents of glass and carbon fibers.

Table 4-1: Material properties of the sandwich model face sheets

	Ex, GPa	**Ey, GPa**	**Ez, GPa**	**Gxy, GPa**	**Gxz = Gyz, GPa**	**vxy**	**vxz = vyz**
GGGG	26.5	25.0	8.5	6.5	4.2	0.10	0.28
GGCC	35.9	34.7	10.2	4.1	4.1	0.26	0.26
GCGC	38.1	37.2	10.2	4.1	4.1	0.25	0.25
GCCG	38.8	38.1	10.2	4.1	4.1	0.24	0.24
CGGC	38.8	38.1	10.2	4.1	4.1	0.24	0.24
CGCG	38.1	37.2	10.2	4.1	4.1	0.25	0.25
CCGG	35.9	34.7	10.2	4.1	4.1	0.26	0.26
CCCC	50.8	50.8	12.0	3.86	3.86	0.03	0.45

4.1.2 Flexural 3-Point Bending Model Results

The results of each sandwich panel were obtained at four incremental points of the central displacement, including the yield and ultimate displacement points extracted from the experimental data. The numerical results demonstrated a linear and proportional relationship between the specimens' middle displacement (deflection) and the calculated von Mises stresses. Figure 4-5 graphically illustrates the correlation between the numerical results and the experimental results as well as their linear agreement until reaching the deflection yield point. This level of linear agreement between the numerical and experimental results indicates the validity of the material properties listed in Table 4-1 for this model. Hence, this model can predict the linear behavior of sandwich specimens under ASTM C393/C393M-11 testing conditions.

After yielding, the experimental test specimens started to fail non-linearly by suffering from the generated shear deformation between the weak core and the face sheets. However, this level of non-linear failure is beyond the scope of this study as it needs to be studied using progressive failure analysis. Thus, the numerical model here was constructed to solve the model linearly only and to validate the material properties used.

The von Mises stress distribution across each layer including the core were also obtained at deflection points that represent the experimental yield and ultimate deflection points for each test specimen, as noted in Table 3-3 in Chapter 3. In Figure 4-6, the stress distribution in each face sheet layer shows a highly stressed zone located where the applied load is exerted, while the constrained (simply supported) short edges show the least stress. The von Mises stress distribution at the core reveals a highly stressed oval-shaped area located at the center. The stressed oval shape is considerably stressed along the oval shape height that is aligned with where the load is applied. This stressed area might suggest the location of the initial failure of the face-core debonding and the later final crushing failure area resulting from the load continuing beyond the sandwich panels' ultimate strength. It has been shown that the maximum and minimum stress values were delivered by the upper top and lower bottom layers (L1 and L8). By moving across the model's thickness, the stress values showed a slight, linear and gradual decrease starting from L2 up to L4. A huge decrease in the stress value was shown at the core's top edge and continued to zero at the model centerline. After passing the centerline, the stresses return to the same values in L5, L6, L7 and L8 but with the opposite sign (see Appendix B). The numerically calculated von Mises stresses for all the sandwich panels resembled the usual stress distribution of an ideal 3-point flexural test across the panel thickness. However, this numerical stress-deflection relationship does not indicate the panels' yielding points as in the experimental results, where the stress yield and ultimate points are visually clear. There are two methods used to relate numerical results to experimental results: taking the numerical stress readings at deflection points similar to the experimental deflection values or taking the numerical deflection readings at stresses similar to the experimental values. Here, it is quite practical to implement the first method to calculate the numerical yielding loads from the stresses using equation 3-1 by taking the stress readings at the deflection points that are similar to the experimental deflection values. As a result, a relationship between the numerical and the experimental yielding and ultimate points can be achieved. Table 4-2 lists the numerical results

with their related experimental results from Section 3.5.2 in Chapter 3. While the numerical results represent a linear proportional relation between the load/stress and deflection, the numerical deflection yielding points were chosen to match the experimental deflection yielding points. On the other hand, the experimental ultimate load/stress at core shear failure happened at the core's ultimate shear strength (0.6 MPa), as shown in Table 3-3 in Section 3.5.2. The tested sandwich panels ultimately all failed near the core's ultimate strength, which was within the expected behavior of such sandwich panels under ASTM C393/C393M-11. This mode of failure satisfies the accepted failure mode specified in the ASTM C393/C393M-11 testing procedure and the specimens' accepted failure mode. Thus, the experimental ultimate deflection was used in the numerical model as the deflection point to obtain the numerical ultimate load/stress.

Table 4-2: Experimental and numerical results of the flexural 3-point bending tests

	Experimental Results				**Numerical Results**	
	w_{yld}, **mm (CV)**	w_{ult}, **mm (CV)**	σ_{yld}, **MPa (CV)**	σ_{ult}, **MPa (CV)**	σ_{yld}, **MPa**	σ_{ult}, **MPa**
S1	2.87 (±0.02)	4.12 (±0.02)	39.7 (±0.01)	50.0 (±1.10)	39.9	57
H1	2.80 (±0.01)	4.0 (±0.001)	40.5 (±2.28)	50.0 (±2.16)	38.1	61
H2	2.84 (±0.01)	3.50 (±0.01)	41.0 (±1.13)	47.0 (±1.07)	40.1	61.6
H3	2.83 (±0.02)	4.18 (±0.02)	39.4 (±2.49)	49.0 (±0.58)	43.3	61.8
H4	2.87 (±0.01)	4.19 (±0.02)	39.4 (±0.88)	50.0 (±0.58)	43.3	61.8
H5	2.61 (±0.01)	3.99 (±0.05)	36.5 (±1.04)	48.3 (±1.56)	40.1	61.6
H6	2.87 (±0.02)	4.12 (±0.02)	37.8 (±1.46)	45.0 (±0.00)	38.1	61
S8	2.87 (±0.02)	4.12 (±0.02)	40.8 (±0.00)	53.0 (±0.56)	40.4	64.6

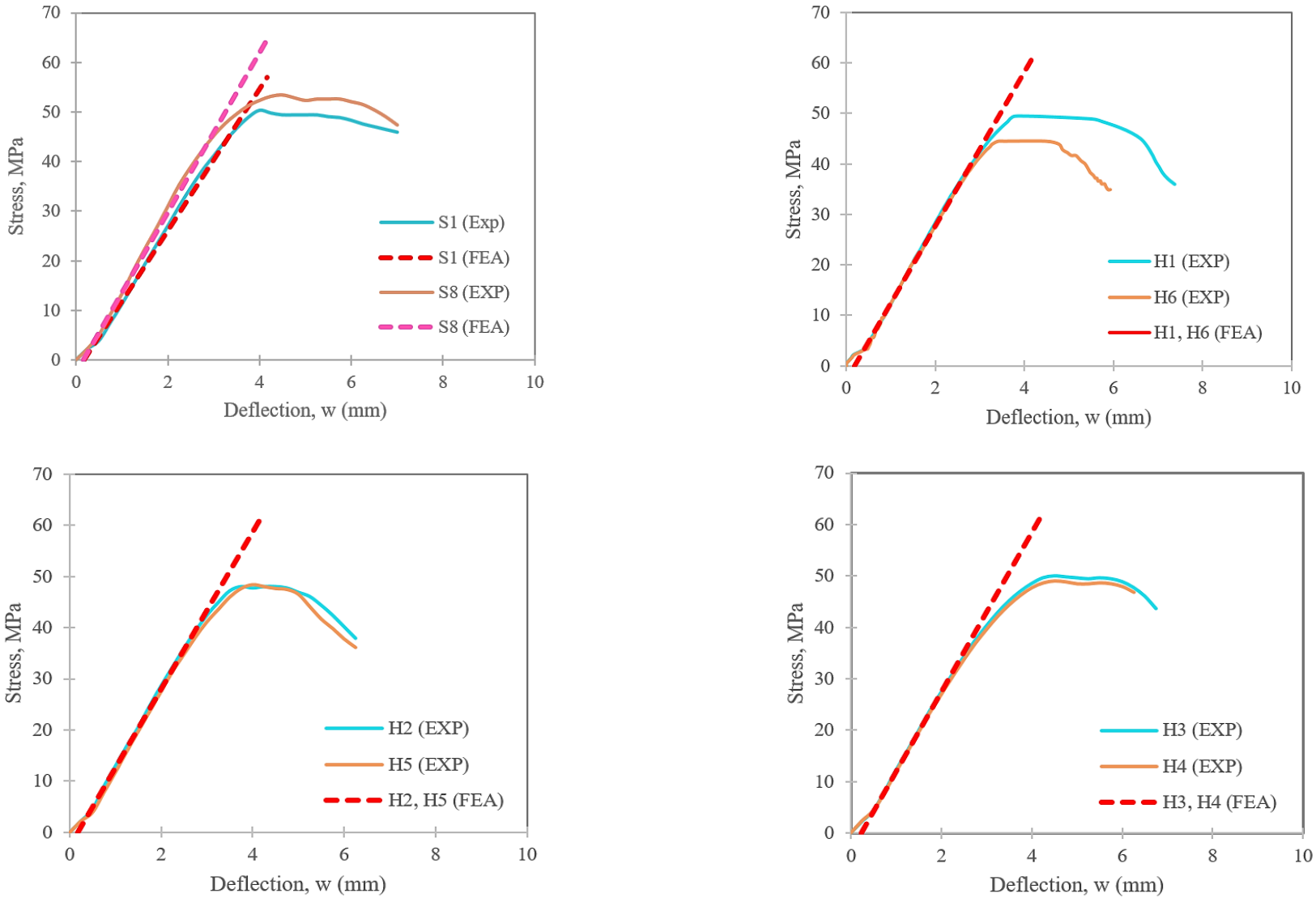

Figure 4-5: The Von-mises stress vs. deflection of the numerical and experimental results of all the tested sandwich panels

In general, the numerical stress distribution across the model's thickness for all the sandwich panels at the experimental yield and ultimate deflection points are illustrated in Figures 4-7 and 4-8. Figure 4-7 shows that specimens S1, H2, H5 and S8 reached their yielding stress at the same value. Hybrids H1 and H6 yielded at a lower stress value than S1, H2, H5 and S8. In contrast, hybrids H3 and H4 reached their yield stress at a higher level than the other sandwich panels. Figure 4-8 shows that the ultimate stress distribution across the model thickness predicted approximately equal ultimate stresses for all the hybrid panels. The smallest ultimate stress was achieved by S1, while S8 performed the best by failing at the highest ultimate stress value.

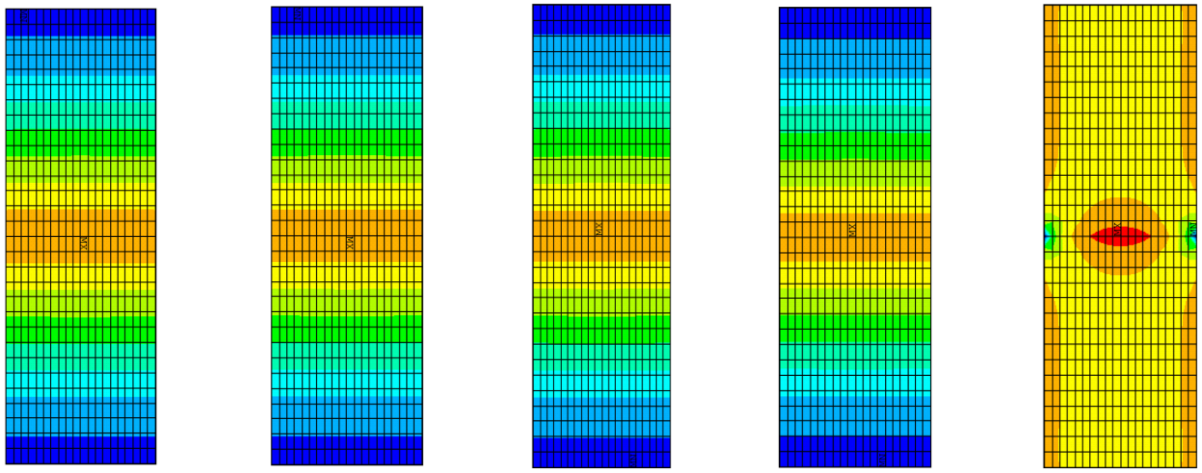

L1 & L8 L2 & L7 L3 & L6 L4 & L5 Core

Figure 4-6: Von-Mises stress distribution for each layer within the sandwich panel numerical model

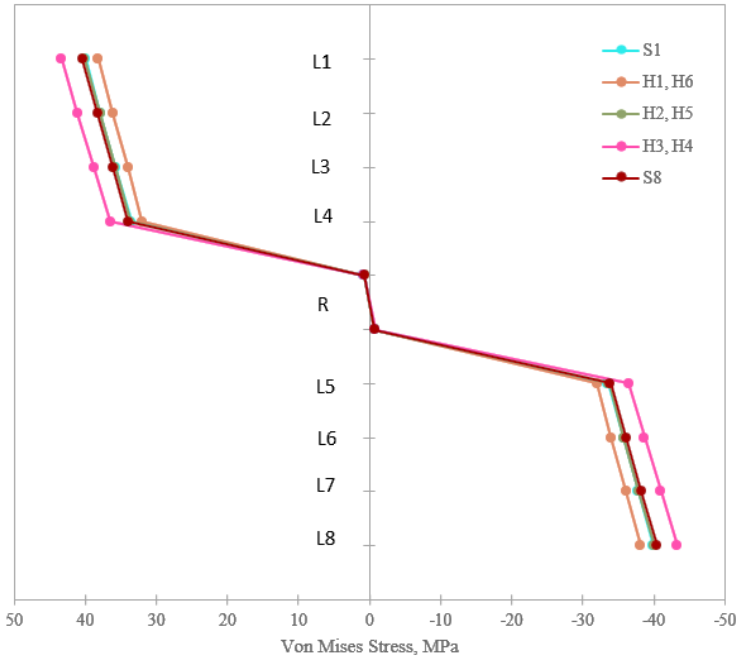

Figure 4-7: Von-mises yield stress distribution across the model thickness

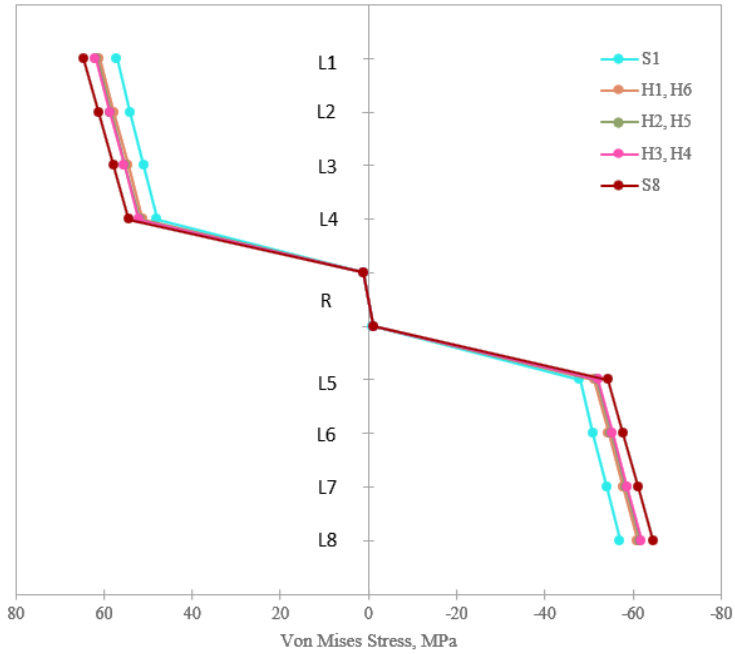

Figure 4-8: Von-mises ultimate stress distribution across the model thickness

From another prospective, the yield and ultimate loads can be reviewed by analyzing the relationship between the numerical and experimental results. This analysis starts with calculating the numerical P_{yld} from the numerical stress σ_{yld} from equation 3-1. Table 4-2 shows that P_{yld} for both S1 and S8 were similar to the experimental results. For H1, the experimental results showed a 3.6% higher yielding load at the same deflection point, which might be considered a positive hybrid effect, while H6 delivered a yield load that was approximately equal to the experimental result. In contrast, the numerical result for hybrid H2 was equal to the experimental result, while hybrid H5 provided 9.5% less yielding capacity for the numerical value, which can be considered a negative hybrid effect. Hybrids H3 and H4 yielded at the same loading level but was 11.2% less than the numerical result, which can also be considered a negative hybrid effect. Further discussion on the numerical and experimental results can be found in Chapter 5.

4.2 Non-linear buckling model

The buckling behavior of the sandwich panels with composites face sheets and a rigid foam core were simulated. The model was constructed as a 2D sandwich panel with two similar orthotropic face sheets bonded to an isotropic core with the properties listed in Table 4-3. The model dimensions were 50 x 406 mm (2 x 16 in) with a core thickness of 6.66 mm and a face sheet thickness of 9×10^{-4} mm, as shown in Figure 4-9. Figure 4-9 shows that the model's boundary conditions were set to fix the bottom short horizontal edge ($U_x = U_y = U_z = R_x = R_y = Rz = 0$) and to similarly fix the opposite top edge except in the U_x (loading) direction. The vertical long edges were not supported. The element used was SHELL 281 (Manual) with 8 nodes and six degrees of freedom at each node, as shown in Figure 4-2. This type of quadratic element is suitable for non-linear analysis due to its ability to change thickness. The model's complete shape is shown in Figure 4-10 (a).

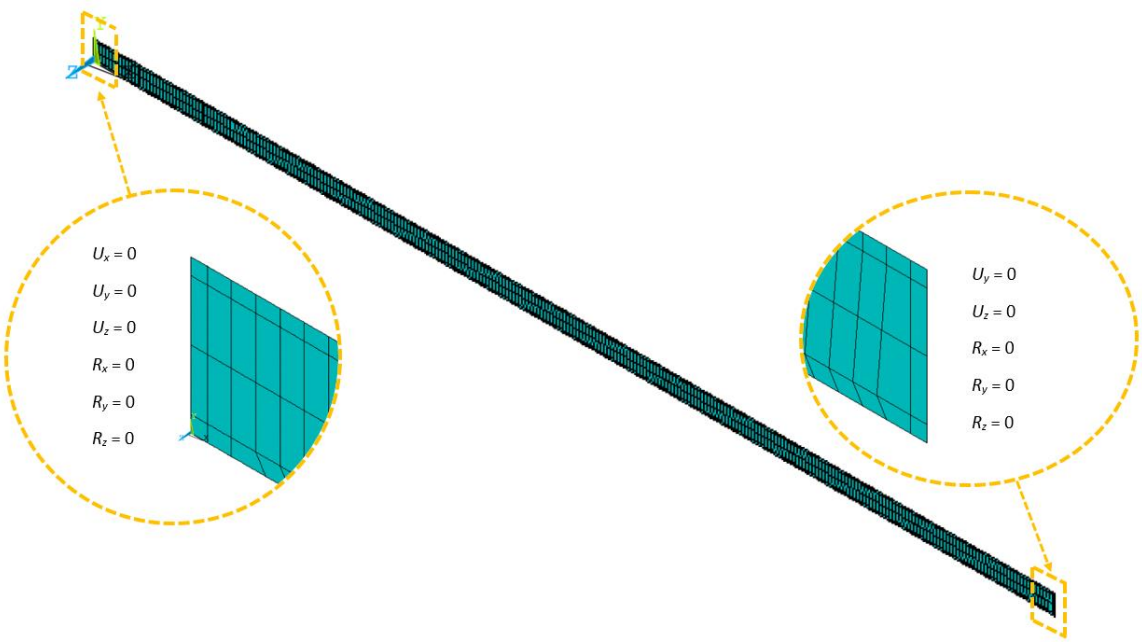

Figure 4-9: The FEA 2D buckling model

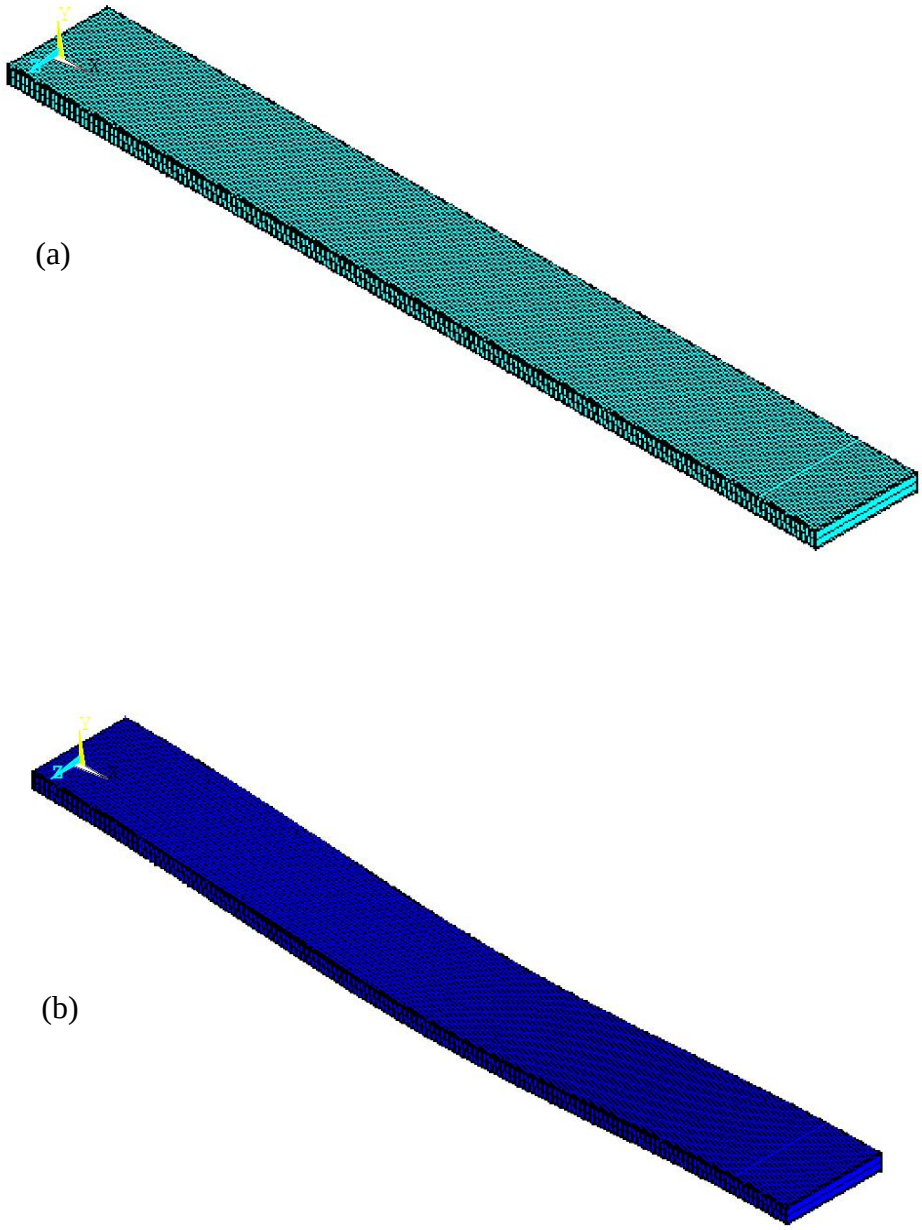

Figure 4-10: The model on disply element view, (a) The model after meshing and applying boundary conditions, (b) the models first buckling mode shape

As recommended by the ANSYS developers, a small force F_i was applied at a node located at the middle surface of one of the face sheets. This small force excited the buckling initiation for non-linear buckling analysis and was tested at different values starting from 5 N until the model showed monitored buckling behavior. This small force was also varied depending on the face sheet properties, especially stiffness. In Table 4-3, the initiation force needed to excite the sandwich panel with all-glass face sheets was 120 N; the highly stiffened all-carbon sandwich panel needed only 20 N, and the hybrids buckled at 80 N. The experimental controlled displacement procedure was simulated by applying a uniformed nodal displacement (U_x = 1.5 mm) at the nodes located at the top horizontal short edge. The model solution was performed through a non-linear built-in solver using the Newton-Raphson method for all the nodes. In effect, a non-linear analysis was used to solve the model by simulating the non-linear buckling behavior to obtain P_{cr} from the applied incremental load steps against the out-of-plane deflection at the middle of the face sheet. This middle point was used to simulate the experimental readings recorded by the non-contact laser sensors that measured the out-of-plane deflection. However, the FE model provides only one out-of-plane deflection result. Thus, the positive out-of-plane deflection was compared to the positive experimental readings.

Table 4-3: FE model materials properties

	E_x, GPa	E_y, GPa	E_z, GPa	G_{xy}, GPs	$G_{xz} = G_{yz}$, GPa	ν_{xy}	$\nu_{xz} = \nu_{yz}$	F_i, N
GGGG	26.5	25.0	8.5	6.5	4.2	0.10	0.28	120
GGCC	35.9	34.7	10.2	4.1	4.1	0.26	0.26	80
GCGC	38.1	37.2	10.2	4.1	4.1	0.25	0.25	80
GCCG	38.8	38.1	10.2	4.1	4.1	0.24	0.24	80
CGGC	38.8	38.1	10.2	4.1	4.1	0.24	0.24	80
CGCG	38.1	37.2	10.2	4.1	4.1	0.25	0.25	80
CCGG	35.9	34.7	10.2	4.1	4.1	0.26	0.26	80
CCCC	50.8	50.8	12.0	3.86	3.86	0.03	0.45	20

The non-linear model was used to analyze the static large displacements and to write the nodal and elemental results for each sub-step. The number of sub-steps was chosen to control the solver

output results instead of the time increment control option, which provides a program's chosen number of outputs that might be inconvenient for the user. Therefore, a total number of 20 output results were obtained by setting the sub-step number to 50, bounded by a maximum and minimum number of sub-steps of 1000 and 1, respectively. The historical incremental nodal reaction forces at the fixed bottom edge were plotted against the incremental out-of-plane nodal transition at the middle point. This reaction force node was selected because it had the highest loading readings among the other nodes located at the fixed edge. An example of the output results from the FEA model of the reaction force compared to the middle point out-of-plane deflection is illustrated in Figure 4-11. In a similar manner, the numerically obtained force vs. out-of-plane deflection had the same transition zone after the linear zone as the experimental curves. Hence, the numerical P_{cr} did not exist as a bifurcation point; instead, P_{cr} represents the starting point of the transition zone. Therefore, P_{cr} was extracted from the load-step increment results of the reaction force where the solver tended to bisect the load-step increment by trying a new solution at a smaller load (Manual). This numerical approach for extracting P_{cr} agrees with the conservative extraction implemented in this study.

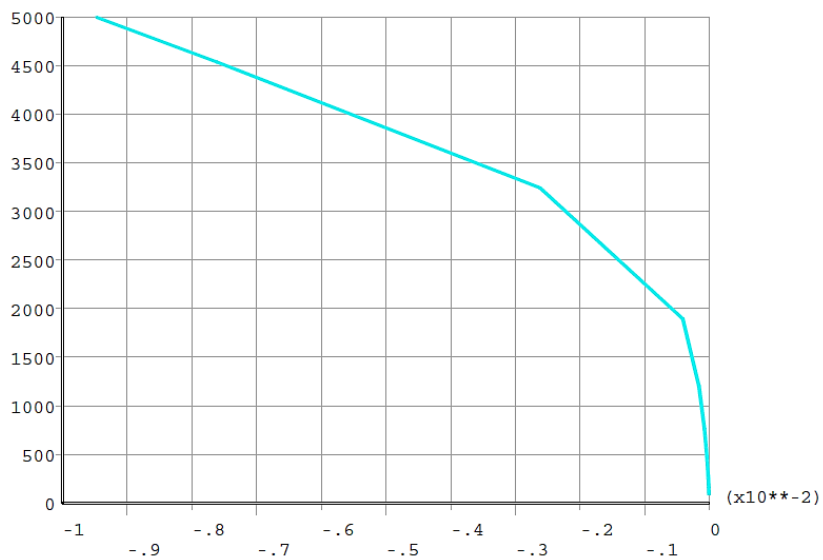

Figure 4-11: Newton-Raphson non-linear curve results

4.3 Non-Linear Stabilization

Non-linear stabilization is defined as "*A tool for dealing with local instabilities as well as global instability*" (Manual). This tool is useful for unstable slender structures when they reach their buckling load during the execution of the non-linear analysis solver. For unstable structures with large nodal displacement caused by small load increments, the use of non-linear stabilization is usually beneficial. Non-linear stabilization adds an artificial damper to each node and forms an artificial element created from the artificial damper node fixed to the ground and the node originally created by the FE model. The damping force is calculated by the program in proportion to the relative pseudo velocity of both the artificial and FE model nodes. This velocity is calculated as an incremental displacement divided by the sub-step time increment. Thus, to accomplish stabilization, the stabilization force reduces the unstable large displacement increment at any degree of freedom (DOF) by applying a sufficiently large damping force. The applied stabilization force can be set as either a constant stabilization force or a reduced stabilization force. The constant stabilization force option maintains a constant damping factor during analysis, while the reduced stabilization force option linearly decreases the damping factor to zero upon analysis completion. In each previous stabilization force option, there are two methods used to control the stabilization factor: entering an energy dissipation ratio or entering a damping factor. The energy dissipation ratio "*is the ratio of the work done by the stabilization force to the element potential energy*" (Manual) and it commonly ranges between 0 and 1. The program uses the damping factor to calculate the stabilization force for all subsequent sub-steps. Furthermore, the damping factor depends on many aspects such as the element's shape and size, the load step size and time. Therefore, the damping factor differs from one element to another.

4.3.1 Modified Model with Non-Linear Stabilization

In general, all the numerical curves plotted in Figures 4-12 and 4-13 agree with the experimental out-of-plane deflection results within Zone 1 until they reach P_{cr}. After that, the numerical results tend to diverge from the experimental results as the load decreases until failure. This post-buckling level of loading (Zone 2) can be accurately studied by implementing a progressive failure code to the ANSYS solver, which is beyond the scope of this study. However, this post-buckling zone can

be altered by applying the non-linear stabilization option to the Newton-Raphson method to closely match the experimental post-buckling zones, especially for H2, H3, H4 and H5. The applied non-linear stabilization constant force option was chosen to be controlled by applying an energy dissipation ratio ranging between 0 and 1. Indeed, the greater the value of the energy dissipation ratio is, the stiffer the response resulting from the system. As a result, the post-buckling part of the numerical curves in Figure 4-14 and 4-15 were adjusted to approximately match the experimental post-buckling curves of H2 and H5 using a dissipation ratio of 0.05 by using the modified Finite Element (MFEA) model.

4.4 Results and Discussion

The modeled sandwich panel exhibited global buckling failure, as shown in Figure 4-10 (b). Unlike composites panels that deliver more than one buckling mode shape, normal sandwich panels exhibit only one buckling mode shape correlated to the core shear deformation failure. Thus, the simulated numerical global buckling agrees with the experimental global buckling that occurred in the test specimens within Zone 1. Therefore, the recorded out-of-plane readings gathered from the non-contact laser sensors can be compared to the historical nodal displacement results for the middle surface point. In addition, the P_{cr} extracted from the numerical results also theoretically followed the method used in to extract P_{cr} from the experimental results, as discussed in Section 3.7.1. However, the numerical P_{cr} values were extracted from the incremental load step data generated by the Newton-Raphson solver at the load step when the load starts to gradually increase before it continues to rapidly and incrementally diverge. This incremental load step data can be gathered from the saved results calculated for each incremental load step by the FE solver under the TimeHistPostpro command. Figures 4-12, 4-13, 4-14 and 4-15 display the corresponding behaviors of both the experimental and numerical results. Table 4-4 shows the P_{cr} results obtained from the numerical model along with the experimental results. However, to obtain a numerical buckling behavior curve similar to the experimental curve, it is recommended to apply progressive failure analysis to the FEA model.

Table 4-4: Numerical and experimental P_{cr} results

Sandwich Panel		P_{cr} (FEA), N	P_{cr} (EXP), N	Diff%
S1	**GGGG/R/GGGG**	1,612	1,545	4.2
H1	**GGCC/R/CCGG**	2,090	1,927	7.8
H2	**GCGC/R/CGCG**	2,228	2,360	5.9
H3	**GCCG/R/GCCG**	2,274	2,024	10.9
H4	**CGGC/R/CGGC**	2,274	2,090	8.1
H5	**CGCG/R/GCGC**	2,228	2,033	8.8
H6	**CCGG/R/GGCC**	2,090	1,961	6.2
S8	**CCCC/R/CCCC**	2,638	2,584	2.0

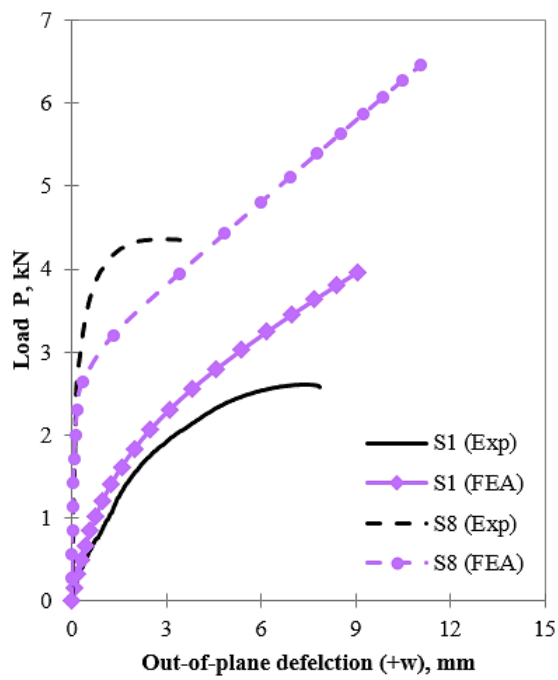

Figure 4-12: Experimental and FEA load vs. out-of-plane deflection for S1 and S8

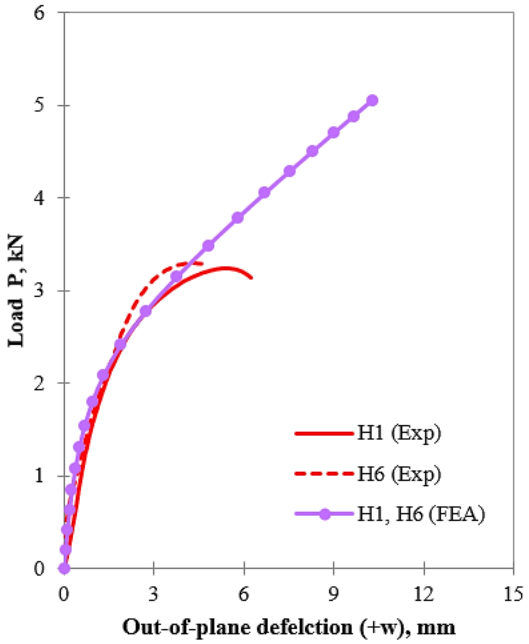

Figure 4-13: Experimental and FEA load vs. out-of-plane deflection for H1 and H6

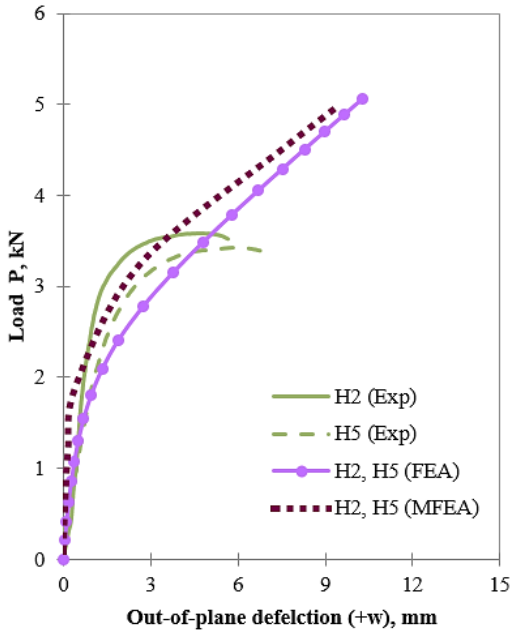

Figure 4-14: Experimental, FEA and MFEA load vs. out-of-plane deflection for H2 and H5

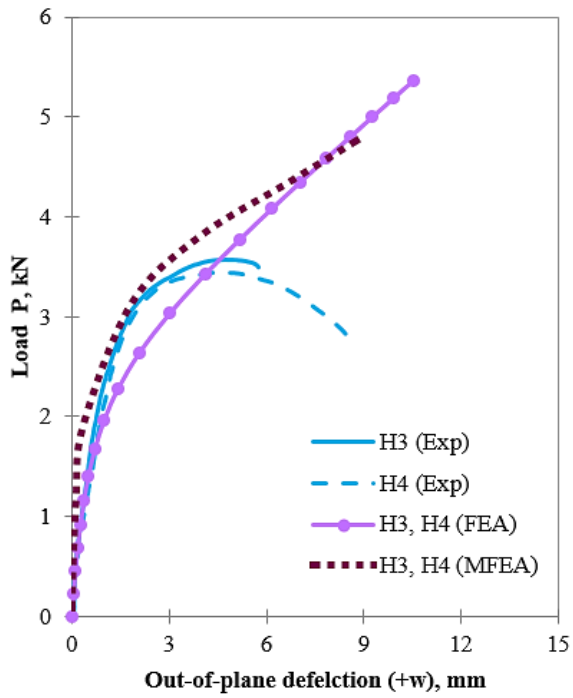

Figure 4-15: Experimental, FEA and MFEA load vs. out-of-plane deflection for H3 and H4

CHAPTER 5 ANALYTICAL, EXPERIMENTAL AND NUMERICAL RESULTS

5.1 Flexural 3-Point Bending Results

The ASTM C393/C393M-11 testing procedure was designed to practically determine the core shear properties of a sandwich panel. However, the experimental test results here showed a clear contribution of the stacking sequence of carbon and glass fiber layers in the face sheets on the sandwich panel performance during flexural testing. This contribution improved the panels' ability to resist the applied load by delaying the panels' yielding and ultimate load limits. Conversely, some panels performed worse than hypothetically expected, yielding and ultimately failing earlier. The most commonly used definition of the hybrid effect is not applicable in this case due to the lack of a theoretical failure prediction for sandwich panels under flexural loading other than the CLPT theory, which does not include the effect of shear deformation. However, by examining the experimental results, some hybrids performed better than the others even with less flexural rigidity. Moreover, the specimens that placed the carbon fiber layers at the outer side of the panels tended to fail earlier than the panels with the glass fiber layers at the outer side of the face sheet lamina. This observation agrees with the conclusions obtained by the researchers mentioned earlier in Section 2.9.4.1; these studies stated that placing the glass fibers layers at the outer side improved the flexural performance of the lamina. In this study, the sandwich panels under flexural loading simultaneously provided two different and unequal flexural rigidities for each face sheet. However, the upper face sheet always delivered higher flexural rigidity than the lower face sheet, as mentioned in Section 3.7.2; the upper face sheet showed a higher tendency to be crushed under flexural loading due to the brittle nature of composites combined with the stress concentration at the contact area between the upper face sheet and the loading roller. This type of failure is one of the advantages of sandwich panels in terms of protecting the space behind the lower face sheet from failure or leakage. Additionally, the existence of the foam core may help to prevent any fluid, gas or thermal leakages; it can also absorb impact energy caused by static or projectile loading conditions.

From the experimental results, the hybrid specimens can be categorized into three groups depending on their yielding load levels. The first level contains hybrids H1 and H2 as they are approximately equal at 360 N and 365 N, respectively. The second group contains specimens with balanced face sheets, H3 and H4; these specimens also have equal yielding levels that are 10 N smaller than those of the first group. The last and the critically important group is the third group which consists of H5 and H6. Hybrid H5 yielded earlier than all the other hybrids at 330 N, which means that is has the worst stacking sequence. Similarly, hybrid H6 yielded less than the other hybrids but better than H5. In terms of the ultimate failure load levels, hybrids H2, H5 and H6 performed the worst and failed earlier than the other hybrids. The early failures of H5 and H6 can be explained by the carbon fiber layers located at the outer side of the face sheet lamina; however, this is not the case for H2. The unique performance of H2 in providing the best yielding load resistance accompanied with the second smallest ultimate failure load resistance is interesting. This change from the highest yielding load to the second lowest ultimate load shows a stiff performance, similar to the carbon fibers, which is not preferable in applications with flexural loading conditions. In contrast, hybrids H3 and H4 delivered a balanced and stable performance and resisted the deflection better than the other hybrids. Thus, it is recommended to use hybrids H3 and H4 in applications where flexural loading is critical.

The numerical model was mainly constructed to validate the material properties gathered from Appendix A for glass and carbon fiber fabrics and the calculated mechanical properties of the hybrids. The FEA model results agreed with the experimental results only in their linear part of the load/stress vs. deflection curves. The model was constructed to simulate the 3-point bending test linearly. The linear solution was stopped at a deflection value similar to the experimental deflection value where the core's shear stress was equal to the core's shear strength. However, the ultimate load values of the FEA model were much higher than the experimental results because of their locations at the non-linear parts of the experimental curves. Further implementation of progressive failure analysis could help to simulate the non-linear behavior of the flexural 3-point bending test.

5.2 ATFT and SDPT

The theoretical P_{cr} results calculated using both methods for each sandwich panel were plotted against the sandwich panels' configurations, as shown in Figure 5-1. The SDPT results started from the all-glass face sheet sandwich panel at 1,980 N and ended with the all-carbon face sheet sandwich panel at 3,003 N. In between, the calculated P_{cr} for the six hybrids showed a gradual increase in P_{cr} values from H1 to H6, ranging from 2,163 N to 2,865 N. Together with the reference panels, the values of the calculated P_{cr} values showed a progressive linear increase. On the other hand, the Allen Thick results delivered P_{cr} results that differed from the SDPT results due to the addition of the separately calculated face sheet buckling load in the final P_{cr} equation (see equation 2-8).

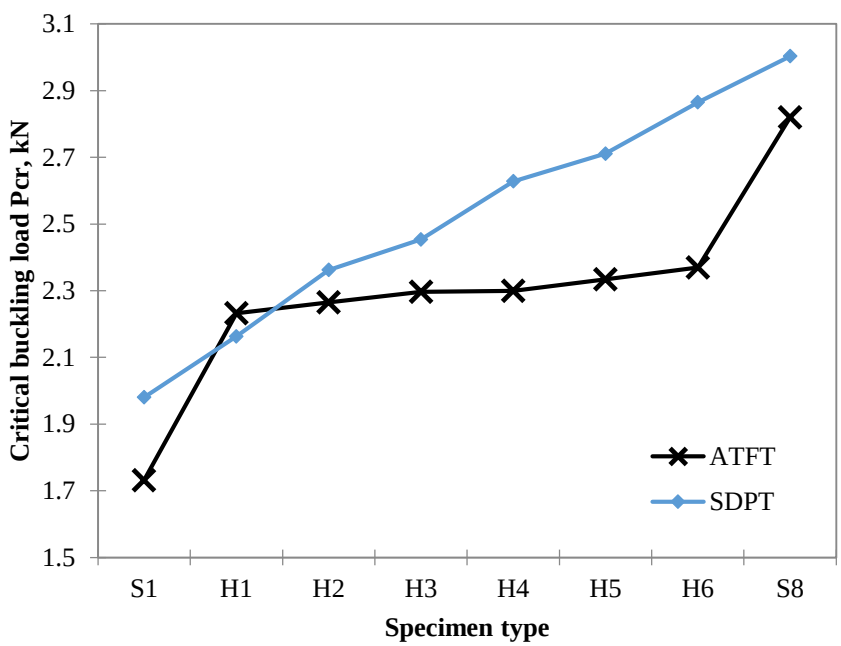

Figure 5-1: ATFT analytical prediction compared to SDPT results

The all-glass face sheet sandwich panel buckled at 1,731 N, which was 12.6% less than the P_{cr} value from SDPT. In addition, the all-carbon sandwich panel was predicted to buckle 6.1% earlier

than the value calculated by SDPT. The P_{cr} for hybrid H1 showed a good improvement of 22.4% in P_{cr} compared to S1. Similar to SDPT, the predicted P_{cr} values for hybrids H1, H2, H3, H4, H5 and H6 showed a gradual linear increase in P_{cr} values, ranging from 2,232 N to 2,370 N. The P_{cr} values predicted from Allen Thick were less than the predicted values from SDPT except for H1. Hence, the Allen Thick predictions are more conservative than the SDPT predictions. Therefore, the Allen Thick predictions were selected for validating the numerical and experimental results. Moreover, several previously mentioned studies showed that the ATFT formulation provides very good buckling predictions that agree with the predictions obtained from very complicated formulations such as HSDT. Indeed, the good buckling predictions delivered by ATFT serves the objective of this study by validating the HE existence between the experimental and theoretical results.

5.3 The Analytical, Experimental and Numerical P_{cr}: A Comparison

A comprehensive comparison of the analytical, experimental and numerical critical buckling load was one of the main goals in this study. As previously shown in Chapter 3, the hybrid effect can only occur under a controlled experimental test environment. This is also true as shown in the studies previously mentioned in Chapter 2. Therefore, the analytical and numerical modeling validation using the investigated P_{cr} experimental results are plotted for all the sandwich panel specimens in Figures 5-2 and 5-3. The numerical modeling results were added to the previously mentioned analytical and experimental results in Chapters 2 and 4.

In general, the numerical predictions did not follow the progressively increasing pattern provided by the analytical predictions. In fact, the numerical predictions exhibited a buckling failure pattern close to the experimental results. This similarity might result from the difference in the coupling stiffness matrix [B] due to the different stacking sequences of the face sheet, which certainly result in different planar moduli (E_x and E_y). Among the hybrids, H3 and H4 had an equal superior planer moduli followed by hybrids H2 and H5 and then H1 and H6. These different planar moduli were clearly illustrated by the numerical results shown in Figure 5-3. The numerical results provided similar outputs for H1 and H6 as the face sheet properties were the same. The same concept applies

to H2 and H5 as well as H3 and H4. Hence, the numerical P_{cr} values start at a value of 1,612 N for the all-glass sandwich panel and increased to 2,090 N for H1 and then to 2,228 N and 2,274 for H2 and H3, respectively. Hybrids H3 and H4 delivered the highest P_{cr} values because of their similar and high longitudinal modulus E_x. After reaching the maximum values, the P_{cr} values for H5 and H6 continued to decrease to match the values of their mechanically corresponding specimens of H2 and H1, respectively. Finally, P_{cr} significantly increased to 2,638 N for the highly stiffened all-carbon face sheets in S8.

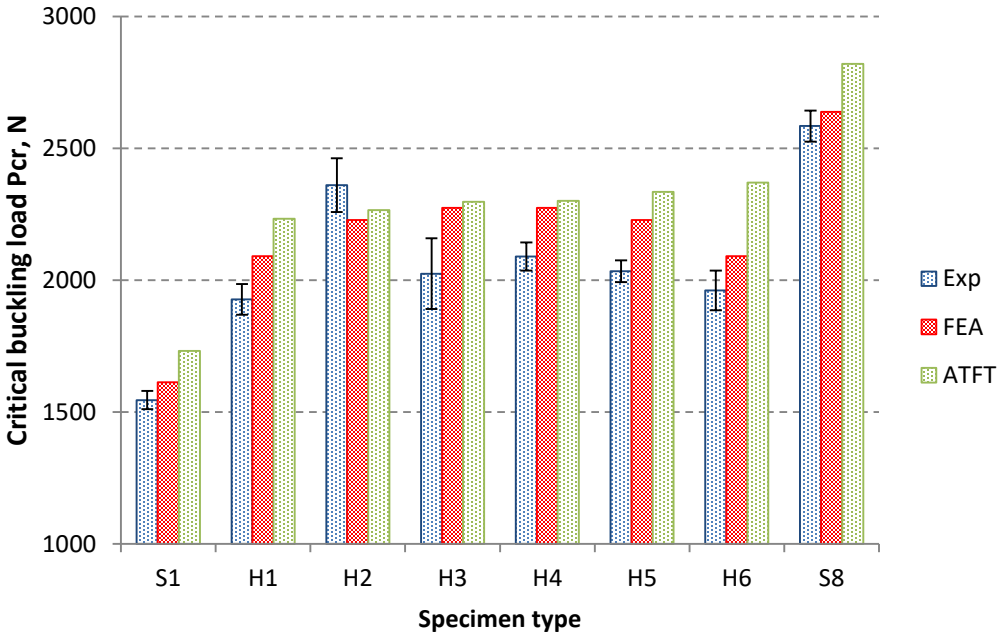

Figure 5-2: Comparison of the experimental, numerical and analytical P_{cr} results 1/2

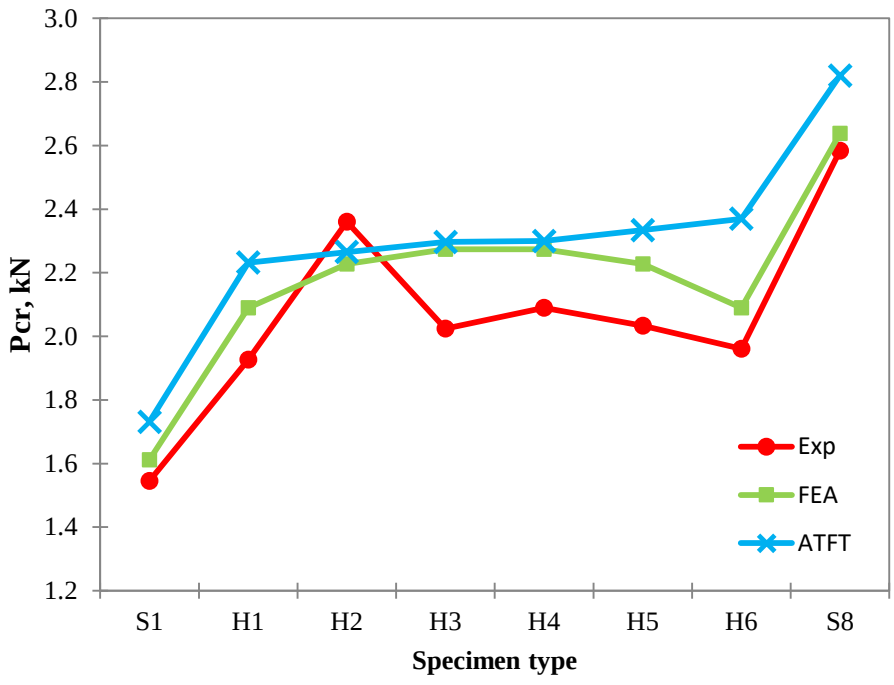

Figure 5-3: Comparison of the experimental, numerical and analytical P_{cr} results 2/2

The plotted experimental results in Figures 5-2 and 5-3 for all the specimens except for hybrid H2 showed a pattern similar to the FEA and ATFT results. In general, the experimental results for each specimen were less than the predicted results obtained from ATFT and FE analysis. This occurred for several reasons related to manufacturing quality, the specimens' geometric imperfections and the specimens' misalignment with the exerted experimental compressive load during the buckling tests. Starting from specimen S1, a 19.8% increase in P_{cr} was shown by adding two carbon fiber layers in each face sheet, as shown in H1. Although H1 and H2 had the same glass and carbon fiber contents, hybrid H2 had a higher longitudinal modulus and flexural rigidity and therefore had an 18.3% higher P_{cr} compared to H1. Unlike the other experimental results, the H2 experimental value of 2,360 N was 5.6% and 4.0% higher than its FE and ATFT predicted values, respectively. Moving to H3, an unexpected 14.2% decrease in P_{cr} was shown compared to the H2 P_{cr} value; the H3 longitudinal modulus and flexural rigidity were higher than those of H2. Hybrid H4 buckled later than H3 by only 3.1%, which is understandable due to their similar longitudinal modulus and the slightly higher flexural rigidity of H4. However, H3 and H4 provided less buckling resistance than

H2. As discussed in Section 3.7.4, in terms of the specimens' suggested failure mechanisms, the increasing flexural rigidity from H1 to H6 did not help hybrids H5 and H6 to perform better than H3 and H4. The lower longitudinal moduli of H5 and H6 compared to H3 and H4 dominated their buckling performance by causing them to buckle earlier than H3 and H4. Moreover, hybrid H5 was similar to H2 in terms of the longitudinal modulus but buckled less than H2. However, hybrids H3, H4, H5 and H6 had a failure pattern that matched the FE predicted failure pattern shown in Figure 5-3 as green line. Finally, specimen S8 buckled the least, as expected for a specimen made from carbon fiber face sheets; its P_{cr} was 2.4% and 8.4% smaller than the FE and ATFT predictions, respectively.

Figures 5-2 and 5-3 provide evidence of the hybrid effect, which is especially shown by the performance of H2 compared to the experimental, FE and ATFT results. The above results demonstrate the increases in buckling resistance achieved by changing only the stacking sequence of the same fibrous content within the specimen face sheets and its impact on designing high performance hybrid composites.

CHAPTER 6 CONCLUSION AND CONTRIBUTION TO KNOWLEDGE

The objective of this project was fully accomplished, and the project's research questions were answered. The hybrid effect of using glass and carbon fibers as face sheets attached to a rigid foam core has been thoroughly studied experimentally, analytically and numerically. The experimental part of the project started with the challenge of manufacturing several sandwich panels with an acceptable quality using local materials and tools available in the department's laboratory. The suggested double face infusion of resin during the VARTM technique produced very good quality test specimens that reflected very good experimental results. The second challenge was to design the test specimens to exhibit clear and measurable out-of-plane deflection. The process of testing specimens with different aspect ratios according to accepted standards was critical for studying many considerations before deciding on the final specimen dimensions. However, all test specimens showed clear and measurable buckling behavior before they failed due to core shear deformation. The non-contact laser sensors were a good addition for measuring the out-of-plane deflection, which is usually measured by deflectometers. The analytical predictions were also tested in comparison to the experimental results, and it was shown that both analytical methods provided different predictions; the ATFT method provided the closest predictions to the experimental results. The constructed FE model was also a challenge; the procedure of simulating the non-linear behavior of a sandwich panel with orthotropic face sheets and an isotropic core to not only extract the *Pcr* but to also simulate the out-of-plane deflection of the test specimen middle point was challenging. The FEA and MFEA results agreed with the experimental results with a minimal margin of deference. In addition, the increasing pattern of the *Pcr* values from S1 to S8 also agreed with the experimental results except for hybrid H2. A hybrid effect was clearly shown by incorporating carbon fibers and glass fibers, and the improvement in the buckling resistance was shown comparing the glass fibers and carbon fibers. Within the same assortment of stacking sequences with a 2:2 ratio of glass fibers to carbon fibers, there was also an observed hybrid effect. Hybrid H2 showed unexpected behavior as it buckled last compared to the other hybrids. Moreover, H2 behaved as a stiff panel more than H3, H4, H5 and H6, providing the smallest out-of-plane deflection among the hybrids. Therefore, hybrid H2 provides the best buckling resistance among

its follow hybrids. On the other hand, hybrid H4 demonstrated a balanced performance in terms of buckling resistance with the least CV. Structures with SHM systems benefit greatly from using hybrid sandwich panels as they have the advantage of strength (from carbon fibers) and "elasticity" (from glass fibers).

6.1 Contribution to the Knowledge

This research work has added significant contributions to the domains of manufacturing and the experimental mechanical behavior of hybrid composite sandwich structures. These contributions to knowledge are summarized in the following list:

1. The double face sheet infusion through VARTM is a simple and economical technique that can produce acceptable quality composite sandwich panels with a respectable volume fraction V_f ranging from 45% to 55%. Unlike the aeronautical industry that requires the higher volume fraction obtained using the expensive autoclave manufacturing technique, this level of volume fraction is acceptable in the civil and transportation industries.

2. The composite materials library of the experimental database is still incomplete, and more experimental studies are needed to better understand the complex mechanical performance of composite materials and their correlations to theoretical predictions. Therefore, this study aimed to experimentally fill the gaps in the composite material experimental database by performing flexural 3-point bending tests and buckling tests on composite sandwich panels with hybrid face sheets.

3. A novel hybridization arrangement within face sheet laminates were used to improve the critical buckling load P_{cr} of the tested sandwich panels compared to the sandwich panels made from all-glass fiber face sheets. This improvement ranged from 19.8% to 34.5%. On the other hand, the hybrid sandwich panels mitigated the catastrophic failure of all-carbon

fiber face sheet sandwich panels by 60%. Therefore, the use of hybrid composites can provide an improved composite structure without an excessive increase in cost. As shown in this study, the fixed and variable costs of fabricating hybrid sandwich panels with the 2:2 carbon and glass fiber content ratio were equal. However, the tested hybrid panels performed differently. The process of hybridization can control the measured and recorded experimental data such as the critical buckling load and the maximum out-of-plane deflection. Hence, composite structure designers can benefit from the results obtained by this study.

4. The complex nature of buckling (compression-bending) tests was studied along with the hybrid effect of the sandwich panel face sheets. The hybrid effect of buckling tests tended to imitate the hybrid effect of hybrid laminates under the compressive loading condition rather than the bending loading condition.

5. It has been physically and visually noticed that the chances of face sheet failure are higher when the carbon fiber layers are placed at or near the outer side of the face sheet lamina during bending tests. This was shown in all of the buckling tests except those for hybrid H2. Despite their theoretically high flexural rigidity, the hybrids with outer carbon fiber layers failed earlier due to their smaller damping ability and higher stress concentration zones.

6. A non-linear 2D FEA model was successfully developed and implemented in ANSYS APDL V13.0 to simulate the out-of-plane deflection results recorded by the non-contact laser sensors during experimental testing. The FEA model historical and incremental loads and the out-of-plane deflection outputs were in good agreement with the experimental results, validating the reliability of the FEA model.

6.2 Recommendations and Future Work

This study can be extended to cover other stacking sequences of glass and carbon layers with different fiber content ratios. A variety of core types can be also tested. The numerical model can also be extended by implementing progressive failure analysis to better understand and study the post-buckling region of the load vs. out-of-plane deflection and in-plane displacement. Additionally, the FE model could be extended with a dynamic failure analysis package to simulate the sandwich panel failure mechanism. Finally, this project aimed to fill a gap in the composite material library which still has the potential for further research opportunities.

BIBLIOGRAPHY

Allen, H. G. (1969). *Analysis and Design of Structural Sandwich Panels*: Pergamon Press, Oxford.

Ambartsumyan, S. A., Ashton, J. E. (1970). *THEORY OF ANISOTROPIC PLATES: STRENGTH, STABILITY, VIBRATION* (Vol. 11). Stamford, CT, U.S.A: Technomic Publishing Co., Inc.

ASTM. (2011). ASTM C393/C393M-11 Core Shear Properties of Sandwich Constructions by Beam Flexure.

Bažant, Z. P., & Beghini, A. (2004). Sandwich buckling formulas and applicability of standard computational algorithm for finite strain. *Composites Part B: Engineering, 35*(6–8), 573-581. doi: http://dx.doi.org/10.1016/j.compositesb.2003.11.009

Bažant, Z. P., & Beghini, A. (2006). Stability and finite strain of homogenized structures soft in shear: Sandwich or fiber composites, and layered bodies. *International Journal of Solids and Structures, 43*(6), 1571-1593. doi: http://dx.doi.org/10.1016/j.ijsolstr.2005.03.060

Benard, A., Boukhili, R., & Gauvin, R. (1991). Mechanical Behavior of Bidirectional Intraply Hybrid Lamina tes. *SAMPE Quarterly, 22*(no. 3), 8-15.

Blog, D. P. (2010). First Image: Disney Monorail Train Features Tron Art, from https://disneyparks.disney.go.com/blog/2010/03/first-image-disney-monorail-train-features-tron-art/

Bunsell, A. R., & Harris, B. (1974). Hybrid carbon and glass fibre composites. *Composites, 5*(4), 157-164. doi: http://dx.doi.org/10.1016/0010-4361(74)90107-4

Carlsson, L. A., & Kardomateas, G. A. (2011). *Structural and Failure Mechanics of Sandwich Composites* (Vol. 121): Springer Dordrecht Heidelberg London New York.

Chamis, C. C., & Lark, R. F. (1977). Hybrid composites, state-of-the-art review: Analysis, design, application and fabrication *NASA*.

Chau, F. W. (1987). Discussion of Paper by Minguez (1986). *Exper. Mech., 27*, pp. 388–389.

Chretien, N. (2002). *NUMERICAL CONSTITUTIVE MODELS OF WOVEN AND BRAIDED TEXTILE STRUCTURAL COMPOSITES.* Master of Science, Virginia Polytechnic Institute and State University, Blacksburg,Virginia.

Composite, C. (2016). Custom Made AFO's Mean Better Fit and Function, from http://www.cc-mfg.com/afo.html

COMPOSITE MATERIALS HANDBOOK, V. C. M. C. (2002).

Construction, R. B. (2016), from http://www.rapidwallksa.com/

Daniel, I. M., Gdoutos, E. E., Wang, K. A., & Abot, J. L. (2002). Failure Modes of Composite Sandwich Beams. *International Journal of Damage Mechanics, 11*(4), 309-334. doi: 10.1106/105678902027247

Das, M., Barut, A., Madenci, E., & Ambur, D. R. (2005). Complete stress field in sandwich panels with a new triangular finite element of single-layer theory. *Computer Methods in Applied Mechanics and Engineering, 194*(27–29), 2969-3005. doi: http://dx.doi.org/10.1016/j.cma.2004.07.033

Davies, I. J., & Hamada, H. (2001). Flexural properties of a hybrid polymer matrix composite containing carbon and silicon carbide fibres. *Advanced Composite Materials, 10*(1), 77-96. doi: 10.1163/15685510152546376

Dong, C., & Davies, I. J. (2012). Optimal design for the flexural behaviour of glass and carbon fibre reinforced polymer hybrid composites. *Materials & Design, 37*, 450-457. doi: http://dx.doi.org/10.1016/j.matdes.2012.01.021

Dong, C., Duong, J., & Davies, I. J. (2012). Flexural properties of S-2 glass and TR30S carbon fiber-reinforced epoxy hybrid composites. *Polymer Composites, 33*(5), 773-781. doi: 10.1002/pc.22206

Engesser, F. (1891). Die Knickfestigheit gerader Stabe. *Zentralblatt der Bauverwaltung, 11*, pp. 483-486.

Fleck, N. A., & Sridhar, I. (2002). End compression of sandwich columns. *Composites Part A: Applied Science and Manufacturing, 33*(3), 353-359. doi: http://dx.doi.org/10.1016/S1359-835X(01)00118-X

Gaiotti, M., & Rizzo, C. M. (2012). *Buckling behavior of FRP sandwich panels made by hand layup and vacuum bag infusion procedure*. Paper presented at the Sustainable Maritime Transportation and Exploitation of Sea Resources, Genoa, Italy.

Gay, D., Hoa, V. S., & Tsai, S. W. (2003). *Composite Materials Design and Applications*: CRC Press L.L.C.

Greene, E. (1999a). *Marine Composite*. Annapolis, MD: Eric Greene Associates.

Greene, E. (1999b). *Marine Composites* (1st ed.). Annapolis, MD: Eric Greene Associate.

Griffin, D. A. (2004). SAND 2001-0073 (Vol. Vol II): Sandia National Laboratories.

Grünewald, J., Parlevliet, P., & Altstädt, V. (2015). Manufacturing of thermoplastic composite sandwich structures: A review of literature. *Journal of Thermoplastic Composite Materials*. doi: 10.1177/0892705715604681

Gunyaev, G. M. (1977). Polycomponent high modulus composites. *Polymer Mechanics, 8*(1), pp 57-62.

. Gurit, GUIDE TO COMPOSITES. GURIT, www.gurit.com.

Hadcock, R. (1974). *The application of mixed fiber composites to military aircraft.* Paper presented at the Fiber Frontiers, 10th National State of the Art Symposium (American Chemical Society Division of Industrial and Engineering Chemistry, Washignton DC.

Hai, N. D., Mutsuyoshi, H., Asamoto, S., & Matsui, T. (2010). Structural behavior of hybrid FRP composite I-beam. *Construction and Building Materials, 24*(6), 956-969. doi: http://dx.doi.org/10.1016/j.conbuildmat.2009.11.022

Halimi, F., Golzar, M., Asadi, P., & Beheshty, M. (2013). Core modifications of sandwich panels fabricated by vacuum-assisted resin transfer molding. *Journal of Composite Materials, 47*(15), 1853-1863. doi: 10.1177/0021998312451763

Haringx, J. A. (1948). On Highly Compressible Helical Springs and Rubber Rods, and Their Application for Vibration-Free Mountings, I. *Phillips Research Reports* (Vol. 3, pp. pp. 401–449). Eindhoven, the Netherlands.

Hayashi, T. (1972). *On the improvement of mechanical properties of composites by hybrid composition*. Paper presented at the 8th Reinforced Plastics Congress, Brighton, UK.

Hedgepeth, J. N. (1998). Stress Concentrations in Filamentary Structures. NASA Langley Research Center; Hampton, VA United States: National Aeronautics and Space Administration.

Hess, T. E., Huang, S. L., & Rubin, H. (1977). Fracture Control in Composite Materials using integral crack arresters. *Journal of Aircraft, 14*(No 10), pp 994-999.

Hoa, V. S. (2009). *Principles of the Manufacturing of Composite Materials*. 439 North Duke Street. Lancaster, Pennsylvania 17602 U.S.A.: DEStech Publications, Inc.

Hsiao, H. M., & Daniel, I. M. (1996). Effect of fiber waviness on stiffness and strength reduction of unidirectional composites under compressive loading. *Composites Science and Technology, 56*(5), 581-593. doi: http://dx.doi.org/10.1016/0266-3538(96)00045-0

Hu, H.-T. (1995). Buckling analyses of fiber-composite laminate plates with material nonlinearity. *Finite Elements in Analysis and Design, 19*(3), 169-179. doi: http://dx.doi.org/10.1016/0168-874X(95)00009-I

Hyer, M. W. (1998). *Stress Analysis of Fiber-Reinforced Composite Materials*: McGraw-Hill.

Inovatec Systems, C. C. T. (2016), 2015, from http://www.innovida.com/default.asp

Irina, M. M. W., Azmi, A. I., Tan, C. L., Lee, C. C., & Khalil, A. N. M. (2015). Evaluation of Mechanical Properties of Hybrid Fiber Reinforced Polymer Composites and their Architecture. *Procedia Manufacturing, 2*, 236-240. doi: http://dx.doi.org/10.1016/j.promfg.2015.07.041

Johnson, G. R. (1978). *An investigation of methods of attaching steel components to carbon/glass hybrid laminates in the construction of body support systems.* Paper presented at the Proc Imperial College Aerodynamics Department Symposium, London.

Jones, R. M. (1999). *Mechanics of Composite Materials* (second edition ed.): Taylor & Francis.

Karlsson, K. F., & TomasÅström, B. (1997). Manufacturing and applications of structural sandwich components. *Composites Part A: Applied Science and Manufacturing, 28*(2), 97-111. doi: http://dx.doi.org/10.1016/S1359-835X(96)00098-X

Keller, T., Rothe, J., Castro, J. d., & Osei-Antwi, M. (2014). GFRP-Balsa Sandwich Bridge Deck: Concept, Design, and Experimental Validation. *Journal of Composites for Construction, 18*(2), 04013043. doi: doi:10.1061/(ASCE)CC.1943-5614.0000423

Khurmi, R. S., & Gupta, J. K. (2005). *A Textbook of Machine Design*: S Chand & Co Ltd.

Kliger, H. S. (1978a). *Designing cost-effective hybrid composites for automotive structures*. Paper presented at the Proc Annual Technical Conference Reinforced Plastics/Composites Institue Washington DC.

Kliger, H. S. (1978b). Simplified design with graphite reinforced plastics. *Mechanical Engineering 100*(No 6), pp 38-43.

Knops, M. (2008). *Analysis of Failure in Fiber Polymer Laminates, The Theory of Alfred Puck* (Corrected Second Printing ed.). New York: Springer-Verlag Berlin Heidelberg.

Kreja, I. (2011). A literature review on computational models for laminated composite and sandwich panels. [journal article]. *Central European Journal of Engineering, 1*(1), 59-80. doi: 10.2478/s13531-011-0005-x

Kretsis, G. (1987). A review of the tensile, compressive, flexural and shear properties of hybrid fibre-reinforced plastics. *Composites, 18*(1), 13-23. doi: 10.1016/0010-4361(87)90003-6

Krzyzak, A., Mazur, M., Gajewski, M., Drozd, K., Komorek, A., & przybylek, P. (2016). Sandwich Structured Composites for Aeronautics: Methods of Manufacturing Affecting Some Mechanical Properties. *International Journal of Aerospace Engineering, 2016*, 10. doi: 10.1155/2016/7816912

Lee, C. S., Lee, D. G., & Oh, J. H. (2004). Co-cure bonding method for foam core composite sandwich manufacturing. *Composite Structures, 66*(1–4), 231-238. doi: http://dx.doi.org/10.1016/j.compstruct.2004.04.042

Lightfoot, J. S., Wisnom, M. R., & Potter, K. (2013). Defects in woven preforms: Formation mechanisms and the effects of laminate design and layup protocol. *Composites Part A: Applied Science and Manufacturing, 51*, 99-107. doi: http://dx.doi.org/10.1016/j.compositesa.2013.04.004

Mallick, P. K. (2007). *Fiber-Reinforced Composites Materials, Manufacturing, and Design* (3rd ed.): CRC Press.

Manalo, A., Aravinthan, T., Fam, A., & Benmokrane, B. (2016). State-of-the-Art Review on FRP Sandwich Systems for Lightweight Civil Infrastructure. *Journal of Composites for Construction, 0*(0), 04016068. doi: doi:10.1061/(ASCE)CC.1943-5614.0000729

Manalo, A. C., Aravinthan, T., Karunasena, W., & Islam, M. M. (2010). Flexural behaviour of structural fibre composite sandwich beams in flatwise and edgewise positions. *Composite Structures, 92*(4), 984-995. doi: http://dx.doi.org/10.1016/j.compstruct.2009.09.046

Manders, P. W., & Bader, M. G. (1981). The strength of hybrid glass/carbon fibre composites. *Journal of Materials Science, 16*(8), 2233-2245. doi: 10.1007/bf00542386

Manual, A. V. U. In A. Inc. (Ed.). Southpointe, Canonsburge PA2016.

Marcinowski, J. (2003). *Geometrically nonlinear static analysis of sandwich plates and shells* (Vol. 41).

Margolis, J. M. (1986). Advanced Tberrnoset Composites Industrial and Commercial Applications. N. Y: Van Nostrand Reinhold Company,.

Marouene, A., Boukhili, R., Chen, J., & Yousefpour, A. (2016). Buckling behavior of variable-stiffness composite laminates manufactured by the tow-drop method. *Composite Structures, 139*, 243-253. doi: http://dx.doi.org/10.1016/j.compstruct.2015.12.025

Mastali, M., Valente, I. B., Barros, J. A. O., & Gonçalves, D. M. F. (2015). Development of innovative hybrid sandwich panel slabs: Experimental results. *Composite Structures, 133*, 476-498. doi: http://dx.doi.org/10.1016/j.compstruct.2015.07.114

Materials, M. A. (2016). LASA Helmets

May, G. L., & Tanner, C. (1979). Composite Truck Frame Rails. *Automotive Engineering*, pp 77-79.

Minguez, J. M. (1986). An Experimental Investigation of How Accurate, Simply Supported Boundary Conditions Can Be Achieved in Compression Testing of Panels. *Exper. Mech.*,(26), pp. 238–244.

Mohamed, M., Anandan, S., Huo, Z., Birman, V., Volz, J., & Chandrashekhara, K. (2015). Manufacturing and characterization of polyurethane based sandwich composite structures. *Composite Structures, 123*, 169-179. doi: http://dx.doi.org/10.1016/j.compstruct.2014.12.042

Naik, R. A. (1994). Analysis of Woven and Braided Fabric Reinforced Composites. Langley Research Center Hampton, Virginia: National Aeronautics and Space Administration.

NewRail, T. C. f. R. R. a. N. U. Retrieved 01/20/2013, from http://www.ncl.ac.uk/newrail/research/hycoprod.htm

Nunna, S., Chandra, P. R., Shrivastava, S., & Jalan, A. (2012). A review on mechanical behavior of natural fiber based hybrid composites. *Journal of Reinforced Plastics and Composites, 31*(11), 759-769.

Pandya, K. S., Veerraju, C., & Naik, N. K. (2011). Hybrid composites made of carbon and glass woven fabrics under quasi-static loading. *Materials & Design, 32*(7), 4094-4099. doi: http://dx.doi.org/10.1016/j.matdes.2011.03.003

Phillips, L. N. (1976). *On the usefulness of glass fiber carbon hybrids*. Paper presented at the 10th Congress, Innovation - the basis of reinforced plastics, Brighton, UK.

Plates, B. S. o. S. (1971). Washington, DC, United States: NASA SPACE VEHICLE DESIGN CRITERIA (Structures).

Rohwer K., F. S., Wehmeyer C. (2005). *Analyzing laminated structures from fibre-reinforced composite material - an assessment*. Paper presented at the Technische Mechanik 25.

Rolfes, R., & Rohwer, K. (1997). IMPROVED TRANSVERSE SHEAR STRESSES IN COMPOSITE FINITE ELEMENTS BASED ON FIRST ORDER SHEAR DEFORMATION THEORY. *International Journal for Numerical Methods in Engineering, 41*(1).

Sevkat, E. (2009). *HYBRID CARBON-GLASS FIBER/TOUGHENED EPOXY THICK COMPOSITES SUBJECT TO DROP-WEIGHT AND BALLISTIC IMPACTS.* Doctor of Philosophy, The City University of New York, Newyork, NY.

Sharaf, T., & Fam, A. (2012). Numerical modelling of sandwich panels with soft core and different rib configurations. *Journal of Reinforced Plastics and Composites, 31*(11), 771-784. doi: 10.1177/0731684412445494

Shimamura, S., & Ishine, K. (1976). *A contribution to the safety design of FRP cars* Paper presented at the 10th Congress Innovation - the basis of reinforced plastics, Brighton UK.

Short, D., & Summerscales, J. (1979). Hybrids-a review: Part 1. Techniques, design and construction. *Composites, 10*(4), 215-222. doi: http://dx.doi.org/10.1016/0010-4361(79)90022-3

Summerscales, J. (1983). *The Mechanical Properties of Carbon Fibre with Glass Fibre Hybrid Reinforced Plastics.* PhD, Plymouth Polytechnic, Plymouth, UK.

Summerscales, J. (1987). Marine Applications *Engineering Materials Handbook* (Vol. Vol. 1): ASM International.

Swolfs, Y., Gorbatikh, L., & Verpoest, I. (2014). Fibre hybridisation in polymer composites: A review. *Composites Part A: Applied Science and Manufacturing, 67*(0), 181-200. doi: http://dx.doi.org/10.1016/j.compositesa.2014.08.027

Sze, K., Chan, W. K., & Pian, T. H. H. (2002). An eight-node hybrid-stress solid-shell element for geometric non-linear analysis of elastic shells. *International Journal for Numerical Methods in Engineering, 55*(1).

Tanov, R., & Tabiei, A. (2000). A note on finite element implementation of sandwich shell homogenization. *International Journal for Numerical Methods in Engineering, 48*(3).

Thomas, D., & Cramer, D. (2008). Hybrid Thermoplastic Composite Ballistic Helmet Fabrication Study *Advancement of Materials & Process Engineering*.

Thompson, A. W. (1978). *Automotive Drive Shafts.* Paper presented at the Discission Meeting, New Fibers and thier composites, London.

Vinson, J. R. a. C., T-W. (1975). *Composite Materials and Their Use in Structures*. London: Applied Science Publishers, Ltd.

Walsh, S. M., Scott, D. M., & Spagnuolo, D. M. (2005). The Development of Hybrid Thermoplastic Ballistic Material with Application to Helmets: Army Research Labs, Aberdeen, MD.

Wang, L., Liu, W., & Hui, D. (2014). Compression strength of hollow sandwich columns with GFRP skins and a paulownia wood core. *Composites Part B: Engineering, 60*, 495-506. doi: http://dx.doi.org/10.1016/j.compositesb.2014.01.013

Whitney, J. M. (1987). *Structural Analysis of Laminated Anisotropic Plates*. Paper presented at the Technomic, Lancaster.

Xia, Y., & Ruiz, C. (1991). Analysis of damage in stress wave loaded unidirectional composites. *Computers & Structures, 38*(3), 251-258. doi: http://dx.doi.org/10.1016/0045-7949(91)90103-S

Xing, J., Hsiao, G. C., & Chou, T.-W. (1981). A Dynamic Explanation of The Hybrid Effect. *Journal of Composite Materials, 15*(5), 443-461. doi: 10.1177/002199838101500504

Yeter, E., Erkliğ, A., & Bulut, M. (2014). Hybridization effects on the buckling behavior of laminated composite plates. *Composite Structures, 118*, 19-27. doi: http://dx.doi.org/10.1016/j.compstruct.2014.07.020

You, Y.-J., Park, Y.-H., Kim, H.-Y., & Park, J.-S. (2007). Hybrid effect on tensile properties of FRP rods with various material compositions. *Composite Structures, 80*(1), 117-122. doi: http://dx.doi.org/10.1016/j.compstruct.2006.04.065

Young, J. (2016). The Weaves of Composite Fabrics Retrieved 10/03/2016, from http://blog.fibreglast.com/fiberglass/the-ins-and-outs-choosing-composite-fabric-by-weave/

Zhang, J., Chaisombat, K., He, S., & Wang, C. H. (2011). Hybrid composite laminates reinforced with glass/carbon woven fabrics for lightweight load bearing structures. *Materials & Design*.

Zhang, J., Supernak, P., Mueller-Alander, S., & Wang, C. H. (2013). Improving the bending strength and energy absorption of corrugated sandwich composite structure. *Materials & Design, 52*, 767-773. doi: http://dx.doi.org/10.1016/j.matdes.2013.05.018

Zhao, C., Zhang, G., & Wu, Y. (2012). Resin Flow Behavior Simulation of Grooved Foam Sandwich Composites with the Vacuum Assisted Resin Infusion (VARI) Molding Process. *Materials, 5*(7), 1285.

APPENDIX A – ANSYS ITERATIVE NEWTON-RAPHSON METHOD

The built-in set of non-linear equation in the ANSYS solver is defined as follows:

$$[K]\,\{u\}vv = \{Fa\} \qquad \text{(Manual)}$$

where:

[K] = coefficient matrix (stiffness matrix).

{u} = degree of freedom vector values.

$\{Fa\}$ = applied loads vector.

Equation (2-9) becomes non-linear when the matrix [K] is a function of the unknown values of its degree of freedom (DOF) vector values or their derivatives. The Newton-Raphson iterative non-linear equations are:

$$[\mathrm{KiT}]\{\Delta \mathrm{ui}\} = \{\mathrm{Finr}\} \qquad \text{(Manual)}$$

$$\{\mathrm{ui+1}\} = \{\mathrm{ui}\} + \{\Delta \mathrm{ui}\} \qquad \text{(Manual)}$$

where

[KiT] = Jacobian matrix.

{Finr} = vector of restoring loads equivalent to the element internal loads.

I = the current number of iteration.

The [KiT] matrix is the tangent stiffness matrix; {ui} is the displacement vector; and {Finr} is the restoring force vector calculated from the element stresses. The iteration cycle consists of five steps that can be written as follows:

1 – Start with {ui} = 0;

2 – Plug {ui} into equation (2-10) to calculate [KiT] and {Finr};

3- Calculate {Δui} from equation (2-11);

4- Add {Δui} to {ui} to calculate {ui+1}; and

5- Repeat steps 2 to 4 until reaching convergence.

An illustration of the iterative nonlinear solution following the above five steps is shown in Figure A1.

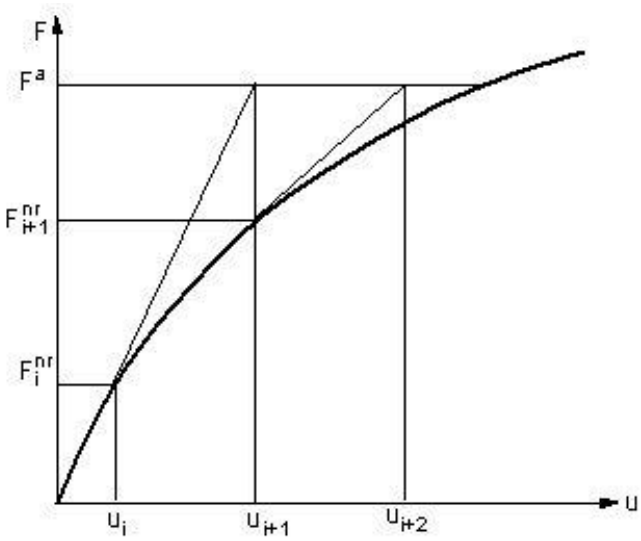

Figure A1: Newton-Raphson non-linear iterative method (Manual)

APPENDIX B – MATERIALS PROPERTIES USED IN NUMERICAL ANALYSIS

NOT MEASUREMENT SENSITIVE

MIL-HDBK-17-2F
Volume 2 of 5
17 JUNE 2002

SUPERSEDING
MIL-HDBK-17-2E
Volume 2 of 5
24 MAY 1999

DEPARTMENT OF DEFENSE HANDBOOK

COMPOSITE MATERIALS HANDBOOK

VOLUME 2. POLYMER MATRIX COMPOSITES MATERIALS PROPERTIES

This handbook is for guidance only. Do not cite this document as a requirement.

AMSC N/A AREA CMPS

DISTRIBUTION STATEMENT A. Approved for public release; distribution is unlimited.

4.2.6 T-300 3k/934 plain weave fabric

Material Description:

Material: T-300 3k/934

Form: Plain weave fabric, fiber areal weight of 196 g/m^2, typical cured resin content of 34%, typical cured ply thickness of 0.0078 inches.

Processing: Autoclave cure; 355°F, 85-100 psi for 2 hours.

General Supplier Information:

Fiber: T-300 fibers are continuous, no twist carbon filaments made from PAN precursor, surface treated to improve handling characteristics and structural properties. Filament count is 3,000 filaments/tow. Typical tensile modulus is 33 x 10^6. Typical tensile strength is 530,000 psi.

Matrix: 934 is a high flow, epoxy resin with good hot/wet properties and meets NASA outgassing requirements.

Maximum Short Term Service Temperature: 350°F (dry), 200°F (wet)

Typical applications: Aircraft primary and secondary structure, critical space structure.

* DATA WERE SUBMITTED BEFORE THE ESTABLISHMENT OF DATA DOCUMENTATION REQUIREMENTS (JUNE 1989). ALL DOCUMENTATION PRESENTLY REQUIRED WAS NOT SUPPLIED FOR THIS MATERIAL.

Table 4.2.6(e)
C/Ep 194-PW
T-300/934
Compression, 1-axis
$[0_f]_{12}$
75/A, -65/A, 250/A
Interim, Screening

MATERIAL: T-300 3k/934 plain weave fabric

RESIN CONTENT: 33-35 wt%
FIBER VOLUME: 58-60 %
PLY THICKNESS: 0.0074-0.0082 in.
COMP: DENSITY: 1.54-1.57 g/cm^3
VOID CONTENT: <0.5-1.2%

TEST METHOD: SACMA SRM 1-88

MODULUS CALCULATION: Chord between 20 and 40% of typical ultimate load

NORMALIZED BY: Specimen thickness and batch fiber volume to 57% (0.0077 in. CPT)

Temperature (°F)		75		-65		250	
Moisture Content (%)		ambient		ambient		ambient	
Equilibrium at T, RH							
Source Code		12		12		12	
		Normalized	Measured	Normalized	Measured	Normalized	Measured
F_1^{cu} (ksi)	Mean	95	98	104	108	100.	105
	Minimum	83	87	87	90.	94	98
	Maximum	120	125	133	139	107	111
	C.V.(%)	10.	10.	13	14	5.6	5.1
	B-value	(1)	(1)	(1)	(1)	(1)	(1)
	Distribution	ANOVA	ANOVA	ANOVA	ANOVA	Normal	Normal
	C_1	10.	11	15	16	100.	105
	C_2	3.9	3.9	3.7	3.8	5.64	5.4
	No. Specimens	20		20		5	
	No. Batches	4		4		1	
	Data Class	Interim		Interim		Screening	
E_1^c (Msi)	Mean	8.4	8.8	8.2	8.6	8.4	8.9
	Minimum	7.7	8.0	7.4	7.8	7.9	8.1
	Maximum	9.0	9.4	8.9	9.7	10.0	10.1
	C.V.(%)	5.1	5.3	5.1	5.7	6.3	6.4
	No. Specimens	20		20		19	
	No. Batches	4		4		4	
	Data Class	Interim		Interim		Interim	
ν_{12}^c	Mean						
	No. Specimens						
	No. Batches						
	Data Class						
ε_1^{cu} (με)	Mean						
	Minimum						
	Maximum						
	C.V.(%)						
	B-value						
	Distribution						
	C_1						
	C_2						
	No. Specimens						
	No. Batches						
	Data Class						

(1) Basis values are presented only for A and B data classes.
(2) Tab thickness of 0.112 - 0.120 inch is larger than 0.070 inch nominal thickness per method.
(3) Specimen thickness of 0.09 - 0.10 inch is less than nominal 0.12 inch thickness per method.

* DATA WERE SUBMITTED BEFORE THE ESTABLISHMENT OF DATA DOCUMENTATION REQUIREMENTS (JUNE 1989). ALL DOCUMENTATION PRESENTLY REQUIRED WAS NOT SUPPLIED FOR THIS MATERIAL.

Table 4.2.6(g)
C/Ep 194-PW
T-300/934
Compression, 2-axis
$[90_t]_{12}$
75/A, -65/A, 250/A
Interim, Screening

MATERIAL: T-300 3k/934 plain weave fabric

RESIN CONTENT: 33-35 wt% COMP: DENSITY: 1.54-1.57 g/cm^3
FIBER VOLUME: 58-60 % VOID CONTENT: <0.5-1.2%
PLY THICKNESS: 0.0074-0.0082 in.

TEST METHOD: SACMA SRM 1-88

MODULUS CALCULATION: Chord between 20 and 40% of typical ultimate load

NORMALIZED BY: Specimen thickness and batch fiber volume to 57% (0.0077 in. CPT)

Temperature (°F)		75		-65		250	
Moisture Content (%)		ambient		ambient		ambient	
Equilibrium at T, RH							
Source Code		12		12		12	
		Normalized	Measured	Normalized	Measured	Normalized	Measured
F_2^{cu} (2) (ksi)	Mean	90.	93	103	106	82	85
	Minimum	81	85	94	98	77	81
	Maximum	100.	104	116	121	84	88
	C.V.(%)	5.9	6.0	6.2	6.1	3.4	3.4
	B-value	(4)	(4)	(1)	(1)	(1)	(1)
	Distribution	ANOVA	ANOVA	Normal	Normal	Normal	Normal
	C_1	5.6	5.9	103	106	81.7	85.3
	C_2	3.2	3.2	6.18	6.4	2.74	2.86
	No. Specimens	20		20		5	
	No. Batches	4		4		1	
	Data Class	Interim		Interim		Screening	
E_2^c (3) (Msi)	Mean	8.3	8.6	8.4	8.8	8.8	9.0
	Minimum	7.4	7.7	7.5	7.7	7.9	8.1
	Maximum	9.3	9.5	9.0	9.4	10.2	10.6
	C.V.(%)	7.0	6.6	5.1	5.5	8.4	8.9
	No. Specimens	20		20		20	
	No. Batches	4		4		4	
	Data Class	Interim		Interim		Interim	
ν_{21}^c	Mean						
	No. Specimens						
	No. Batches						
	Data Class						
ε_2^{cu} (με)	Mean						
	Minimum						
	Maximum						
	C.V.(%)						
	B-value						
	Distribution						
	C_1						
	C_2						
	No. Specimens						
	No. Batches						
	Data Class						

(1) Basis values are presented only for A and B data classes.
(2) Tab thickness of 0.112-0.120 inch is larger than 0.070 inch nominal thickness per method.
(3) Specimen thickness of 0.09-0.10 inch is less than nominal 0.120 inch thickness per method.
(4) B-basis values calculated from less than five batches of data using the ANOVA method are not presented.

6.2.4 E-Glass 7781/EA9396 8-harness satin weave fabric

Material Description:

Material: E7781/EA9396

Form: Eight harness satin fabric of style 7781, fiber areal weight of 295 g/m^2, dry fabric impregnated in a wet lay-up process, typical cured resin content of 25.9 to 30.4%, typical cured ply thickness of 0.008 inches.

Processing: Vacuum Bag cure; 200°F, 25 inches Hg, 45 minutes

General Supplier Information:

Fiber: Continuous E-glass fiber woven by Hexcel using F-16 (Volan-A) sizing. Typical tensile modulus is 10 x 10^6 psi. Typical tensile strength is 500,000 psi.

Matrix: EA9396 is a 200°F curing toughened epoxy resin with improved hot/wet properties. 75 minute pot life for 1 lb batch. This resin is a two part, unfilled version of EA 9394.

Maximum Short Term Service Temperature: Not determined from available data, but at least 150°F.

Typical applications: Aircraft repair

Data Analysis Summary:

1. This material was tested at fiber volumes that may be higher than what are typically used for repair. Data should be substantiated if used at lower fiber volumes.
2. Glass transition temperature (Tg) values were not reported because they were determined on neat resin using a non-standard method.
3. Wet properties are very low because of the glass and sizing combination.
4. Contrary to expectations, the fill tensile strengths and stiffnesses were greater than the warp properties.
5. Most tension failures were under the tabs, but were included since the strengths were consistent with correct failure modes.
6. Variability between batches is high. Documentation does not reveal a reason.
7. High end outliers for the following properties were discarded:
   a. Transverse tension strain at 72°F ambient
   b. Transverse tension modulus at -65°F ambient and 72°F wet
   c. Transverse compression modulus at 72°F wet
8. Data are from publicly available report, Reference 4.2.27.
9. Test method dates were assumed from the testing dates rather than obtained from the data source.

* ALL DOCUMENTATION PRESENTLY REQUIRED WERE NOT SUPPLIED FOR THIS MATERIAL.

Table 6.2.4(d)
EGl/Ep 295-8HS
E-7781/EA 9396
Compression, 1-axis
$[0_f]_{18}$
72/A,72/W
Interim

MATERIAL: E-Glass 7781/EA 9396 8-harness satin weave fabric

RESIN CONTENT: 27.6-30.4 wt% COMP: DENSITY: 1.89-1.93 g/cm^3
FIBER VOLUME: 54.1-55.8% VOID CONTENT: 3.7-5.4%
PLY THICKNESS: 0.0085-0.0086 in.

TEST METHOD: ASTM D 3410B-87

MODULUS CALCULATION: Chord between 1000 and 3000με

NORMALIZED BY: Specimen thickness and batch fiber areal weight to 50% fiber volume (0.0085 in. CPT)

Temperature (°F)		72		72				
Moisture Content (%)		Ambient		1.68-2.33				
Equilibrium at T, RH				(1)				
Source Code		30		30				
		Normalized	Measured	Normalized	Measured	Normalized	Measured	
F_1^{cu} (ksi)	Mean	46.4	49.6	20.3	21.0			
	Minimum	41.1	43.9	11.2	11.0			
	Maximum	51.2	55.5	26.3	27.0			
	C.V.(%)	5.96	5.84	27.6	27.8			
	B-value	(2)	(2)	(2)	(2)			
	Distribution	Weibull	Weibull	ANOVA	ANOVA			
	C_1	47.6	51.0	6.40	6.71			
	C_2	17.5	18.5	4.91	5.67			
	No. Specimens	15		15				
	No. Batches	3		3				
	Data Class	Interim		Interim				
E_1^c (Msi)	Mean	3.45	3.68	3.06	3.18			
	Minimum	2.96	3.17	2.56	2.56			
	Maximum	3.86	4.11	3.77	3.85			
	C.V.(%)	6.24	5.98	10.1	10.1			
	No. Specimens	15		15				
	No. Batches	3		3				
	Data Class	Interim		Interim				
ν_{12}^c	Mean							
	No. Specimens							
	No. Batches							
	Data Class							
ε_1^{cu} (με)	Mean	14700		7160				
	Minimum	11700		4160				
	Maximum	19600		10600				
	C.V.(%)	12.8		27.3				
	B-value	(2)		(2)				
	Distribution	ANOVA		ANOVA				
	C_1	3.25		4.72				
	C_2	1940		2130				
	No. Specimens	15		15				
	No. Batches	3		3				
	Data Class	Interim		Interim				

(1) Specimens conditioned at 140°F, 95-100% R.H for 68-180 days.
(2) Basis values are presented only for A and B data classes.

* ALL DOCUMENTATION PRESENTLY REQUIRED WERE NOT SUPPLIED FOR THIS MATERIAL.

Table 6.2.4(e)
EGl/Ep 295-8HS
E-7781/EA 9396
Compression, 2-axis
$[0_7]_{18}$
-65/A, 72/A, 200/A
Interim, Screening

MATERIAL: E-Glass 7781/EA 9396 8-harness satin weave fabric

RESIN CONTENT: 27.6-30.4 wt%
FIBER VOLUME: 51.2-53.8 %
PLY THICKNESS: 0.0083-0.0085 in.

COMP: DENSITY: 1.89-1.93 g/cm^3
VOID CONTENT: 4.0-5.0 %

TEST METHOD:
ASTM D 3410B-87

MODULUS CALCULATION:
Chord between 1000 and 3000με

NORMALIZED BY: Specimen thickness and batch fiber areal weight to 50% fiber volume (0.0085 in. CPT)

Temperature (°F)		72		-65		200	
Moisture Content (%)		Ambient		Ambient		Ambient	
Equilibrium at T, RH							
Source Code		30		30		30	
		Normalized	Measured	Normalized	Measured	Normalized	Measured
F_2^{cu} (ksi)	Mean	37.7	40.8	59.2	63.8	26.9	29.0
	Minimum	32.4	35.3	50.8	55.8	20.4	23.4
	Maximum	42.9	46.0	68.9	73.5	34.4	37.2
	C.V.(%)	8.72	7.60	9.72	9.58	16.1	15.1
	B-value	(1)	(1)	(1)	(1)	(1)	(1)
	Distribution	Weibull	Weibull	ANOVA	ANOVA	ANOVA	ANOVA
	C_1	39.2	42.3	6.54	5.33	5.07	5.75
	C_2	11.6	15.1	4.81	6.87	5.00	5.16
	No. Specimens	15		15		12	
	No. Batches	3		3		3	
	Data Class	Interim		Interim		Screening	
E_2^c (Msi)	Mean	3.37	3.66	3.89	4.18	3.23	3.49
	Minimum	2.94	3.13	3.38	3.63	2.82	2.98
	Maximum	3.61	3.93	4.17	4.55	3.54	3.83
	C.V.(%)	6.04	6.70	5.79	5.84	7.64	7.23
	No. Specimens	15		15		12	
	No. Batches	3		3		3	
	Data Class	Interim		Interim		Screening	
ν_{21}^c	Mean						
	No. Specimens						
	No. Batches						
	Data Class						
ε_2^{cu} (με)	Mean		11900		16800		8650
	Minimum		9020		13400		6550
	Maximum		17800		20800		12400
	C.V.(%)		20.1		11.8		19.5
	B-value		(1)		(1)		(1)
	Distribution		Weibull		ANOVA		Weibull
	C_1		12900		5.06		9340
	C_2		5.04		2200		5.42
	No. Specimens	15		15		12	
	No. Batches	3		3		3	
	Data Class	Interim		Interim		Screening	

(1) Basis values are presented only for A and B data classes.
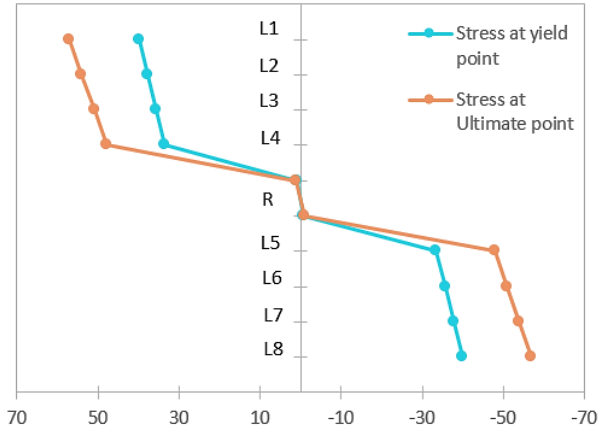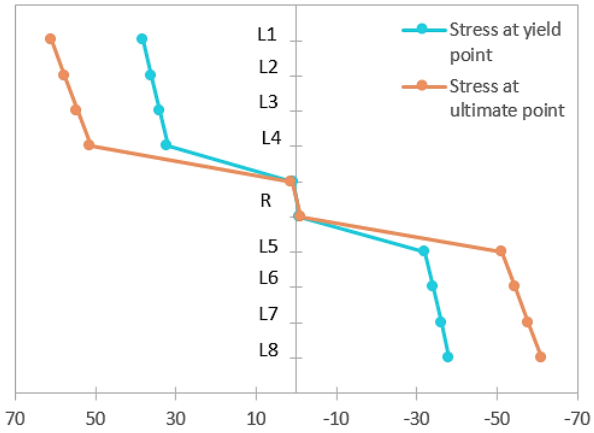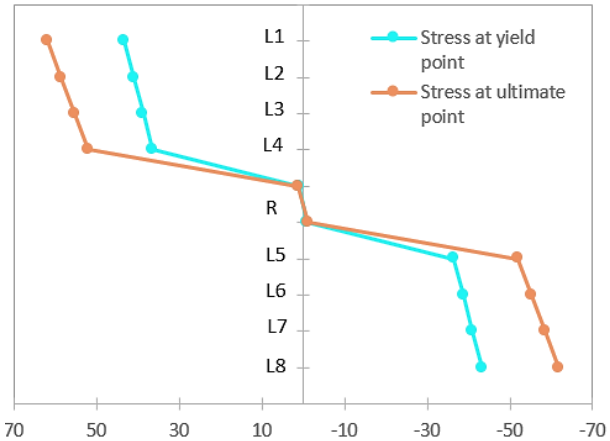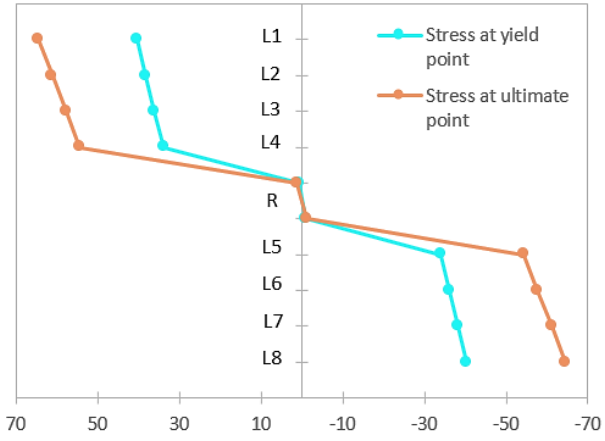
APPENDIX C – STRESS DISTRIBUTION ACROSS NUMERICAL MODEL'S THICKNESS